Dissertation zur Erlangung des Doktorgrades

der Fakultät für Chemie und Pharmazie

der Ludwig-Maximilians-Universität München

Single molecule diffusion studies in nanoporous systems: From fundamental concepts to material science and nano-medicine

Florian Feil

aus

München

2012

Erklärung

Diese Dissertation wurde im Sinne von § 7 der Promotionsordnung vom 28. November 2011 von Herrn Prof. Dr. Christoph Bräuchle betreut.

Eidesstattliche Versicherung

Diese Dissertation wurde eigenständig und ohne unerlaubte Hilfe erarbeitet.

München, den 24.04.2012

Florian Feil

Dissertation eingereicht am:	24.04.2012
1. Gutachter:	Prof. Dr. Christoph Bräuchle
2. Gutachter:	Prof. Dr. Jens Michaelis
Mündliche Prüfung am:	22.05.2012

Contents

Der Zweifel ist der Beginn der Wissenschaft. Wer nichts anzweifelt, prüft nichts. Wer nichts prüft, entdeckt nichts. Wer nichts entdeckt, ist blind und bleibt blind.

Marie-Joseph Pierre Teilhard de Chardin, 1881 - 1955

Phantasie ist wichtiger als Wissen, denn Wissen ist begrenzt.

Albert Einstein, 1879 - 1955

1 Introduction

Diffusion describes the propagation of particles, such as molecules, via random thermal motion driven by a concentration gradient. The diffusive transport mechanism is essential for countless processes in nature and technology.[1-4] In chemistry, diffusion is in most cases the major mechanism of bringing the reactants in close proximity to each other, which is an essential prerequisite before any chemical reaction can occur. Moreover, many reactions are diffusion controlled, i.e. the reaction kinetic is limited by the diffusion process. In particular, for the transport processes ongoing within nanoporous systems diffusion plays a crucial role. These nanoporous materials are of interest for numerous potential applications,[5] such as molecular separation,[6-8] sensor systems,[9, 10] catalysis,[11, 12] photovoltaic solar cells,[13, 14] and drug delivery devices for nano-medicine.[15-17] The ability to specifically design nanoporous materials and to improve their properties with respect to a particular functionality is therefore strongly desired. That is why nanotechnology, which usually implies the knowledge and understanding as well as the manipulation of matter at the nanometer (10^{-9} m) scale, has emerged as a promising approach towards novel high-tech materials in recent decades. However, in order to develop such customized host-guest systems for nanotechnology applications, a thorough knowledge of the interactions between the porous host and the guest molecules is required. Usually, the investigation of porous host systems and of the guest molecules diffusing inside the channel systems is accomplished by determining an average host structure and/or by averaging over a large number (ensemble) of guest molecules. Such methods include NMR,[18, 19] IR and UV-Vis spectroscopy[20] and X-ray diffraction.[21] However, the dynamical behavior of the guest molecules is typically spatially and temporally heterogeneous on the nanometer scale. Therefore, it might be impossible to conceive the true behavior of the single molecules within their respective environment and thus the real distribution of investigated variables due to the averaging process. Recently, single molecule experiments, in which the motion of a single particle is directly observed over time, provided a completely new view on diffusion. In this approach, the trajectory of a single, fluorescently labeled molecule is recorded during a sufficiently long interval of time. The thus obtained trajectory can thereafter be analyzed to reveal the presence of subpopulations, rare events and the influence of heterogeneities of the structural environment on the diffusing molecules in unprecedented detail.

This thesis is devoted to the investigation of diffusion of molecular guest molecules within nanoporous host structures using single molecule fluorescence microscopy and single particle tracking. In particular, this thesis is structured as described in the following. After the introduction, the basic theoretical background and methods related to the topics covered in this work will be explained in chapter 2. A brief overview of nanoporous materials is given first, followed by the derivation of the theoretical concepts of diffusion. Next, a detailed explanation of the phenomenon of fluorescence is provided. This process is prerequisite for the method of single molecule fluorescence microscopy, which will be introduced subsequently. In this regard also the technical details of the used microscope setup are enlisted. The procedure of the data analysis including single particle tracking will be presented at the end of the chapter.

In chapter 3 to 6 six different studies utilizing single molecule microscopy techniques are presented. In the first of these investigations in chapter 3, a fundamental concept central to the dynamics of diffusion, the ergodic theorem, is tested. Ergodicity means that for systems under equilibrium the time average taken over a single particle is the same as the ensemble average over many particles. While this principle is key to several fields of mathematics and physics, it has been lacking experimental proof so far.

Chapter 4 deals with the investigation and structuring of nanoporous matter with emphasis on potential applications in material science. Ordered mesoporous silica materials have recently advanced to an important class of self-assembled nano-structured materials on account of their variety of structures and pore geometries, controllable pore sizes and their widely tunable properties, for example by pore functionalization.[22-24] Chapter 4.1 is dedicated to the synthesis and patterning of highly structured, collinear silica mesopores functionalized to incorporate organic dye molecules or bio-molecules, such as DNA, as well as the direct visualization of these guest molecules in real space. Thereby, dynamical and structural information of this sophisticated host-guest system are acquired. The following investigation of mesoporous silica materials in chapter 4.2 is focused on the interactions between the porous host and the guest molecules, which play a crucial role for the overall properties of the material. Therefore, three structurally slightly different dyes were studied in hexagonal and lamellar silica structures with regard to their diffusional behavior.

In recent years there has been a growing interest in the unique optical properties of nano-structures of (noble) metal assemblies, which are caused by the collective oscillation of free electrons, known as plasmon resonances.[25-27] Consequently, a thorough understanding of these properties is essential for the development of customized plasmonic systems for nanotechnology applications. Such potential utilizations include surface-enhanced Raman scattering (SERS),[28-31] gas or bio-molecular sensors,[32, 33] full color holograms[34] and coupling to luminescent particles, such as dye molecules,[35-37] quantum dots[38, 39] or metal nano-particles.[40] In chapter 5.1 such plasmon coupling of silver-island films to organic dye molecules and quantum dots resulting in fluorescence enhancement and quenching of the fluorophore in relation to its relative position to the silver-island film is demonstrated. While the influence of metal nanoparticles on the absorption and emission of single fluorophores is an interesting field of research yet to be fully explored, also the luminescence after photo-activation of metal nanostructures itself is a worthwhile subject to investigate. Therefore, using wide-field fluorescence microscopy, the photophysical properties of silver nano-wires were investigated in a separate study presented in chapter 5.2.

Finally, the application of porous materials as nano-carriers for drug delivery purposes in nanomedicine will be discussed. Thereby, a specific dose of a therapeutic agent can be delivered in a controlled way over an extended amount of time. Various materials have been used for the preparation of sustained release devices for macromolecules. In particular, the sustained release of protein drugs from lipid drug reservoirs is a very promising approach for long term delivery due to the excellent stability, biocompatibility [41, 42] and biodegradability [41, 43] of the lipid devices. The general mechanisms of sustained protein release from inert matrices were already extensively reviewed.[44-46] Thereby, it was found that macromolecular drug release from such devices is much more sustained than mathematical models predicted.[44] However, due to the lack of methods to directly visualize the processes within such lipid matrices, this retention could not be fully explained so far. Using single molecule microscopy and tracking of individual fluorescently labeled recombinant human IFNα protein molecules within lipid tsc-extrudates the diffusion processes within those drug delivery devices could be observed directly for the first time. This allows for the elucidation of the major mechanisms which contribute to the sustained release from such tsc-extrudates.

Most of the results in this thesis have been published previously in peer-reviewed journals and are thus presented in a cumulative manner in the individual sections of the thesis. Therefore, each section is self-contained including a separate numeration of figures, tables, etc. and its own bibliography. The respective published references are given at the beginning of each section. The thesis concludes with a summary, followed by several appendices, such as a list of abbreviations, a list of publication and the acknowledgements.

References

1. F. Crick, DIFFUSION IN EMBRYOGENESIS. *Nature* **225**, 420 (1970).
2. E. R. Weeks, J. C. Crocker, A. C. Levitt, A. Schofield, D. A. Weitz, Three-dimensional direct imaging of structural relaxation near the colloidal glass transition. *Science* **287**, 627 (2000).
3. L. A. Hayden, E. B. Watson, A diffusion mechanism for core-mantle interaction. *Nature* **450**, 709 (2007).
4. S. Kondo, T. Miura, Reaction-Diffusion Model as a Framework for Understanding Biological Pattern Formation. *Science* **329**, 1616 (2010).
5. M. E. Davis, Ordered porous materials for emerging applications. *Nature* **417**, 813 (2002).
6. M. J. Wirth, R. W. P. Fairbank, H. O. Fatunmbi, Mixed Self-Assembled Monolayers in Chemical Separations. *Science* **275**, 44 (1997).
7. S. J. L. Billinge *et al.*, Mercury binding sites in thiol-functionalized mesostructured silica. *Journal of the American Chemical Society* **127**, 8492 (2005).
8. R. Brady, B. Woonton, M. L. Gee, A. J. O'Connor, Hierarchical mesoporous silica materials for separation of functional food ingredients -- A review. *Innovative Food Science & Emerging Technologies* **9**, 243 (2008).
9. H. S. Peng *et al.*, Responsive periodic mesoporous polydiacetylene/silica nanocomposites. *Journal of the American Chemical Society* **128**, 5304 (2006).
10. J. Lei, L. Wang, J. Zhang, Ratiometric pH sensor based on mesoporous silica nanoparticles and Forster resonance energy transfer. *Chemical Communications* **46**, 8445 (2010).
11. W. M. Van Rhijn, D. E. De Vos, B. F. Sels, W. D. Bossaert, P. A. Jacobs, Sulfonic acid functionalised ordered mesoporous materials as catalysts for condensation and esterification reactions. *Chemical Communications*, 317 (1998).
12. D. E. De Vos, M. Dams, B. F. Sels, P. A. Jacobs, Ordered mesoporous and microporous molecular sieves functionalized with transition metal complexes as catalysts for selective organic transformations. *Chemical Reviews* **102**, 3615 (2002).
13. M. Gratzel, Photoelectrochemical cells. *Nature* **414**, 338 (2001).
14. J. Font *et al.*, Periodic mesoporous silica having covalently attached tris(bipyridine)ruthenium complex: synthesis, photovoltaic and electrochemiluminescent properties. *Journal of Materials Chemistry* **17**, 2336 (2007).
15. C.-Y. Lai *et al.*, A Mesoporous Silica Nanosphere-Based Carrier System with Chemically Removable CdS Nanoparticle Caps for Stimuli-Responsive Controlled

Release of Neurotransmitters and Drug Molecules. *Journal of the American Chemical Society* **125**, 4451 (2003).

16. V. Cauda *et al.*, Colchicine-Loaded Lipid Bilayer-Coated 50 nm Mesoporous Nanoparticles Efficiently Induce Microtubule Depolymerization upon Cell Uptake. *Nano Letters* **10**, 2484 (2010).
17. A. Schlossbauer *et al.*, A Programmable DNA-Based Molecular Valve for Colloidal Mesoporous Silica. *Angewandte Chemie International Edition* **49**, 4734 (2010).
18. V. Kukla *et al.*, NMR Studies of Single-File Diffusion in Unidimensional Channel Zeolites. *Science* **272**, 702 (1996).
19. F. Stallmach, J. Kärger, C. Krause, M. Jeschke, U. Oberhagemann, Evidence of anisotropic self-diffusion of guest molecules in nanoporous materials of MCM-41 type. *Journal of the American Chemical Society* **122**, 9237 (2000).
20. S. G. Choi *et al.*, Application of mesoporous TiO_2 as a thermal isolation layer for infrared sensors. *Thin Solid Films* **516**, 212 (2007).
21. M. Klotz *et al.*, The true structure of hexagonal mesophase-templated silica films as revealed by X-ray scattering: Effects of thermal treatments and of nanoparticle seeding. *Chemistry of Materials* **12**, 1721 (2000).
22. G. Wirnsberger, G. D. Stucky, Ordered mesostructured materials with optical functionality. *A European Journal of Chemical Physics and Physical Chemistry* **1**, 90 (2000).
23. M. Manzano *et al.*, Studies on MCM-41 mesoporous silica for drug delivery: Effect of particle morphology and amine functionalization. *Chemical Engineering Journal* **137**, 30 (2008).
24. V. Cauda, A. Schlossbauer, J. Kecht, A. Zürner, T. Bein, Multiple core-shell functionalized mesoporous silica nanoparticles. *Journal of the American Chemical Society* **131**, 11361 (2009).
25. W. L. Barnes, A. Dereux, T. W. Ebbesen, Surface plasmon subwavelength optics. *Nature* **424**, 824 (2003).
26. E. Ozbay, Plasmonics: Merging photonics and electronics at nanoscale dimensions. *Science* **311**, 189 (2006).
27. R. Kolesov *et al.*, Wave-particle duality of single surface plasmon polaritons. *Nature Physics* **5**, 470 (2009).
28. P. Mohanty *et al.*, Simple vapor-phase synthesis of single-crystalline Ag nanowires and single-nanowire surface-enhanced raman scattering. *Journal of the American Chemical Society* **129**, 9576 (2007).
29. J. M. Baik, S. J. Lee, M. Moskovits, Polarized Surface-Enhanced Raman Spectroscopy from Molecules Adsorbed in Nano-Gaps Produced by Electromigration in Silver Nanowires. *Nano Letters* **9**, 672 (2009).
30. Y. R. Fang, H. Wei, F. Hao, P. Nordlander, H. X. Xu, Remote-Excitation Surface-Enhanced Raman Scattering Using Propagating Ag Nanowire Plasmons. *Nano Letters* **9**, 2049 (2009).
31. I. Yoon *et al.*, Single Nanowire on a Film as an Efficient SERS-Active Platform. *Journal of the American Chemical Society* **131**, 758 (2009).
32. B. J. Murray, Q. Li, J. T. Newberg, J. C. Hemminger, R. M. Penner, Silver oxide microwires: Electrodeposition and observation of reversible resistance modulation upon exposure to ammonia vapor. *Chemistry of Materials* **17**, 6611 (2005).
33. S. E. Brunker, K. B. Cederquist, C. D. Keating, Metallic barcodes for multiplexed bioassays. *Nanomedicine* **2**, 695 (2007).

34. M. Ozaki, J. Kato, S. Kawata, Surface-Plasmon Holography with White-Light Illumination. *Science* **332**, 218 (2011).
35. S. L. Pan, L. J. Rothberg, Enhancement of platinum octaethyl porphyrin phosphorescence near nanotextured silver surfaces. *Journal of the American Chemical Society* **127**, 6087 (2005).
36. S. L. Pan, Z. J. Wang, L. J. Rothberg, Enhancement of adsorbed dye monolayer fluorescence by a silver nanoparticle overlayer. *Journal of Physical Chemistry B* **110**, 17383 (2006).
37. S. H. Guo, D. G. Britti, J. J. Heetderks, H. C. Kan, R. J. Phaneuf, Spacer Layer Effect in Fluorescence Enhancement from Silver Nanowires over a Silver Film; Switching of Optimum Polarization. *Nano Letters* **9**, 2666 (2009).
38. A. V. Akimov *et al.*, Generation of single optical plasmons in metallic nanowires coupled to quantum dots. *Nature* **450**, 402 (2007).
39. C. Grillet *et al.*, Nanowire coupling to photonic crystal nanocavities for single photon sources. *Optics Express* **15**, 1267 (2007).
40. Z. Y. Fang *et al.*, Plasmonic Coupling of Bow Tie Antennas with Ag Nanowire. *Nano Letters* **11**, 1676 (2011).
41. C. Guse *et al.*, Biocompatibility and erosion behavior of implants made of triglycerides and blends with cholesterol and phospholipids. *International Journal of Pharmaceutics* **314**, 153 (2006).
42. M. Schwab *et al.*, Correlation of in vivo and in vitro release data for rh-INF[alpha] lipid implants. *European Journal of Pharmaceutics and Biopharmaceutics* **70**, 690 (2008).
43. M. Schwab, G. Sax, S. Schulze, G. Winter, Studies on the lipase induced degradation of lipid based drug delivery systems. *Journal of Controlled Release* **140**, 27 (2009).
44. R. A. Siegel, R. Langer, Controlled Release of Polypeptides and Other Macromolecules. *Pharmaceutical Research* **1**, 2 (1984).
45. R. A. Siegel, R. Langer, Mechanistic studies of macromolecular drug release from macroporous polymers. II. Models for the slow kinetics of drug release. *Journal of Controlled Release* **14**, 153 (1990).
46. R. A. Siegel, J. Kost, R. Langer, Mechanistic studies of macromolecular drug release from macroporous polymers. I. Experiments and preliminary theory concerning completeness of drug release. *Journal of Controlled Release* **8**, 223 (1989).

2 Theoretical background and methods

2.1 Nanoporous materials

Porous materials are classified into three categories according to the International Union of Pure and Applied Chemistry (IUPAC) based on their pore sizes.[1] Hereby, materials with pore sizes below 2 nm are called microporous, between 2 nm and 50 nm mesoporous and above 50 nm macroporous. Furthermore, porous matter can be found in crystalline or amorphous structures. For example microporous zeolites posses a highly ordered crystalline structure. Moreover, there are materials, such as mesoporous silica, which are composed of amorphous silica, i.e. glass, however, their pore arrangement might still exhibit various topologies. These include for example hexagonal, cubic or lamellar structures. In many cases porous systems exhibits no order at all resulting in random networks.

There are two general strategies for the synthesis of nano-structured porous matter, which are characterized by a top-down and a bottom-up approach, respectively (Figure 1). Top-down approaches employ macro-sized, externally-controlled devices in order to downsize bulk material into nano-scaled patterns. Thereby, often common micro-fabrication methods and tools are used to cut, mill, etch and shape the bulk material into the desired form and structure. Photolithography and inkjet printing are famous examples of such micropatterning techniques. A top-down approach was utilized for example in the work described in chapter 3 to fabricate the nanoporous glass applied in the study. Briefly, sodium borosilicate glass containing two separated glass phases was treated with hydrochloric acid at elevated temperatures in order to remove only one of these phases by etching. Details of the entire manufacturing procedure are given in chapter 3.

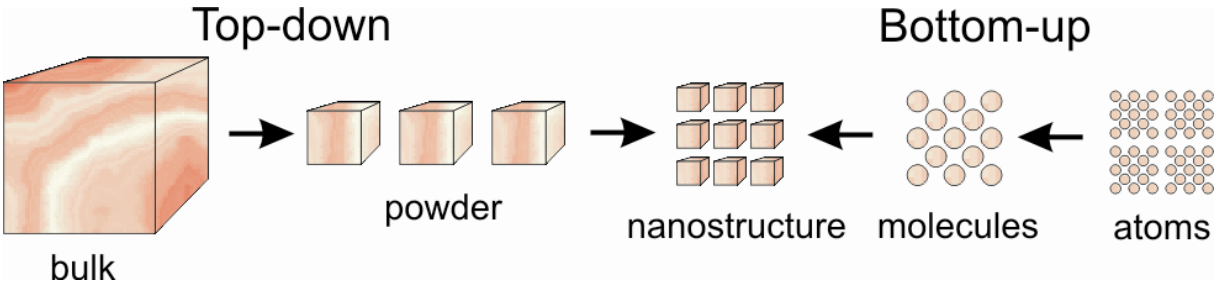

Figure 1: Top-down and bottom-up approach.

In the bottom-up approach, complex structures are built up starting from small, typically molecular components. Here, the physical and chemical properties of the individual molecules are exploited to self-assembly into the desired structure by molecular recognition. In general, the bottom-up approach is advantageous over top-down techniques, because of the faster and cheaper production of nano-scaled materials. However, with increasing size and complexity of the fabricated device the use of bottom-up strategies becomes dramatically more challenging. An example of such a bottom-up self assembly process is the synthesis of the mesoporous silica materials described in chapter 4. In this approach silica polycondensation around a templating agent is utilized to form nano-scaled structures. In particular, silica monomers, such as tetraehtyl orthosilicate (TEOS), are first hydrolyzed under acid- or base-catalyzed conditions at elevated temperatures. Upon cooling silica precursor molecules undergo condensation and thus form a three-dimensional interconnected, solid silica structure. The acid-catalyzed hydrolysis and condensation reaction is illustrated in Figure 2.

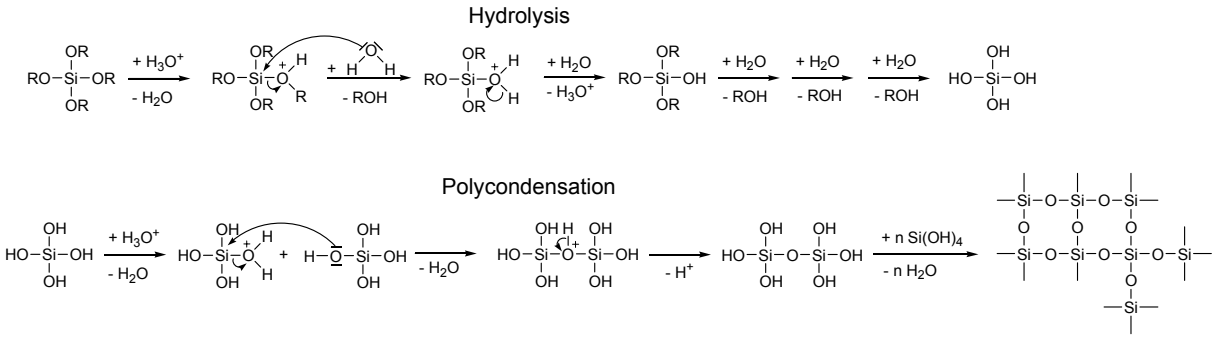

Figure 2: Acid-catalyzed hydrolysis and condensation of silica monomers.

During this process the precursor solution containing TEOS as silica source, a surfactant, ethanol, water and acid or base is evaporated. Thereby, the surfactant concentration rises above the so-called critical micelle concentration resulting in the spontaneous formation of surfactant micelles, while the silica condensation reaction occurs. This leads to the formation of a porous silica structure. The driving force behind this self-assembly is the minimization of the repulsive interactions between the hydrophilic head and the hydrophobic tail of the surfactant with the solvent. The entire process is called evaporation-induced self-assembly (EISA).[2]

However, the ordering of the mesoporous channel alignment over long distances via bottom-up strategies, such as the EISA process, is very challenging as it was stated before and has thus been mostly unavailable so far. Sophisticated patterning techniques have to be developed to circumvent this restriction. Such an approach towards the production of highly ordered, collinear mesopores over extended distances is provided in chapter 4.1.

Nanoporous materials are almost exclusively designed and applied as host systems for the incorporation of guest molecules. Therefore, the diffusional behavior of these guest molecules within the porous host is essential for the properties of the resulting nano-material. In order to design novel, customized nano-structured devices, it is thus vital to investigate and understand diffusion processes in such systems. The theoretical basis to understand the diffusion processes studied in this thesis is derived in the following chapter.

2.2 Diffusion

Diffusion is defined as the random motion of particles within a medium caused by thermal energy. This motion can be described by the diffusion laws. Central values to this are the diffusion coefficient (D) and the mean square displacement (MSD). The derivation will be shown in the following by using a microscopic approach.

As a basis, the motion of one particle will be discussed in one dimension, here denoted as x-direction, and transferred to two and three dimensions later. For this purpose, ideal behavior will be assumed, i.e. the motion is not influenced by external factors such as attractive or repulsive interactions with other particles.

According to the kinetic gas theory the mean kinetic energy $\langle E_{kin} \rangle$ of a particle, e.g. along the x-axis, is dependent on the mass m and the mean velocity $\langle v_x \rangle$ along this axis:

$$\langle E_{kin} \rangle = ½ \, m \, \langle v_x^2 \rangle \tag{1}$$

According to the equipartitation principle a molecule possesses an energy E of ½ kT per degree of freedom. Therefore, the mean kinetic energy $\langle E_{kin} \rangle$ along the x-axis is:

$$\langle E_{kin} \rangle = ½ \, kT \qquad \text{k: Boltzmann constant} \tag{2}$$

Combining (1) and (2) gives:

$$\langle v_x^2 \rangle^{1/2} = (kT/m)^{1/2} \tag{3}$$

Thus, the mean velocity of a particle at a given temperature can be calculated if its mass is known. However, the particle is usually not located in vacuum and collisions with other particles or molecules of the surrounding medium can occur. Therefore, the motion is not linear but follows the rules of a so-called random walk. This behavior will be discussed in the following.

2.2.1 Random walk

The motion of one particle performing a random walk will be discussed in one dimension and transferred to two and three dimensions later. The particle starts at time t = 0 at the position x = 0. Further simplifications are used:

1. The entire covered distance x can be dissected into several single steps of the length d. Thereby, the particle moves every time interval τ with a velocity of $\pm v_x$ in one of the two directions and covers the distance $d = \pm v_x\tau$. For reasons of simplification τ, d and thus also v_x will be assumed to be constant. However, in reality both variables are dependent on the size of the particle, the properties of the solvent and the temperature.
2. The steps in both directions have the same probability. The single steps are independent of each other and therefore the particle has no "memory" of the previous steps. Therefore, all successive steps are statistically independent of each other and thus the motion of the particle is not directional.
3. Every particle moves independent of the other particles and has no interactions besides collisions with the surrounding medium. This is in fact only the case for highly diluted solutions.

From these assumptions several implications arise. If all single molecule trajectories of an ensemble were projected to the same origin, then the expectation value of the displacement is $\langle x \rangle = 0$. Therefore, considering only the mean value, the particles seem to remain at the starting point. However, a propagation of the ensemble can be observed over time, i.e. with an increasing number of steps. This can be interpreted as an increase of the standard deviation σ of the travelled distance x:

$$\sigma = \sqrt{\langle x^2 \rangle - \langle x \rangle^2} \tag{4}$$

Since $\langle x \rangle = 0$ the mean square displacement (MSD) $\langle x^2 \rangle$ has to be determined in addition. In n steps the particle covers the following distance:

$$x(n) = x(n-1) \pm d = x(n-1) \pm v_x\tau \tag{5}$$

The square of this distance thus amounts to:

$$x(n)^2 = x(n-1)^2 \pm 2\,x(n-1)\,v_x\tau + (v_x\tau)^2 \tag{6}$$

Extending this to a multi-particle system with N particles after n steps gives:

$$\begin{aligned}\langle x_N^2 \rangle &= \frac{1}{N}\sum_{i=1}^{N}[x_i^2(n-1) \pm 2v_x\tau x_i(n-1) + (v_x\tau)^2] \\ &= \langle x^2(n-1)\rangle + d^2\end{aligned} \tag{7}$$

Since the particle moves the same number of steps forwards as backwards, the second term becomes zero on average. Because one has $x_i(0) = 0$ for all particles i, it follows:

$$\langle x^2(0)\rangle = 0,\ \langle x^2(1)\rangle = 1d^2,\ \langle x^2(2)\rangle = 2d^2,\ \ldots,\ \langle x^2(n)\rangle = nd^2 \tag{8}$$

Therefore, the MSD increases with the number of steps n. The total time t is the sum of the durations of all single steps $n\tau$. The number of steps n and also the MSD are thus directly proportional to the time t. Inserting $n = t / \tau$ in equation (8) gives:

$$\langle x^2(t)\rangle = (t / \tau)\, d^2 = (d^2 / \tau)\, t \tag{9}$$

The time of each single step τ and the step length d can be replaced by the diffusion coefficient D analogue to the macroscopic Fick's Law.[3] Hereby, D is defined as:

$$D = \frac{d^2}{2\tau} \tag{10}$$

The diffusion coefficient is an important measure for the characterization of particle motion. Consisting of the variables τ and d the diffusion coefficient is thus also dependent on the

particle mass, the properties of the solvent and the temperature as stated previously for τ and d.

Inserting equation (10) in (9) results in:

$$\text{1 dim. MSD:} \qquad \langle x^2(t)\rangle = 2Dt \tag{11}$$

The solutions for the one-dimensional problem can be extended to two- and three-dimensional motion with the following estimations: The motions in x-, y- und z-direction are statistically independent of each other, the analogue equations with $\langle x^2(t)\rangle = 2Dt$, $\langle y^2(t)\rangle = 2Dt$ und $\langle z^2(t)\rangle = 2Dt$ for two and three dimensions can be derived:

$$\text{2 dim. MSD:} \qquad r^2 = x^2 + y^2 \quad \Rightarrow \quad \langle r^2(t)\rangle = 4Dt \tag{12}$$

$$\text{3 dim. MSD:} \qquad r^2 = x^2 + y^2 + z^2 \quad \Rightarrow \quad \langle r^2(t)\rangle = 6Dt \tag{13}$$

For some of the experiments presented later in this work only a two-dimensional projection of a three-dimensional diffusion could be measured because the used wide-field technique described in chapter 2.4.2, only allows for two-dimensional imaging. Nevertheless, the diffusion coefficient can still be determined in such a case using the two-dimensional description from equation 12 if the diffusion in the respective system is isotropic.

2.2.2 Deviations from the ideal behavior

For the previous considerations about diffusion, ideal behavior of the particles was assumed. However, under real conditions there are often deviations from this ideal behavior caused by several different reasons. These can be interactions, e.g. hindered diffusion in confined spaces, barriers, adsorption and active transport by flow or in biologic systems. Using Single Molecule Spectroscopy (SMS) the diffusional behavior of single molecules can be investigated.[4] By plotting the MSD extracted from the experimental data versus time insights about the diffusional behavior can be deduced from the shape of the curve. For the most important kinds of diffusion the respective equations and plots (Figure 3) are given in the following:

Normal diffusion: $\langle r^2 \rangle = 2d\,Dt$ (14)

Anomalous diffusion: $\langle r^2 \rangle = 2d\,Dt^{\alpha}$ $0 < \alpha < 1$ (15)

Diffusion with drift: $\langle r^2 \rangle = 2d\,Dt + (vt)^2$ (16)

Confined diffusion: $\langle r^2 \rangle \approx \langle r_c^2 \rangle \left[1 - A_1 e^{\frac{-2dA_2Dt}{\langle r_c^2 \rangle}}\right]$ $A_1, A_2 > 0$ (17)

with d = 1, 2 or 3 for one-, two- or three-dimensional diffusion, respectively.

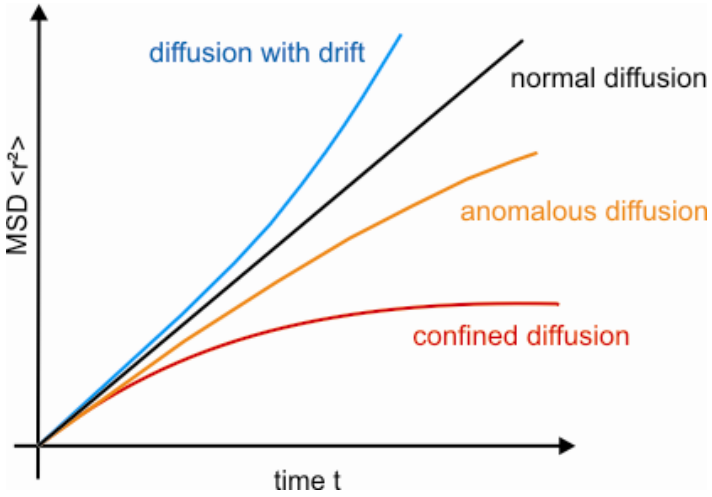

Figure 3: MSD as a function of time for different kinds of diffusion.

In the case of ideal behavior the description for normal diffusion (equation 14) derived in chapter 2.2.1 is correct. However, collisions with obstacles, such as other heavy particles or barriers, can slow down the particle motion. This is called hindered or anomalous diffusion (equation 15). The MSD is in this case proportional to t^{α} instead of t resulting in a convex curve for $\alpha < 1$.[5] In the case of active transport or drift, then equation 16 for diffusion with drift can be used to describe the process. Due to the additional drift the curve gets a concave shape. If a molecule is located inside a confinement (equation 17) then the MSD converges to a distinct value for $t \rightarrow \infty$. This value is influenced by a constant, the so called mean confinement radius $\langle r_c^2 \rangle$. A_1 and A_2 are both constants describing the geometry of the confinement.[6] In porous systems with a small pore diameter different molecules may block each other. This case is called single-file diffusion. Although some of the porous host systems used in this work have a very small pore diameter compared to the size of the guest molecules, however, single-file diffusion should never occur as the concentration of the guest molecules is typically very low. Therefore, they do not encounter and block each other.

2.2.3 Probability distributions

If the position x of a particle after n steps is treated as a stochastic random variable, then the probability distribution of the single steps can be expressed by a binomial or Bernoulli distribution. This distribution can be described by a normal or Gaussian distribution for large factorials taking into account Stirling's approximation:

1 dimension: $$P(x,t) = \frac{1}{\sqrt{4\pi Dt}} e^{-\frac{x^2}{4Dt}} \quad (18)$$

2 dimensions: $$P(r,t) = \frac{1}{\sqrt{4\pi Dt}} e^{-\frac{r^2}{4Dt}} \quad (19)$$

P is the probability of a particle being located in a distance x or r from the starting point after a time t. From the equations 18 or 19 it can be concluded that the probability of finding a particle is highest at the starting position and that the displacement of the particle ensemble increases with time, i.e. with an increasing number of steps (Figure 4). Additionally, a larger amount of particles also increases the overall propagation. For a homogeneous and statistically independent amount of particles, the same diffusion coefficient can be extracted from the time average of a single particle as well as from the ensemble average of a large number of particles, according to the ergodic theorem.[7]

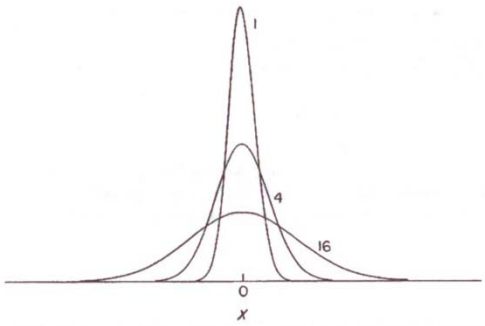

Figure 4: A one-dimensional Gaussian distribution[3] with the probability of finding a particle at the position x for the times t = 1, t = 4 and t = 16. The starting point was x = 0 at t = 0.

In order to obtain the true distribution of diffusion coefficients a method operating at a molecule-by-molecule basis is required. Single molecule fluorescence measurements are ideally suited in this regard. The phenomenon of fluorescence is discussed in the following.

2.3 Fluorescence

Some physical systems, typically specific atoms, molecules, semiconductor or metallic nanoparticles are able to emit fluorescence light spontaneously after excitation by electromagnetic radiation and are therefore called fluorophores. Their electrons can absorb photons which are the quantum of the electromagnetic interaction and the basic "unit" of all forms of electromagnetic radiation. As most fluorophores used in this work are organic dye molecules, the following explanation refers to such molecules. Via photon absorption, the electrons are excited from the ground state S_0 to a vibrational level of a higher excited electronic state, usually the first being S_1 (Figure 5). This process is so fast (about 10^{-15} s) that the atomic nuclei are not able to react and retain their positions, which is known as Frank-Condon principle. Afterwards the vibrational energy is quickly (about 10^{-12} s) dissipated by relaxation via vibrational modes of the particle (vibrational relaxation) and of the surrounding (phonons) to the lowest excited electronic state S_1. The lifetime of this state amounts to about 10^{-9} - 10^{-8} s. Then a radiative transition to a vibrational level of the ground state, the fluorescence, can occur by emitting a photon. The vibrational ground state is then recovered by vibrational relaxation.

Besides fluorescence there are two additional processes competing for restoration of the ground state from the lowest excited electronic state. To begin with, there is a chance for internal conversion (IC) from the latter state to a higher vibrational level of the ground state followed by vibrational relaxation to the vibrational ground state. This process is completely radiationless. Additionally, a transition from the lowest excited electronic state into the triplet state via intersystem crossing (ISC) is possible. This transition is actually forbidden by the selection rules, however, due to spin-orbit interaction it can occur, but typically with a low probability. After relaxation to the lowest vibrational level of the triplet state the excited particle can return to the ground state either by another ISC into the ground state or by emitting a phosphorescence photon, both followed by vibrational relaxation. The lifetime of the triplet state is much longer than the fluorescence lifetime since the transition to the ground state is also "forbidden" and therefore kinetically not favored. It ranges from microseconds up to several minutes or even some hours. Fluorescence and phosphorescence are both forms of luminescence.

The vibrational relaxations, which are in fact energy losses, cause a redshift of the emitted fluorescence or phosphorescence light compared to the absorbed energy. This is one of the two contributors to the so-called Stokes shift. However, in most cases the dominating effect is solvent relaxation. The processes involved in absorption and emission are illustrated by the Jablonski diagram in Figure 5.

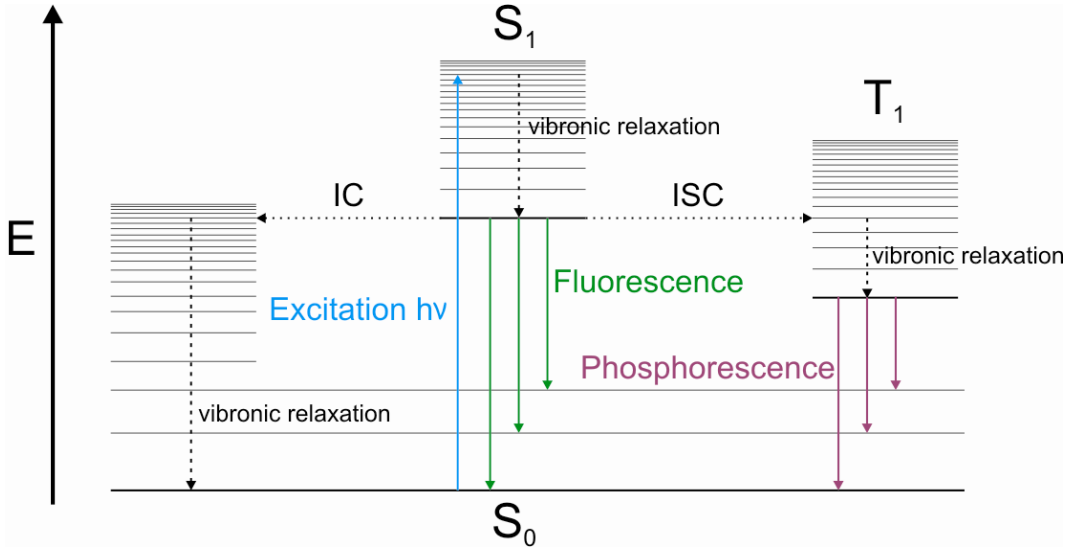

Figure 5: The Jablonski diagram illustrates schematically the electronic and vibrational energy levels of a single dye molecule. Electrons can be excited from the ground state S_0 to the first excited electronic state S_1 by photon absorption. A transition to the lowest triplet state T_1 can occur via ISC. Fluorescence, phosphorescence and radiationless decay restore the ground state.

The absorption and emission spectra, which are utilized to characterize these processes, and the chemical structures of a group of organic dyes used in this work (terrylene diimide derivatives, AS-TDI, DIP-TDI and SW-TDI) are shown as an example in Figure 6. Those spectra of the three TDI dyes are very similar, because all three dyes posses the same terrylene diimide core, which is responsible for the photophysical properties. The substituents do not influence the π–system of the dyes. The data were measured with a Perkin Elmer 330 dual-beam spectrometer and using chloroform as solvent.

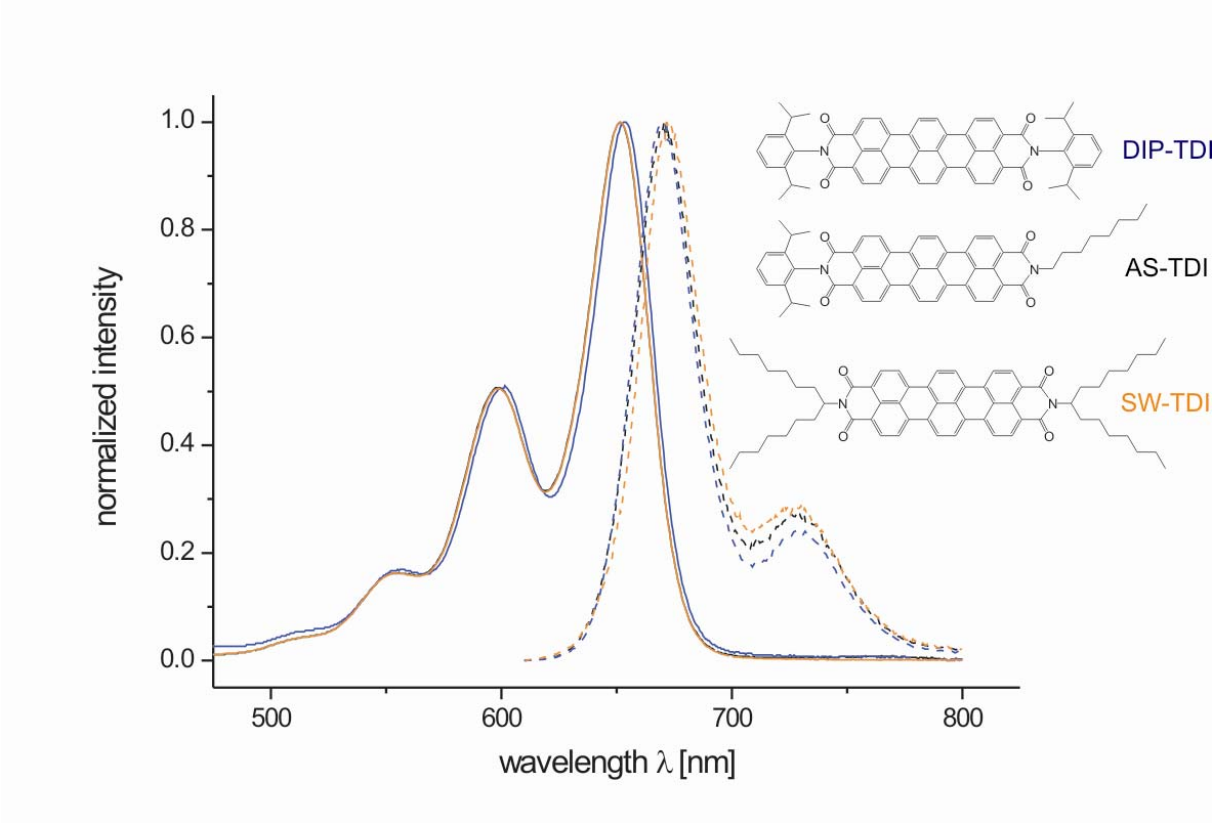

Figure 6: Normalized absorption (straight lines) and emission (dashed lines) spectra of AS-TDI (black), DIP-TDI (blue) and SW-TDI (orange). Their respective chemical structures are shown as inset. The Stokes shift of 20 nm between the absorption and emission maxima at 650 nm and 670 nm, respectively, is clearly visible.

These TDI dyes exhibit excellent photo-physical properties for single molecule spectroscopy which will be explained in the following. In order to absorb as many photons as possible, the absorption cross section σ (equation 20), which is a measure for the probability of an absorption process, has to be high. Therefore, higher signal-to-noise ratios can be obtained compared to using weak absorbing dyes.

$$\frac{dN}{dx} = -Nn\sigma \tag{20}$$

The number of photons absorbed between the points x and x + dx along the path of a beam is dN. N is the number of photons penetrating to depth x and n the number of absorbing molecules per unit volume.

The fluorescence quantum yield is defined as the ratio of the number of emitted photons to the number of photons absorbed or as the ratio of the radiative decay rate to the sum of all (radiative k_{rad} and nonradiative k_{nonrad}) decay rates (equation 21).

$$\Phi_F = \frac{N_{emitted\ photons}}{N_{absorbed\ photons}} = \frac{k_{rad}}{k_{rad}+k_{nonrad}} \quad (21)$$

Therefore, the quantum yield describes the efficiency of the fluorescence process and has a maximum value of 1.0 (= 100%). Good fluorescent dyes such as the TDI derivatives possess a quantum yield close to unity due to their relatively rigid structure which prevents deactivation of the excited state via nonradiative vibrational channels. Thus, these dyes provide a sufficient brightness for single molecule detection.

However, there are also processes which affect the emitted signal and the time over which a single molecule can be observed. These typically include the reversible (photoblinking) or irreversible (photobleaching) transition to a dark state. Photoblinking is usually caused by a transition to the triplet state, which has a relatively long lifetime as explained above, but also other effects are possible.[8, 9] Photobleaching can be induced by irreversible photo-degradation of the fluorophore, mainly photo-oxidation, and limits the time a molecule can be observed. Therefore, exclusion of oxygen or addition of reducing agents can increase the observation time before photobleaching. However, photobleaching is still not well understood in many cases.[10, 11] Both processes, photoblinking and photobleaching, are typical features of single molecules and can be used to clearly indentify those.

2.4 Single molecule spectroscopy

Single molecule spectroscopy (SMS) includes a wide range of methods enabling the detection of single fluorophores, typically at very low concentrations. The fluorophore is usually excited by a light source, for example a laser, and the corresponding spectral signal is then detected by a highly sensitive detector.

Single molecule experiments provide the actual true distribution of a measured variable showing for example the local heterogeneities of the surrounding medium at the nanometer scale for each molecule. Using ensemble methods, which provide only a mean value of the true distribution, the influence of such a locally heterogeneous environment on the behavior of structurally identical molecules is hidden due to averaging. Therefore, SMS has become a widely used tool in numerous scientific fields, ranging from fundamental research in physics, chemistry and biology[12-16] to material science[17, 18, 19] or nano-medicine.[20-22]

In the following the basic principles of fluorescence microscopy will be explained first. Afterwards several common techniques for the detection of single molecules will be presented including a more detailed experimental description of the wide-field setup mostly used in this work. The last section will cover the analysis of the data gained by single molecule experiments using single particle tracking (SPT).

2.4.1 Principles

The first single dye molecules were detected by their absorption[23] or fluorescence excitation spectra.[24] However, the absorption cross section of most dye molecules is usually some orders of magnitude smaller compared to the area exposed to a focused laser beam. Therefore, the detection of single molecule absorption versus the shot noise of not absorbed photons is very challenging and thus the signal-to-noise ratio is quite low. This is why such experiments had to be performed at very low temperatures. Meanwhile highly effective interference filters have been developed allowing for precise separation of the reflected or scattered excitation light and the red-shifted fluorescence of single fluorophores. Additionally novel immersion objectives with high numerical apertures (NA) are able to

gather an extensive fraction of the emitted light and thus provide high detection efficiencies. Therefore, the detection of single molecules via their fluorescence has become common and is employed in various techniques resulting in an excellent signal-to-noise ratio even at room temperature.

Due to diffraction of light, the image of a single molecule, which can be considered as a point emitter since it is much smaller than the wavelength λ, is not a small point. Rather it is a diffraction pattern, the so-called Airy disc. This diffraction pattern is often detected as a broadened spot. The lateral resolution in optical light microscopy is defined as the smallest distance of two such point emitters that still allows for the detection of each of them as spatial separated signal. According to the Rayleigh criterion, this minimal distance is defined as:

$$r_{Rayleigh} = 0.61 \frac{\lambda}{NA} \qquad \text{with } NA = \mathrm{n} \cdot \sin \alpha \tag{22}$$

λ is the wavelength of light and NA the numerical aperture of the objective lens, which is defined as the index of refraction of the sample medium times the sinus of the half collection angle α of the objective lens. Therefore, the lateral resolution increases with higher NA values of the objective. Using typical settings with an 1.4 NA objective and red or green laser light excitation at λ = 633 nm or λ = 532 nm and respective fluorescence detection, the lateral resolution is about 300 nm or 250 nm, respectively. However, utilizing SMS and SPT allows overcoming this resolution limit and achieving a positioning accuracy down to the nanometer regime. Details will be given in the last section addressing SPT.

Most single molecule microscopy techniques can be classified into one of two basic setup principles, namely wide-field or confocal microscopy methods. These two methods differ in the excitation and detection geometry of the setup. Wide-field and confocal microscopy methods both have characteristic advantages and disadvantages. Therefore, the appropriate method has to be chosen carefully for each specific study. In the following both methods will be described in more detail.

2.4.2 Wide-field fluorescence microscopy

In wide-field microscopy an area of typically several micrometers of the sample and thus numerous fluorophores are illuminated simultaneously. Using an array detector, such as a charge-coupled device (CCD) camera, allows then for the emitted fluorescence signals to be collected at once. In addition CCD technology nowadays enables to record several thousands of consecutive images and more importantly it is also possible to achieve very high frame rates. Therefore, the use of wide-field techniques is advantageous when observing many molecules at the same time in micron-sized areas or studying fast processes. In order to study the diffusion processes investigated in this work, a high temporal resolution is required and this is why wide-field microscopy has been used in the majority of cases.

Conventional wide-field microscopes, such as the setup used in this work, are built for epi-fluorescence detection, i.e. the same objective is used for focusing the excitation beam on the sample and gathering the fluorescence signals. Thereby, the amount of background signal arising from incident excitation light can be reduced.

The detailed setup of the wide-field microscope used in this work is explained in the following.

Wide-field microscopy setup

A schematic view of the wide-field microscopy setup used in this work is shown in Figure 7. Samples can be excited at 632.8 nm with a He-Ne gas laser (Coherent) or at 532 nm with a diode pumped solid-state laser (Cobolt Samba TM Laser). Respective laser line filters (Laser Components GmbH) are used to narrow down the laser bandwidth. The laser intensities can be regulated by optical density (OD) filter wheels (OD 0-2, Thorlabs). Using two mirrors and a dichroic mirror both laser beams are guided onto an achromatic lens L1 (f = 50 mm, Thorlabs) which couples the light into an optical multimode fibre (0.6 mm in diameter, Optronics GmbH) used as a spatial filter. In order to eliminate interference patterns at the fibre exit, a motor steadily shaking the fibre is used. The light exiting the fibre is parallelized by a second achromatic lens L2 (f = 50 mm, Thorlabs). A home-built quadratic aperture is used to reduce the size of the circular laser beam to the quadratic region of interest (ROI) of the CCD camera to prevent photobleaching in sample areas outside this ROI. The image of this quadratic aperture is then focused on the back focal plane of the high NA oil-immersion

objective (CFI Plan Apochromat 100x, 1.40 NA oil, Nikon) by the achromatic wide-field lens L3 (f = 200 mm, Thorlabs) in the epifluorescence microscope (Eclipse TE200, Nikon). Therefore, the sample is illuminated in wide-field mode by a parallel beam exiting the objective in a quadratic area of about 30 µm times 30 µm corresponding to the image of the quadratic aperture on the sample. Alternatively the samples can be illuminated by a built-in white light source of the microscope adjusted for Köhler illumination in transmission mode.

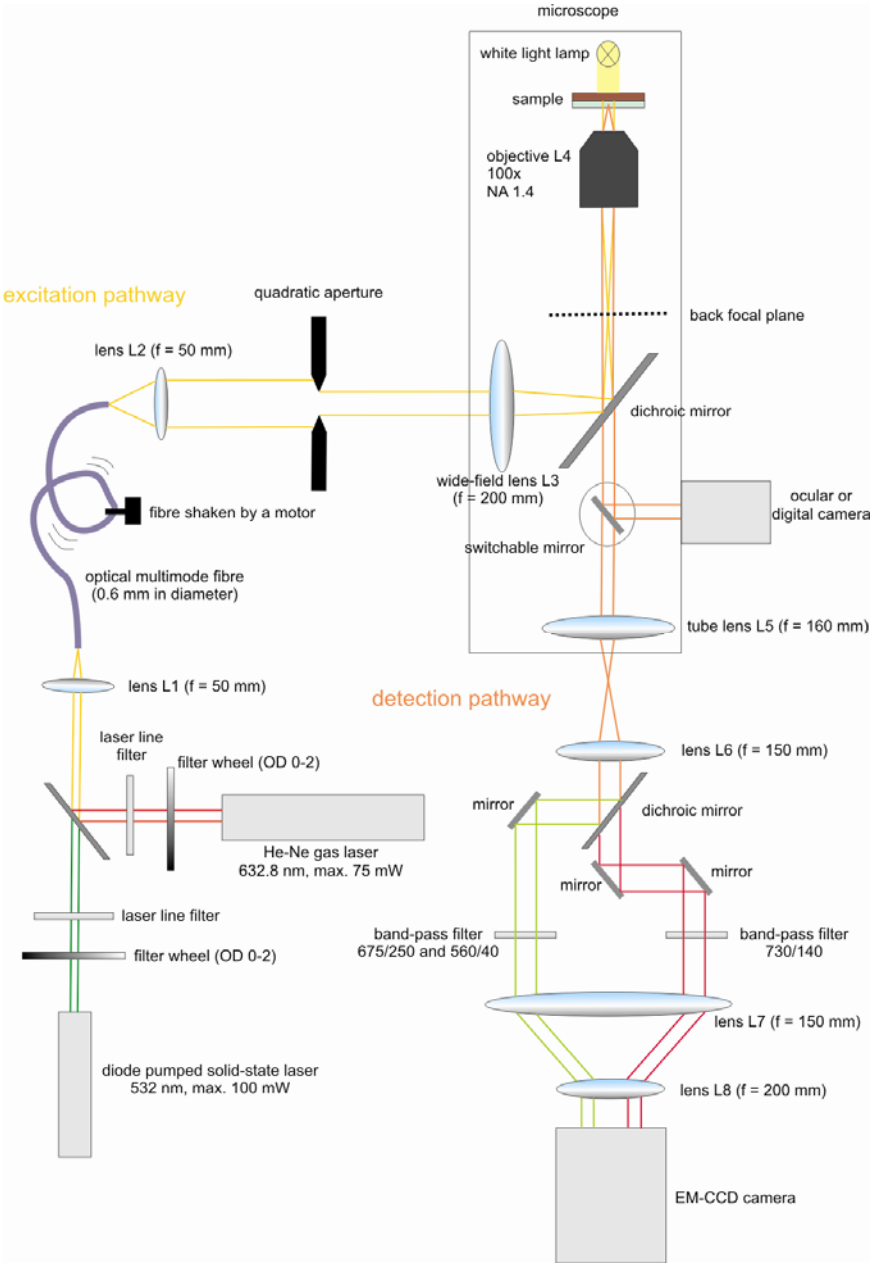

Figure 7: Wide-field microscopy setup. The sample is illuminated by a widened parallel beam. Fluorescence light is separated from incident laser light by a dichroic mirror and band-pass filters. The images are recorded by a EM-CCD camera.

The initial detection pathway was rebuilt and modified in order to be able to visualize not only one detection channel (red or green fluorescence) at a time as before, but both simultaneously. Such a setup was required for example for the studies described in chapter 4.1. The fluorescence of the single fluorophores, which can be considered as point like emitters, is gathered by the objective lens L4. The red-shifted fluorescence light is separated from scattered laser light by a dichroic mirror (dual line beamsplitter 532/633, AHF Analysentechnik). The emission light is then exiting the microscope through a tube lens L5 (f = 160 mm). The lenses L6 (f = 150 mm) and L8 (f = 200 mm) form a telescope magnifying the image by a factor of 1.33. Altogether that results in a total magnification of 133 when using the 100x objective described above. This value has been adjusted to give an optimal image of the ROI on the CCD chip. In between the telescope lenses a dichroic mirror splits green and red fluorescence light into two separate parallel beams. The specific home-built arrangement of mirrors in both beam paths ensures equal lengths of both pathways. Remaining incident laser light is blocked by exchangeable high quality band-pass filters in both beams separately (typically 675/250 and 560/40 for the green channel and 730/140 for the red channel, AHF Analysentechnik). Using another lens (f = 150 mm), both green and red fluorescence is then guided to the latter telescope lens L8 and focused onto the CCD chip with a small lateral shift between them. Fluorescence signals are detected with a back-illuminated electron-multiplying CCD (EM-CCD) camera in frame transfer mode (iXon DV897, 512x512 pixels, Andor). According to measurements using a USAF test-pattern (Melles Griot) a sample size of 154 nm corresponds to one pixel on the camera. Therefore, the images taken with the rebuilt detection setup are smaller on the CCD chip than before with a value of 122 nm per pixel. With the previous setup an image of the total ROI amounted to 256x256 pixels on the CCD chip. However, two images corresponding to the separated detection channels of green and red fluorescence with each of 256x256 pixels in size on a 512x512 pixels chip would result in an overlap of both detection channels. To prevent this, a small gap of several pixels is left in between both channels and this is why each channel now amounts to a size smaller than 256x256 pixels on the CCD chip. Using a switchable mirror in the microscope, the light can alternatively be guided to a digital camera for focus alignment or in the case of a white light source to an ocular.

2.4.3 Confocal fluorescence microscopy

In confocal microscopy the laser beam used for excitation of the fluorophores is focused to a diffraction limited volume, also called confocal volume. Utilizing a point detector, such as a photomultiplier tube or an avalanche photodiode (APD), fluorescence light is only collected from this confocal volume. Additionally out of focus fluorescence can be excluded by inserting a pinhole in the detection pathway. This is why high axial resolution of about 900 nm (compared to about 1-2 µm in wide-field imaging) is achieved by default in confocal microscopy. Images can also be obtained by scanning the sample, however, due to this scanning process the acquisition of images is considerably slower than in wide-field microscopy.

In addition to translational information of a single molecule also further viable single molecule data can be collected using confocal microscopy. For example the orientation of single molecules can be studied by inserting a polarizer into the excitation and detection pathway.[25, 26] Furthermore, it is also possible to record the spectrum of a selected single molecule using a prism or grating to spectrally split the fluorescence signal onto a CCD camera.[25] A schematic view of a confocal setup also used in this work is shown in Figure 8.

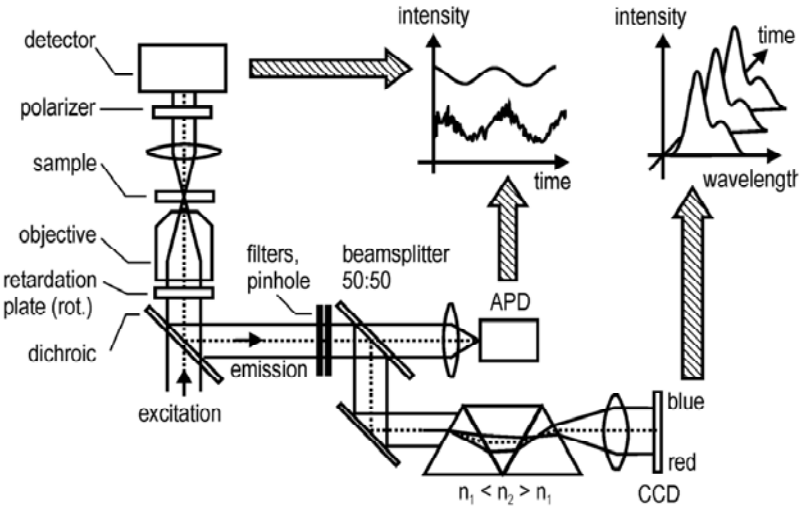

Figure 8: Confocal microscopy setup. A diffraction-limited confocal volume of the sample is illuminated by a focused beam. Fluorescence light is separated from incident laser light by a dichroic mirror and band-pass filters as described before for the wide-field setup. Out-of-plane fluorescence is excluded by a pinhole in the detection pathway. Adapted from [27].

2.4.4 Single particle tracking

The limit of the achievable resolution in optical light microscopy is given by the Rayleigh criterion as explained before. However, it is possible to localize the position of the single fluorophore with higher accuracy. The diffraction limited spot of the single fluorophore signal (Airy disc pattern) can be described as response of the imaging system by the so-called point spread function (PSF). In single molecule experiments the concentration of the fluorophores is typically so low that the average distance between two adjacent emitters is large enough to resolve each of them individually by its PSF. This PSF can be described by a first order bessel function[28] and be approximated well by a two dimensional Gaussian function:[29-31]

$$f(x,y) = A \cdot e^{\left(-\frac{(x-x_0)^2+(y-y_0)^2}{2\sigma^2}\right)} \qquad \text{with } 2\sigma^2 = \omega^2 \tag{23}$$

Hereby the peak position (x_0 and y_0) of the Gaussian can be extracted from the measured data with a high positioning accuracy down to the nanometer range using this equation and a χ^2 minimization. The positioning accuracy is defined as the range in which the true centre of the single molecule is localized with a probability of 68 %. This corresponds to the standard deviation of the approximation of x_0 and y_0. A is the amplitude of the fluorescence signal, σ the radial variance and ω the width of the Gaussian. The determined peak position of the Gaussian is then taken as the position of the single molecule.

The fit given above can be applied in the usual case of the single molecules either rotating freely or having their transition dipole moment not oriented parallel to the optical axis. However, in the special case of the transition dipole moment of a single fluorophore oriented parallel to the optical axis for a time longer than the time resolution of the setup, the diffraction pattern of the corresponding fluorescence signal will be shaped like a "doughnut".[32-37] Therefore, the PSF has to be fitted with a product of the Gaussian given above and a sine squared function:

$$f(x,y) = A \cdot e^{\left(-\frac{(x-x_0)^2+(y-y_0)^2}{2\sigma^2}\right)} \cdot \sin^2\left(\frac{\pi\sqrt{(x-x_0)^2+(y-y_0)^2}}{2r}\right) \tag{24}$$

The quality of SPT and thus the positioning accuracy are influenced by several experimental parameters, which are summarized in the signal-to-noise ratio (SNR).[38] An important factor influencing the detected signal intensity is the brightness of the fluorophore. This is why a high absorption cross section and a high quantum yield of the fluorophore is desirable. The two major contributors to noise are background noise and shot noise. Background noise is induced by out-of-plane fluorescence from fluorophores outside the focal plane. Shot noise is associated with the particle nature of light. If the number of photons, i.e. the quantized unit of light, per time interval is low, then statistical variations in the detected number of photons per pixel will be significant. Since the standard deviation of shot noise is equal to the square root of the number of detected photons N, the SNR is also proportional to the square root of N. Therefore, if N is high, the SNR is high as well, and any statistical variations in N due to other sources are more likely to dominate over shot noise. Furthermore, it can be derived for the positioning accuracy:

$$\Delta(x, y) \sim \frac{1}{SNR} \sim \frac{1}{\sqrt{N}} \tag{25}$$

Applying the SPT routine to several consecutive images of the observed fluorophores from a recorded movie and thus by fitting frame by frame theoretical diffraction patterns to the fluorescence spots, provides the positions of the single fluorophores over time. These time correlated positions of one single molecule are called trajectory. By analyzing these trajectories with respect to the MSDs, yields the single molecule diffusion coefficients by fitting the linear part of the MSD plots according to the Einstein-Smoluchowski relation described in chapter 2.2. Thereby, the diffusional behavior of the single molecules but also structural information of the surrounding medium, for example a porous host matrix, can be investigated. Several examples of insights into diffusion in various nanoporous materials provided by SPT are presented in the following chapters.

References

1. D. H. Everett, L. K. Koopal, Manual of Symbols and Terminology for Physicochemical Quantities and Units - Appendix II: Definitions, Terminology and Symbols in Colloid and Surface Chemistry. *International Union of Pure and Applied Chemistry (IUPAC)*, (1971).
2. C. J. Brinker, Y. Lu, A. Sellinger, H. Fan, Evaporation-Induced Self-Assembly: Nanostructures Made Easy. *Advanced Materials* **11**, 579 (1999).
3. H. C. Berg, *Random Walks in Biology*. (Princeton University Press, 1993).
4. M. J. Saxton, K. Jacobsen, Single-Particle Tracking: Applications to membrane Dynamics. *Annual Review of Biophysics and Biomolecular Structure* **26**, 373 (1997).
5. T. J. Feder, I. Brust-Mascher, J. P. Slattery, B. Baird, W. W. Webb, Constrained diffusion or immobile fraction on cell surfaces: a new interpretation. *Biophysical Journal* **70**, 2767 (1996).
6. M. J. Saxton, Lateral diffusion in an archipelago. Single-particle diffusion. *Biophysical Journal* **64**, 1766 (1993).
7. G. D. Birkhoff, Proof of the ergodic theorem. *Proceedings of the National Academy of Sciences of the United States of America* **17**, 656 (1931).
8. W. P. Ambrose, P. M. Goodwin, J. C. Martin, R. A. Keller, SINGLE-MOLECULE DETECTION AND PHOTOCHEMISTRY ON A SURFACE USING NEAR-FIELD OPTICAL-EXCITATION. *Physical Review Letters* **72**, 160 (1994).
9. R. Zondervan, F. Kulzer, S. B. Orlinskii, M. Orrit, Photoblinking of rhodamine 6G in poly(vinyl alcohol): Radical dark state formed through the triplet. *Journal of Physical Chemistry A* **107**, 6770 (2003).
10. C. Eggeling, J. Widengren, R. Rigler, C. A. M. Seidel, Photobleaching of fluorescent dyes under conditions used for single-molecule detection: Evidence of two-step photolysis. *Analytical Chemistry* **70**, 2651 (1998).
11. R. Zondervan, F. Kulzer, M. A. Kol'chenko, M. Orrit, Photobleaching of rhodamine 6G in poly(vinyl alcohol) at the ensemble and single-molecule levels. *Journal of Physical Chemistry A* **108**, 1657 (2004).
12. S. Weiss, Fluorescence spectroscopy of single biomolecules. *Science* **283**, 1676 (1999).
13. P. Tamarat, A. Maali, B. Lounis, M. Orrit, Ten years of single-molecule spectroscopy. *Journal of Physical Chemistry A* **104**, 1 (2000).
14. G. Seisenberger *et al.*, Real-time single-molecule imaging of the infection pathway of an adeno-associated virus. *Science* **294**, 1929 (2001).
15. W. E. Moerner, A dozen years of single-molecule spectroscopy in physics, chemistry, and biophysics. *Journal of Physical Chemistry B* **106**, 910 (2002).
16. F. Kulzer, M. Orrit, Single-molecule optics. *Annual Review of Physical Chemistry* **55**, 585 (2004).
17. J. Kirstein *et al.*, Exploration of nanostructured channel systems with single-molecule probes. *Nature Materials* **6**, 303 (2007).
18. D. A. Vanden Bout *et al.*, Discrete intensity jumps and intramolecular electronic energy transfer in the spectroscopy of single conjugated polymer molecules. *Science* **277**, 1074 (1997).
19. A. Zürner, J. Kirstein, M. Döblinger, C. Bräuchle, T. Bein, Visualizing single-molecule diffusion in mesoporous materials. *Nature* **450**, 705 (2007).

20. C.-Y. Lai *et al.*, A Mesoporous Silica Nanosphere-Based Carrier System with Chemically Removable CdS Nanoparticle Caps for Stimuli-Responsive Controlled Release of Neurotransmitters and Drug Molecules. *Journal of the American Chemical Society* **125**, 4451 (2003).
21. V. Cauda *et al.*, Colchicine-Loaded Lipid Bilayer-Coated 50 nm Mesoporous Nanoparticles Efficiently Induce Microtubule Depolymerization upon Cell Uptake. *Nano Letters* **10**, 2484 (2010).
22. A. Schlossbauer *et al.*, A Programmable DNA-Based Molecular Valve for Colloidal Mesoporous Silica. *Angewandte Chemie International Edition* **49**, 4734 (2010).
23. W. E. Moerner, L. Kador, OPTICAL-DETECTION AND SPECTROSCOPY OF SINGLE MOLECULES IN A SOLID. *Physical Review Letters* **62**, 2535 (1989).
24. M. Orrit, J. Bernard, SINGLE PENTACENE MOLECULES DETECTED BY FLUORESCENCE EXCITATION IN A PARA-TERPHENYL CRYSTAL. *Physical Review Letters* **65**, 2716 (1990).
25. C. Jung, C. Hellriegel, J. Michaelis, C. Bräuchle, Single-molecule traffic in mesoporous materials: Translational, orientational, and spectral dynamics. *Advanced Materials* **19**, 956 (2007).
26. C. Jung *et al.*, Simultaneous measurement of orientational and spectral dynamics of single molecules in nanostructured host-guest materials. *Journal of the American Chemical Society* **129**, 5570 (2007).
27. C. Jung, Single Molecule Traffic in Mesoporous Materials and New Photostable Water-Soluble Terrylenediimide Derivates. PhD Thesis, LMU Munich (2007).
28. U. Kubitscheck, O. Kückmann, T. Kues, R. Peters, Imaging and tracking of single GFP molecules in solution. *Biophysical Journal* **78**, 2170 (2000).
29. C. M. Anderson, G. N. Georgiou, I. E. G. Morrison, G. V. W. Stevenson, R. J. Cherry, TRACKING OF CELL-SURFACE RECEPTORS BY FLUORESCENCE DIGITAL IMAGING MICROSCOPY USING A CHARGE-COUPLED DEVICE CAMERA - LOW-DENSITY-LIPOPROTEIN AND INFLUENZA-VIRUS RECEPTOR MOBILITY AT 4-DEGREES-C. *Journal of Cell Science* **101**, 415 (1992).
30. G. J. Schütz, H. Schindler, T. Schmidt, Single-molecule microscopy on model membranes reveals anomalous diffusion. *Biophysical Journal* **73**, 1073 (1997).
31. M. K. Cheezum, W. F. Walker, W. H. Guilford, Quantitative comparison of algorithms for tracking single fluorescent particles. *Biophysical Journal* **81**, 2378 (2001).
32. W. Lukosz, R. E. Kunz, LIGHT-EMISSION BY MAGNETIC AND ELECTRIC DIPOLES CLOSE TO A PLANE DIELECTRIC INTERFACE .2. RADIATION-PATTERNS OF PERPENDICULAR ORIENTED DIPOLES. *Journal of the Optical Society of America* **67**, 1615 (1977).
33. R. M. Dickson, D. J. Norris, W. E. Moerner, Simultaneous imaging of individual molecules aligned both parallel and perpendicular to the optic axis. *Physical Review Letters* **81**, 5322 (1998).
34. A. P. Bartko, R. M. Dickson, Imaging three-dimensional single molecule orientations. *Journal of Physical Chemistry B* **103**, 11237 (1999).
35. A. P. Bartko, R. M. Dickson, Three-dimensional orientations of polymer-bound single molecules. *Journal of Physical Chemistry B* **103**, 3053 (1999).
36. M. Böhmer, J. Enderlein, Orientation imaging of single molecules by wide-field epifluorescence microscopy. *Journal of the Optical Society of America B-Optical Physics* **20**, 554 (2003).
37. R. J. Pfab *et al.*, Aligned terrylene molecules in a spin-coated ultrathin crystalline film of p-terphenyl. *Chemical Physics Letters* **387**, 490 (2004).

38. N. Bobroff, Position measurement with a resolution and noise-limited instrument. *Review of Scientific Instruments* **57**, 1152 (1986).

3 Single-particle and ensemble diffusivities - Test of ergodicity

F. Feil*, S. Naumov*, J. Michaelis, R. Valiullin, D. Enke, J. Kärger, C. Bräuchle, Single-Particle and Ensemble Diffusivities - Test of Ergodicity. *Angewandte Chemie* **124**, 1178 (2012) / *Angewandte Chemie International Edition* **51**, 1152 (2012).

[∗] These authors contributed equally to this work.

Author contributions

F.F. conceived and performed the single molecule experiments and analyzed the single molecule data. S.N. conceived and performed the PFG-NMR experiments and analyzed the PFG NMR data.

Diffusion is the omnipresent, random motion of matter such as atoms and molecules, driven by thermal energy and is key for innumerable processes in nature and technology.[1-4] In nearly every chemical reaction diffusion is the key mechanism of bringing the reactants in close proximity, which is an essential prerequisite before any reaction can occur. Additionally many reactions are diffusion controlled, meaning that the reaction kinetic is limited by the diffusion process. Central to the dynamics of diffusion, and in general matter, is the ergodic theorem,[5] which states that for systems under equilibrium the time average taken over a single particle is the same as the ensemble average over many particles. However, while being generally accepted no experimental validation has so far been reported. Here, we present experimental proof of this fundamental theorem by measuring under identical conditions the diffusivities of guest molecules inside a nano-structured porous glass using two conceptually different approaches. The data obtained through the direct observation of dye molecule diffusion by single-molecule tracking experiments,[6-8] i.e. the time-average, is in perfect agreement with the ensemble value obtained in pulsed field gradient NMR experiments.[9, 10]

After one and a half centuries of diffusion measurements with large ensembles of diffusing particles,[11] the option of single-particle tracking (SPT) with single molecule sensitivity has recently provided us with a totally new view of diffusion. In this approach, the trajectory of a

single, optically-labeled molecule can be recorded during a sufficiently long interval of time. The thus obtained trajectory can thereafter be analyzed to access, e.g., the average value of the squared displacement $r^2(t)$ of a diffusing particle during a time interval *t*

$$\langle r^2(t)\rangle_{time} = \lim_{T\to\infty} \frac{1}{T-t}\int_0^{T-t}\big(r(\tau+t)-r(\tau)\big)^2 d\tau. \quad (1)$$

Exactly this quantity is in the most straightforward way measured using the diffusion gradient NMR technique. Here, however, the mean square displacements measured is an average taken over about 10^{20} diffusing species:

$$\langle r^2(t)\rangle_{ensemble} = \iint_{r,r_0}(r-r_0)^2 p(r_0)\,P(r,t;\,r_0)\,dr\,dr_0 \quad (2)$$

where $p(r_0)$ and $P(r, t; r_0)$ denote, respectively, the ("a priori") probability that a molecule is found at position r_0 within the sample and the ("conditional") probability that, after time *t*, a molecule has moved from r_0 to *r*. For both r_0 and *r*, the integration extends over the whole sample space.

The direct comparison of these two quantities obtained for one and the same system may yield essential information on microscopic mechanisms of mass transfer in systems exhibiting deviations from normal diffusion including out-of-equilibrium situations[12-14] and, more generally, ergodicity breaking.[15] However this is an extremely difficult experimental problem. That is why even the seemingly simple case of equilibrium systems, forming the basis for the proof of the ergodic theorem, so far remained unregarded in the literature.

To date, the mutually contradicting measuring conditions have prohibited the application of ensemble and single-particle techniques to one and the same system: The trajectory of a diffusing single molecule is constructed by fitting the position of the molecule over time with SPT.[6] Therefore, the fluorescence signals of the molecules have to be clearly separated from each other, which requires very low concentrations. Additionally the measurements are limited by the signal-to-noise ratio, which is influenced by the brightness of the dye molecules as well as the integration time. Consequently there is an upper limit for the detectable diffusivity in SPT. Exactly the opposite conditions, namely high concentrations

(for generating sufficiently strong signal intensities) and high diffusivities (for giving rise to observable displacements) must be fulfilled for the application of the pulsed field gradient (PFG) technique of NMR, representing the most powerful ensemble technique for diffusion studies.

Bridging the gap between SPT and ensemble measurement did thus require a thoughtful selection of both the probe molecule and the host system. Among a large variety of fluorescing molecules, Atto532 (ATTO532-COOH, ATTO-TEC, Siegen, Germany) dissolved in deuterated methanol offered particularly favorable properties for both techniques, namely a large enough transverse nuclear magnetic relaxation time for PFG NMR (see the Methods section in the Supporting Information) and a sufficient photostability and quantum yield for single molecule spectroscopy. Both single-particle observation[16] and PFG NMR ensemble studies[17] have revealed porous glasses as a most versatile host system for diffusion studies. Moreover, with the option of a continuous variation of the mean pore diameter[18] porous glasses offer the unique option to “adjust” the guest diffusivities to those values where the sensitivity ranges of SPT and ensemble measurements overlap.

So far, the application of porous glasses as a standard material for diffusion measurements in nanopores was limited by the fact that the lower limit of controlled pore sizes in monolithic material has been on the order of 4 nm, as a consequence of uncontrolled phase separation in the sodium borosilicate initial glass melt.[18] This limitation has now been overcome by a modified roller-quenching process[19] in combination with an optical fine cooling[20] so that the fabrication of nanoporous glasses with a homogeneous pore surface and pore diameters down to 1 nm have now become possible.[21] In the presented studies we used such glasses with a random three-dimensional pore structure and pore sizes of 3 nm as determined from nitrogen adsorption at 77 K (see the Supporting Information).

First, diffusion properties of dye molecules in the nanoporous host were studied using gradient NMR. In order to solely detect the NMR signal of the dye molecules under study, we have chosen deuterated methanol as a solvent and tuned the working NMR frequency of the spectrometer to that of protons residing on the dye. The NMR samples prepared (see the Methods section in the Supporting Information) contained both solutions within the pores as

well as some excess bulk phase. Thus, there existed two populations of the dye molecules with different diffusion properties, with faster diffusivities in the bulk and with slower diffusivities in the pore system due to confinements,[17] with the relative weights determined by dynamic equilibrium between the two "phases". Consequently, the primary quantity measured, namely the NMR spin-echo diffusion attenuation Ψ, had been contributed by both ensembles:[10, 22]

$$\Psi(q,t) = p_{pore}e^{-q^2tD} + \left(1 - p_{pore}\right)e^{-q^2tD_{bulk}}. \quad (3)$$

In equation 3, q is the wave number externally controlled in the experiments, p_{pore} is the relative fraction of dye molecules in the pores, D_{bulk} and D are the diffusivities of dye molecules in the bulk solution and in the solution within the pores. Notably, the use of the sum of two exponential functions, uncoupled from one another, in equation 3 is fully justified by the fact that, due to macroscopic extension of the porous monolith, molecular exchange between the two ensembles during the diffusion times of the order of tens of ms used in our experiments was negligibly small.[22]

Figure 1 shows a typical PFG NMR spin-echo diffusion attenuation of a dye ensemble with the solid line being the fit of equation 3 to the experimental data. Notably, the experiments performed with varying diffusion time t yielded the diffusivities which, in the considered interval from 5 to 100 ms, did not depend on the observation time, thus revealing normal diffusion. Exactly the thus obtained diffusivities D are further shown in Figure 3.

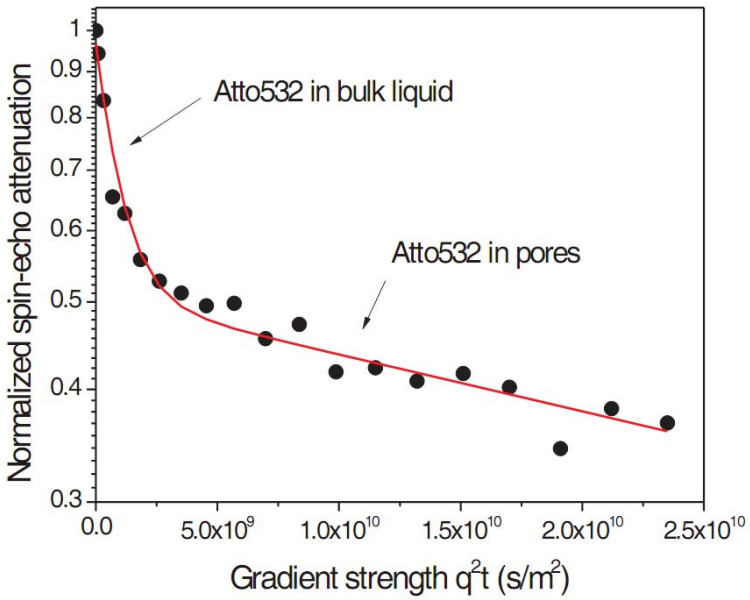

Figure 1: PFG NMR spin-echo diffusion attenuation of a dye ensemble. Data are fitted with a bi-exponential decay thus accounting for diffusion inside the pores and in excess medium.

The diffusion of dye molecules in the glass material was studied additionally by single-molecule fluorescence microscopy (see the Methods section in the Supporting Information). By collecting several fluorescence images of the single molecules using wide-field microscopy and determining the position of the molecules in each image, single-molecule trajectories are obtained (an example can be seen in Figure 2a.) The diffusion coefficient for each single molecule trajectory can be extracted from the linear part of the mean square displacement (MSD) plots according to $\langle r^2(t)\rangle = 4Dt$ assuming an isotropic Brownian diffusion in all three dimensions and keeping in mind that the fluorescence images correspond to a two-dimensional projection of the three-dimensional diffusion. An isotropic Brownian motion is justified by the fact that the particle diffuses in a three-dimensional pore structure und the displacements followed in the experiments exceed the pore diameters by orders of magnitude. In order to test whether diffusion is dependent on dye concentration at low filling ratios, we performed experiments at increasing concentrations keeping in mind that the signal separation of different single dye molecules and out-of-plane fluorescence becomes limiting at higher concentrations. The MSDs of 170 single Atto532 molecules from samples with concentrations of 3.2×10^{-11} mol / l, 3.2×10^{-10} mol / l and 6.4×10^{-10} mol / l were measured. As an example the MSD plots of 70 single molecules of a concentration of 3.2×10^{-11} mol / l are shown in Figure 2b. The MSD plots compare well with other examples

of single molecule diffusion.[23] Additionally the cumulative distribution of the logarithm of the single molecule diffusivities of this sample is depicted in Figure 2c. Both distributions show the heterogeneity of diffusion for different molecules, which is hidden to ensemble measurements due to averaging. The data are fitted to a log-normal distribution using a maximum likelihood estimation (red line).

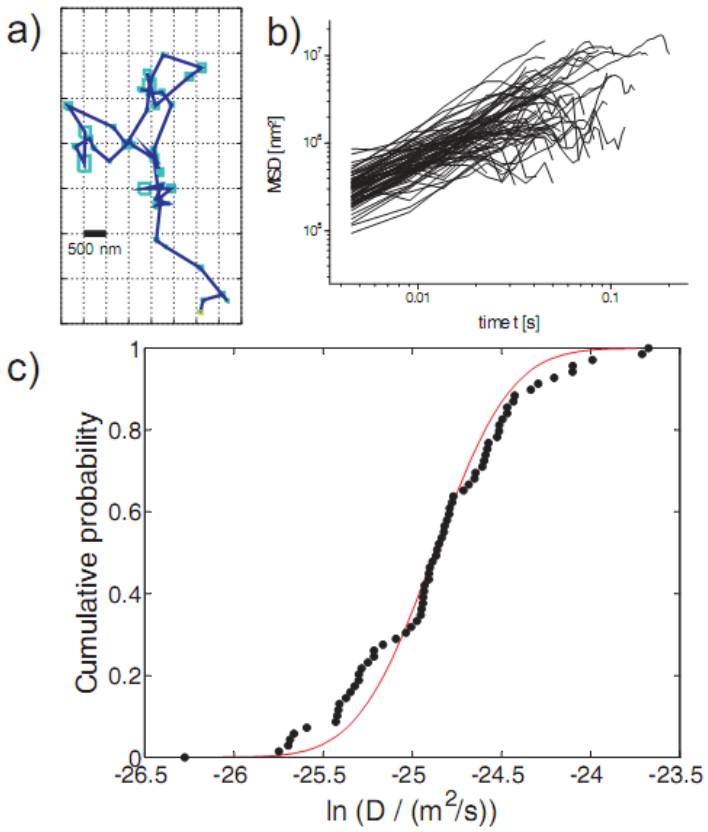

Figure 2: Single-molecule studies of dye molecule diffusion in nanoporous glass. a) Typical trajectory of a single dye molecule diffusing in the porous host system. For each time point the experimentally determined positioning accuracy is depicted by box-error bars. b) MSD plots obtained from the analysis of 70 single molecule trajectories of Atto532 dye molecules. The measurement was performed using a dye concentration of 3.2×10^{-11} mol / l. c) Cumulative distribution of the logarithm of the single molecule diffusivities of the sample with a dye concentration of 3.2×10^{-11} mol / l. The data are fitted assuming a log-normal distribution using a maximum likelihood estimation (red line).

In order to compare the data obtained from PFG NMR und SPT, the mean diffusivities of Atto532 molecules inside the porous host system are shown in Figure 3. The data plotted as

red circles correspond to the mean values of the observed distributions of single-molecule diffusion coefficients. The error bars are computed keeping in mind tracking and statistical errors as well as sample-to-sample variations and the lower signal-to-noise ratio for higher guest molecule concentrations. PFG NMR mean values are shown as black squares. Irrespective of the fact that the measuring conditions may thus be adjusted to allow the application of both techniques to one and the same host-guest system, the maximum guest concentrations in SPT turned out to remain separated from the minimum concentrations in PFG NMR by still one order of magnitude. Even under such conditions, however, the measurements may become fully comparable if molecular diffusion is controlled by host-guest interaction, with the host surface being sufficiently homogeneous for ensuring a host-guest interaction independent of guest concentration.

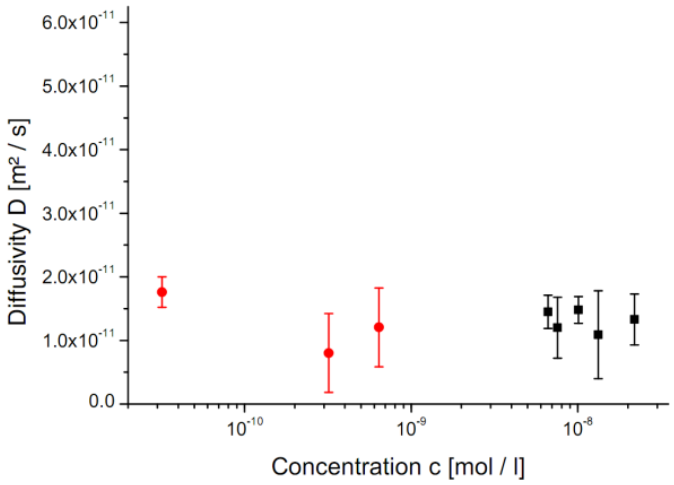

Figure 3: Mean diffusivities of Atto532 molecules inside the porous host system (pore size 3 nm). Single molecule (red circles) and PFG NMR (black squares) mean values.

Since (within the limits of accuracy) both techniques provide the same result (Figure 3), single-molecule and ensemble diffusion measurements are thus found to experimentally confirm the hypothesis of ergodicity for the first time. With these experiments, the two so-far separated worlds of diffusion measurements have been brought together. As a prerequisite of this "marriage" we have considered a situation where the rules of normal diffusion are obeyed. However, single particle observations of e.g. biological systems[23, 24] often seem to contradict ergodicity. In many such studies, the mean square displacement $\langle r^2(t)\rangle$ is found to deviate from the "normal" dependence $\langle r^2(t)\rangle \propto t$,[12-14, 25] with the mean square displacement generally increasing less than linearly with the observation time.

Among the reasons leading to such sub-diffusive dynamics, “macromolecular crowding” and “obstacle effects”[25] are considered as the most probable and decisive ones. Under these conditions ergodicity breaking, i.e. the difference between the messages of SPT and PFG NMR, might occur for example due to aging effects. They are correlated with the broad distribution of the mean residence times of the particles in the system’s sub-volumes and its variation during the evolution of the system. Now, with the combined potentials of single particle and ensemble measurements, we lay out the basis for future studies aiming at the clarification of the possible conditions and underlying reasons for the resulting patterns of ergodicity breaking.

Acknowledgments

This work was funded by FOR 877 “From local constraints to macroscopic transport”, SFB 749 and the Nanosystems Initiative Munich (NIM). We are grateful to Dr. C. Jung for constructive discussions.

Supporting information

Supporting information for this article is available on the WWW under http://www.angewandte.org

A sodium borosilicate initial glass with the composition 70 wt% SiO_2, 23 wt% B_2O_3 and 7 wt% Na_2O was used for the preparation of the nanoporous monoliths. The initial glass in plate geometry was generated by a modified roller-quenching technique.[19] The molten glass was poured onto a cooled steel plate and then rolled out with a cooled steel cylinder. The rolling led to a high surface-area-to-volume ratio of the glass melt. So, a high cooling rate could be realized. This prevented a strong phase separation during the cooling process. Additionally, an optical fine cooling (slow cooling from 670 K to room temperature) was performed to reduce the tensions in the initial glass. This special cooling procedure allowed the control of early state of phase separation and with that the synthesis of porous glass membranes with a defined nanopore structure.[20, 26]

As a result of the optimized cooling procedure, the 3 nm samples could be prepared without an additional thermal treatment. The resulting glass bodies were cut into smaller glass blocks with a diamond circular saw (SAW 15, Logitech). Then, the smaller glass blocks were cut into thin plates with dimensions of 20 mm x 20 mm x 0.3 mm using an annular precision (Annular 55, Logitech) and a diamond band saw (SAW 15, Logitech). Finally, the thin plates were leached with 3N hydrochloric acid at 363 K for 2 h, washed and dried at room temperature.

The texture characteristics of the nanoporous monoliths were estimated using low temperature nitrogen adsorption. The measurements were carried out in an Autosorb-1-MP instrument from Quantachrome. Prior to the sorption measurements, samples were activated in vacuum at 393 K for at least 24 h. Adsorption and desorption isotherms were measured in a relative pressure range (P/P_0) from 0 to 1.0. Surface area was determined from the linear part of the Brunauer-Emmett-Teller (BET) plot in a relative pressure range (P/P_0) between 0.05 and 0.25. A value of 0.162 nm^2 was used for the cross-sectional area per nitrogen molecule. The total pore volume was estimated from the amount of gas adsorbed at the relative pressure $P/P_0 = 0.99$, assuming that pores were subsequently filled with condensed adsorptive in the normal liquid state. For the evaluation of DFT pore size distribution (Density Functional Theory) the Quantachrome software Autosorb 1 with the following DFT kernel was used: N_2 at 77 K on silica (cylindrical pore, NLDFT equilibrium model). The Non-Local Density Functional Theory (NLDFT) method correctly describes the local fluid structure near curved solid walls. Adsorption isotherms in model pores are determined based on the intermolecular potentials of the fluid-fluid and solid-fluid interactions. The Non-Local Density Functional Theory is an improvement of classical density functional theory, so it includes not only local interactions but also intermediate and long-range correlations. For more details see the review of Neimark *et al.*[27] and the references therein. The N_2 sorption isotherm and the DFT pore size distribution of the nanoporous glass monoliths are shown in Figures S-1 and S-2. The nanoporous glass monoliths were found to be characterized by a specific surface area of 238 m^2/g, a total pore volume of 0.15 cm^3/g and a mean pore diameter of 3 nm.

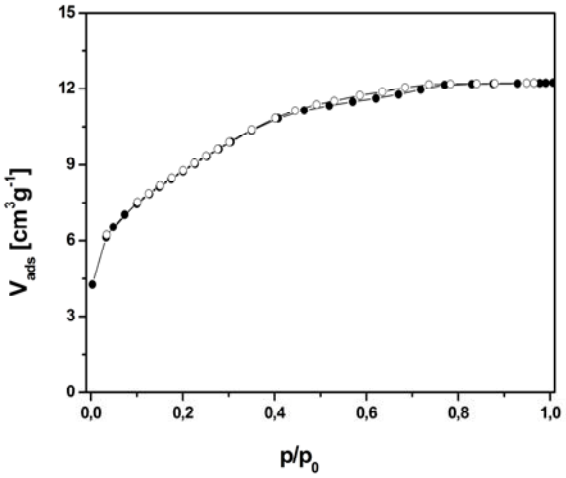

Figure S-1: N_2 sorption isotherm of the nanoporous glass monoliths.

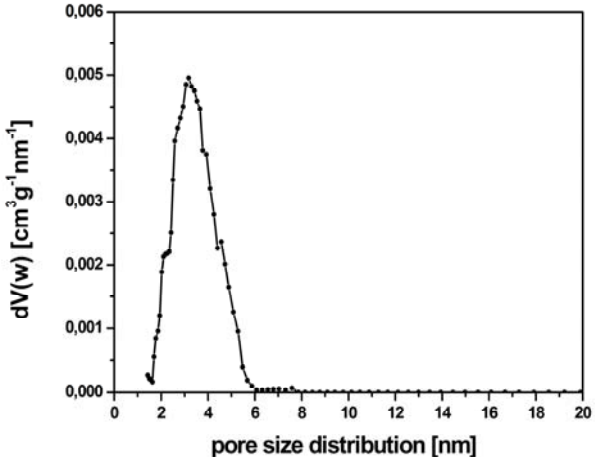

Figure S-2: DFT pore size distribution.

Porous glasses contain more than 96 percent SiO_2. As in the case of other porous silicates, the surface properties of porous glasses are mainly determined by silanol groups with concentrations between 4 and 8 OHs nm^{-2}.[18] So, porous glasses show a homogeneous and well defined surface chemistry. Additional boron species have to be taken into account after a heat treatment at higher temperatures (above 723 K). But in the present study this was not the case.

Methods

Pulsed Field Gradient NMR Diffusometry

PFG NMR diffusion measurements were performed by the stimulated-echo pulse sequence at a proton resonance frequency of 400 MHz. The home-built spectrometer was equipped with a pulsed field gradient system allowing the application of strong magnetic field gradients of up to 35 T/m with extra-short rise and fall times.[28] In this way, as a prerequisite for investigating such bulky and rigid molecules like Atto532, the time intervals relevant for transverse nuclear magnetic relaxation could be kept short enough (typically 1 ms), allowing simultaneously a notable signal attenuation due to diffusion.[10]

The NMR samples were produced by introducing a separately prepared solution of Atto532 in CD_3OD into the previously outgassed host material. The solution was provided in excess so that the PFG NMR signal attenuation becomes a superposition of the contributions outside and inside the host material, with the diffusivity in the pore space determined by the slope of the second, more slowly decaying part in the attenuation curve in Figure 1.[10]

Single Molecule Spectroscopy (SMS) and Single Particle Tracking (SPT)

Fluorescence images were acquired with a wide-field setup as described previously.[16] The Atto532 dye molecules (ATTO532-COOH, ATTO-TEC, Siegen, Germany, see structure in Figure S-3) were excited at 532 nm with a diode pumped solid-state laser (Cobolt Samba TM Laser) with an intensity of 2.5 kW cm^{-2}. Incident laser light was blocked by a dichroic mirror (dual line beamsplitter 532/633, AHF Analysentechnik) and by a band-pass filter (675/250, AHF Analysentechnik).

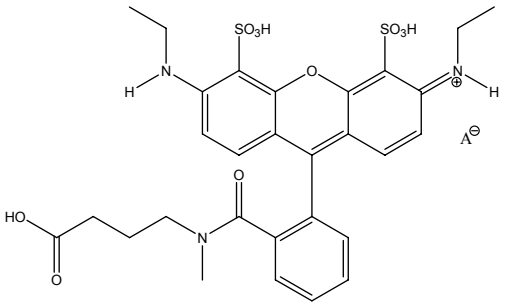

Figure S-3: Chemical structure of Atto532-COOH.

To detect the pathways of the single molecules inside the porous system, series of 1000 frames were recorded with a temporal resolution of ≥ 4 ms per frame. Movie 1 (15 ms / frame, see supporting online material) shows a typical series of fluorescence images. The single dye molecules appear as bright spots on a dark background. SPT was employed to obtain trajectories by fitting frame by frame theoretical diffraction patterns to the spots.[16] With this method the positions of the fluorophores can be obtained with an accuracy of ≥ 10 nm depending on the signal-to-noise ratio.

References

1. F. Crick, DIFFUSION IN EMBRYOGENESIS. *Nature* **225**, 420 (1970).
2. E. R. Weeks, J. C. Crocker, A. C. Levitt, A. Schofield, D. A. Weitz, Three-dimensional direct imaging of structural relaxation near the colloidal glass transition. *Science* **287**, 627 (2000).
3. L. A. Hayden, E. B. Watson, A diffusion mechanism for core-mantle interaction. *Nature* **450**, 709 (2007).
4. S. Kondo, T. Miura, Reaction-Diffusion Model as a Framework for Understanding Biological Pattern Formation. *Science* **329**, 1616 (2010).
5. G. D. Birkhoff, Proof of the ergodic theorem. *Proceedings of the National Academy of Sciences of the United States of America* **17**, 656 (1931).
6. T. Schmidt, G. J. Schutz, W. Baumgartner, H. J. Gruber, H. Schindler, Imaging of single molecule diffusion. *Proceedings of the National Academy of Sciences of the United States of America* **93**, 2926 (1996).
7. G. Seisenberger *et al.*, Real-time single-molecule imaging of the infection pathway of an adeno-associated virus. *Science* **294**, 1929 (2001).
8. A. Zürner, J. Kirstein, M. Doblinger, C. Bräuchle, T. Bein, Visualizing single-molecule diffusion in mesoporous materials. *Nature* **450**, 705 (2007).
9. P. T. Callaghan, *Principles of Nuclear Magnetic Resonance Microscopy*. (Clarendon Press, Oxford, 1991).
10. W. S. Price, *NMR Studies of Translational Motion*. (University Press, Cambridge, 2009).
11. J. Philibert, in *Leipzig, Einstein, Diffusion*. J. Kärger, Ed. (Leipziger Universitätsverlag, Leipzig, 2010), pp. 41.
12. A. Lubelski, I. M. Sokolov, J. Klafter, Nonergodicity mimics inhomogeneity in single particle tracking. *Physical Review Letters* **100**, 250602 (2008).
13. Y. He, S. Burov, R. Metzler, E. Barkai, Random time-scale invariant diffusion and transport coefficients. *Physical Review Letters* **101**, 058101 (2008).
14. J. Szymanski, M. Weiss, Elucidating the Origin of Anomalous Diffusion in Crowded Fluids. *Physical Review Letters* **103**, 038102 (2009).
15. J. P. Bouchaud, WEAK ERGODICITY BREAKING AND AGING IN DISORDERED-SYSTEMS. *Journal De Physique I* **2**, 1705 (1992).

16. J. Kirstein *et al.*, Exploration of nanostructured channel systems with single-molecule probes. *Nature Materials* **6**, 303 (2007).
17. R. Valiullin *et al.*, Exploration of molecular dynamics during transient sorption of fluids in mesoporous materials. *Nature* **443**, 965 (2006).
18. F. Janowski, D. Enke, in *Handbook of Porous Solids*. F. Schüth, K. S. W. Sing, J. Weitkamp, Eds. (Wiley-VCH Verlag GmbH, Weinheim, 2008), pp. 1432.
19. T. Yazawa, R. Kuraoka, W. F. Du, Effect of cooling rate on pore distribution in quenched sodium borosilicate classes. *Journal of Physical Chemistry B* **103**, 9841 (1999).
20. D. Enke *et al.*, in *Characterization of Porous Solids VI*. F. Rodriguez Reinoso, B. McEnaney, J. Rouquerol, K. Unger, Eds. (Elsevier Science Bv, Amsterdam, 2002), vol. 144, pp. 347.
21. C. Chmelik *et al.*, Nanoporous Glass as a Model System for a Consistency Check of the Different Techniques of Diffusion Measurement. *A European Journal of Chemical Physics and Physical Chemistry* **12**, 1130 (2011).
22. J. Kärger, H. Pfeifer, W. Heink, Principles and Application of Self-Diffusion Measurements by Nuclear Magnetic Resonance. *Advances in Magnetic Resonance* **12**, 2 (1988).
23. M. J. Saxton, K. Jacobson, Single-particle tracking: Applications to membrane dynamics. *Annual Review of Biophysics and Biomolecular Structure* **26**, 373 (1997).
24. I. Golding, E. C. Cox, Physical Nature of Bacterial Cytoplasm. *Physical Review Letters* **96**, 098102 (2006).
25. K. de Bruin *et al.*, Cellular dynamics of EGF receptor-targeted synthetic viruses. *Molecular Therapy* **15**, 1297 (2007).
26. D. Enke, F. Janowski, W. Schwieger, Porous glasses in the 21st century - a short review. *Microporous and Mesoporous Materials* **60**, 19 (2003).
27. P. I. Ravikovitch, A. Vishnyakov, A. V. Neimark, Density functional theories and molecular simulations of adsorption and phase transitions in nanopores. *Physical Review E* **64**, 011602 (2001).
28. P. Galvosas *et al.*, Generation and application of ultra-high-intensity magnetic field gradient pulses for NMR spectroscopy. *Journal of Magnetic Resonance* **151**, 260 (2001).

4 Single molecule diffusion in mesoporous silica channels

4.1 Direct visualization of dye and oligonucleotide diffusion in silica filaments with collinear mesopores

F. Feil*, V. Cauda*, T. Bein, C. Bräuchle, Direct Visualization of Dye and Oligonucleotide Diffusion in Silica Filaments with Collinear Mesopores. *Nano Letters* **12**, 1354 (2012).

[*] These authors contributed equally to this work.

Author contributions

F.F. applied the gold layers by thermal evaporation, conceived and performed the single molecule experiments and analyzed the single molecule data. V.C. synthesized and characterized the mesoporous silica filaments by SAXS, TEM, sorption measurements, IR and AFM.

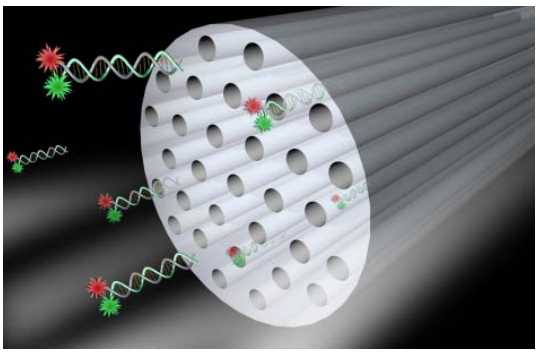

The diffusion dynamics of terrylene diimide (TDI) dye molecules and dye-labeled double-strand DNA were studied in micrometer long silica filaments containing collinear, oriented mesopores using single molecule fluorescence microscopy. TDI was used as a stable and hydrophobic probe molecule for single molecule structural analysis. We used template-free mesoporous silica filaments with 4 nm pore diameter and chemical functionalization with one or two types of trialkoxysilane groups to enhance the affinity between the host system and the guest molecules. Insights about the mesoporous structure as well as the translational and orientational diffusion dynamics of the guest molecules observed along micrometer long trajectories could be obtained. Additionally, the stability of DNA oligomers (15 base pairs, bp, about 5.3 nm long) within the mesopores was examined, showing no degradation of the oligonucleotide upon incorporation into the mesopores. Diffusion of both guest molecules could be controlled by exposure to vapors of water or chloroform; the latter both induced a reversible on-off control of the translational movement of the molecules.

Ordered mesoporous silica structures have recently advanced to an important class of self-assembled nano-structured materials on account of their variety of structures and pore geometries, controllable pore sizes and their widely tunable properties, for example by pore functionalization.[1-3] These materials can be exploited as a host system for a large range of potential guest molecules including inorganic, organic as well as biological molecules. Mesoporous materials are of interest for numerous potential applications,[4] including molecular separation,[5-7] sensor systems,[8, 9] catalysis,[10, 11] photovoltaic solar cells,[12, 13] and drug delivery devices for nano-medicine.[14-16] The ability to specifically design such materials and improve their properties with respect to a particular functionality is therefore strongly desired. Some of these applications, such as chromatography[17, 18] and templating of nano-wires[19, 20] could benefit from highly structured and extended one-dimensional (1D) mesoporous channels. Substantial efforts have recently been aimed at creating mesoporous materials with oriented channel systems and with high aspect ratios (length to diameter). The techniques used for these syntheses include external electric[21] and magnetic fields,[22] shear flow control,[23] substrate surface modification[24] and microtrenches.[25] However, these methods often require specialized equipment or are restricted to certain substrates or surfactants. One successful approach to control the mesoporous domain size and orientation, and towards obtaining 1D hexagonal mesoporous structures, is the confined synthesis of mesoporous silica inside anodic porous alumina membranes[26, 27] via the EISA process (Evaporation-Induced Self-Assembly).[28]

In most cases it is difficult or impossible to load bulky guest molecules into template-filled mesopores. Moreover, these template-filled mesoporous channels provide a hydrophobic environment for guest molecules, as well as basic or acidic pH depending on the synthesis conditions. It is therefore advantageous to remove the template in order to incorporate polar or pH-sensitive molecules and in particular bio-molecules, such as proteins or DNA. Additionally, the modification of the pore walls with appropriate chemical functional groups is essential to provide a suitable host environment for the desired guest molecules.[29]
In order to develop such customized host-guest systems for nanotechnology applications, a thorough knowledge of the interactions between the host and the guest molecules is required. Usually, the investigation of porous host systems and of the guest molecules diffusing inside the channel systems is accomplished by determining an average host

structure and/or by averaging over a large number (ensemble) of guest molecules. Such methods include NMR,[30, 31] IR and UV-Vis spectroscopy[32] and X-ray diffraction.[33] Recently, single molecule (SM) experiments, in which the motion of a single particle is directly observed over time, provided a completely new view on diffusion. The presence of subpopulations, rare events and the influence of heterogeneities of the structural environment on the diffusing molecules can be revealed in unprecedented detail.

Here, we use single molecule spectroscopy to investigate the translational and orientational dynamics of terrylene diimide (TDI)[34] dye molecules and dye-functionalized double-strand DNA constructs incorporated in micrometer long and columnar channels of mesoporous silica filaments. The DNA constructs were labeled with Cy3 and Cy5 Förster Resonance Energy Transfer (FRET) dye pairs to test their stability in the mesopores. Template-free and chemically functionalized mesoporous silica filaments were used. In particular, a double-functionalization with cyanide and amino groups was used to provide an appropriate polar environment within the mesoporous channels for the incorporation of DNA. The mesoporous filaments were synthesized by the EISA method in porous Anodic Alumina Membranes (AAMs), providing columnar, oriented pores of 4 nm in diameter. An initial co-condensation step was included to introduce an homogeneous chemical functionalization with nitrile groups (10 mol% with respect to the silica source). The template was then removed by Soxhlet extraction. Our approach is aimed at avoiding the direct contact of the fragile oligonucleotides with the acidic medium from the synthesis conditions inside the template-filled mesopores, which would otherwise induce DNA protonation, hydrolysis and degradation. In addition, amino groups were also grafted to the channel walls to favor the uptake of the negatively charged DNA constructs, thus allowing the formation of hydrogen bonding during the loading process. For further details, see the Supporting Information (S.I.).

The CN-functionalized and CN+NH_2 bi-functionalized mesoporous silica (MS) materials (sample names hereafter CN-MS and CN+NH_2-MS, respectively) were characterized prior to alumina dissolution. Clear evidence of the mesoporosity of the structure is given by Small-Angle X-ray Scattering (SAXS) in Figures 1a and b. Here the columnar alignment of the mesopores is indicated by the presence of the two in-plane diffraction spots, indexed as (01) and (0-1). The data also show that the bi-functionalized mesoporous channels retained the

same structure as the mono-functionalized samples. Nitrogen sorption measurements (Figure S-1 in the S.I.) confirm these findings and provide the pore diameters, which are about 4.2 and 3.8 nm for the CN-MS and CN+NH_2-MS samples, respectively.

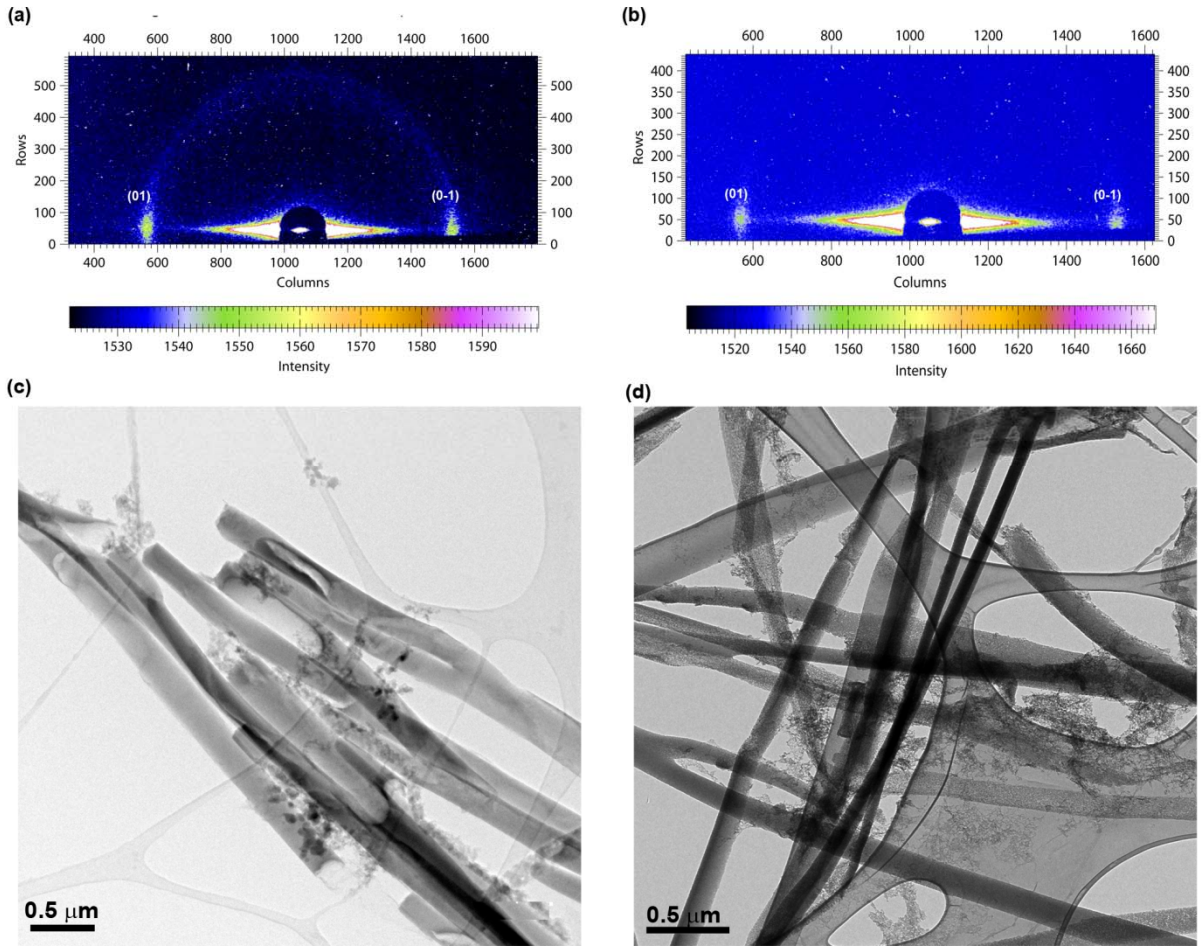

Figure 1: Small Angle XRD Scattering (SAXS) of (a) CN-functionalized mesoporous silica and (b) CN+NH_2-bi-functionalized silica inside the alumina template. Transmission electron micrographs of (c) extracted CN-functionalized and (d) extracted CN+NH_2-bi-functionalized mesoporous filaments after alumina template dissolution

Finally, the mono- and bi-functionalized filament bundles were extracted from the AAM in a phosphoric acid solution (5 %w). The shape of the mesoporous filaments is visualized by transmission electron microscopy (TEM) in Figures 1c and d and by atomic force microscopy (AFM, Figure S-3 in the S.I.). The CN-MS and CN+NH_2-MS samples were loaded afterwards with the desired guest molecules at a concentration appropriate for single molecule studies (about 10^{-11} M, see S. I. for details) and deposited on a glass substrate.

The diffusional dynamics of single TDI dye molecules incorporated in the mesoporous channels of the filament samples were studied by single molecule fluorescence wide-field microscopy.[35] Series of typically 1000 fluorescence images were recorded with a temporal resolution of ≥ 100 ms per frame (see movies supporting online material). An example of a single molecule fluorescence image is depicted in Figure 2a. The single TDI dye molecules appear as bright spots on a dark background. Here, the filament can easily be spotted due to the large number of single molecules arranged linearly in the image. Additionally, several single molecules are distributed randomly on the glass substrate. Under air atmosphere the TDI molecules remain immobile in the mesopores, while exposure of the sample to a saturated mixture of $CHCl_3$ and H_2O vapors enables diffusion. In that case TDI molecules moving along the filaments can be observed (S-Movie 1). This switching between diffusion and the immobile state is reversible and can be controlled by addition or removal of the $CHCl_3$ and H_2O vapors. Additionally the diffusion coefficient can be tuned to a desired value by adjusting the vapor pressure of the $CHCl_3$ and H_2O vapors (data not shown; see references[36, 37] for similar experiments).

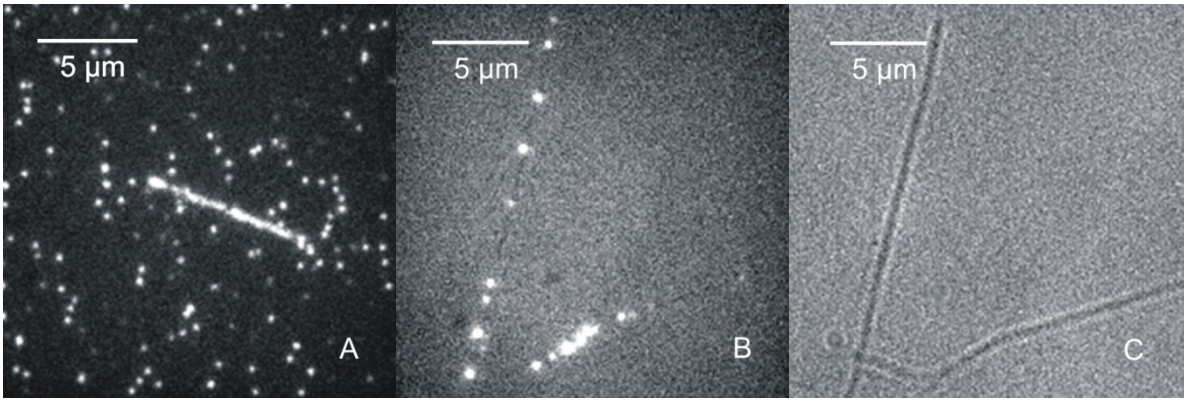

Figure 2: Single molecule fluorescence experiments. a) Fluorescence image of a sample without a gold layer. Every bright spot represents one single molecule. The mesoporous filament is clearly visible due to the incorporated dye molecules. Additionally, molecules located on the cover glass also show fluorescence. b) Fluorescence image of a sample with a gold layer. Here, only molecules residing in the mesoporous channels are still fluorescing, while all others are quenched. The positions of the bright spots are perfectly correlated to the structure of the filaments displayed in c): Optical transmission image of the filaments shown in b).

In order to investigate whether the observed diffusion of single TDI molecules along the mesoporous filaments occurs in the mesoporous channels of the host material or only on the surface, we deposited a 0.4 nm thin layer of gold on the surface of the sample by thermal evaporation. The thickness of the film was determined by employing a crystal oscillator. Because of the close vicinity to the small gold particles, the fluorescence of all molecules on the surface of the glass substrate or the filaments is quenched.[3] Only TDI molecules residing inside the mesoporous host remain fluorescent (Figure 2b). Their positions are clearly correlated to the structure of the filaments depicted in the transmission optical image in Figure 2c. The diffusion, only occurring while exposed to $CHCl_3$ and H_2O vapors, appears highly structured due to the confinement of the molecules in the columnar mesopores (S-Movies 2 and 3).

Single particle tracking (SPT) was used to obtain trajectories (Figures 3a and 3b) by fitting, frame-by-frame, theoretical diffraction patterns to the fluorescence spots.[35] With this method the positions of the fluorophores can be determined with a positioning accuracy of ≥ 5 nm depending on the signal-to-noise ratio (Figure 3c). Changes in the brightness of the molecule, background fluorescence or other dye molecules nearby can decrease the signal-to-noise ratio and thereby the positioning accuracy. The trajectory of a single molecule provides detailed information about the host structure, such as domain size and the presence of defects (Figure 3b). These defects include dead ends, where the pores are impassable for molecules (Figure 3b) or small openings in the silica walls through which the dye molecules can enter a neighboring channel as observed in high resolution experiments.[38] The presented trajectories have a highly defined nearly linear shape extending over several microns (up to about 10 µm), reflecting the collinear structure of the mesoporous channels (shown by TEM analysis in Figure 1 and in previous studies).[20]

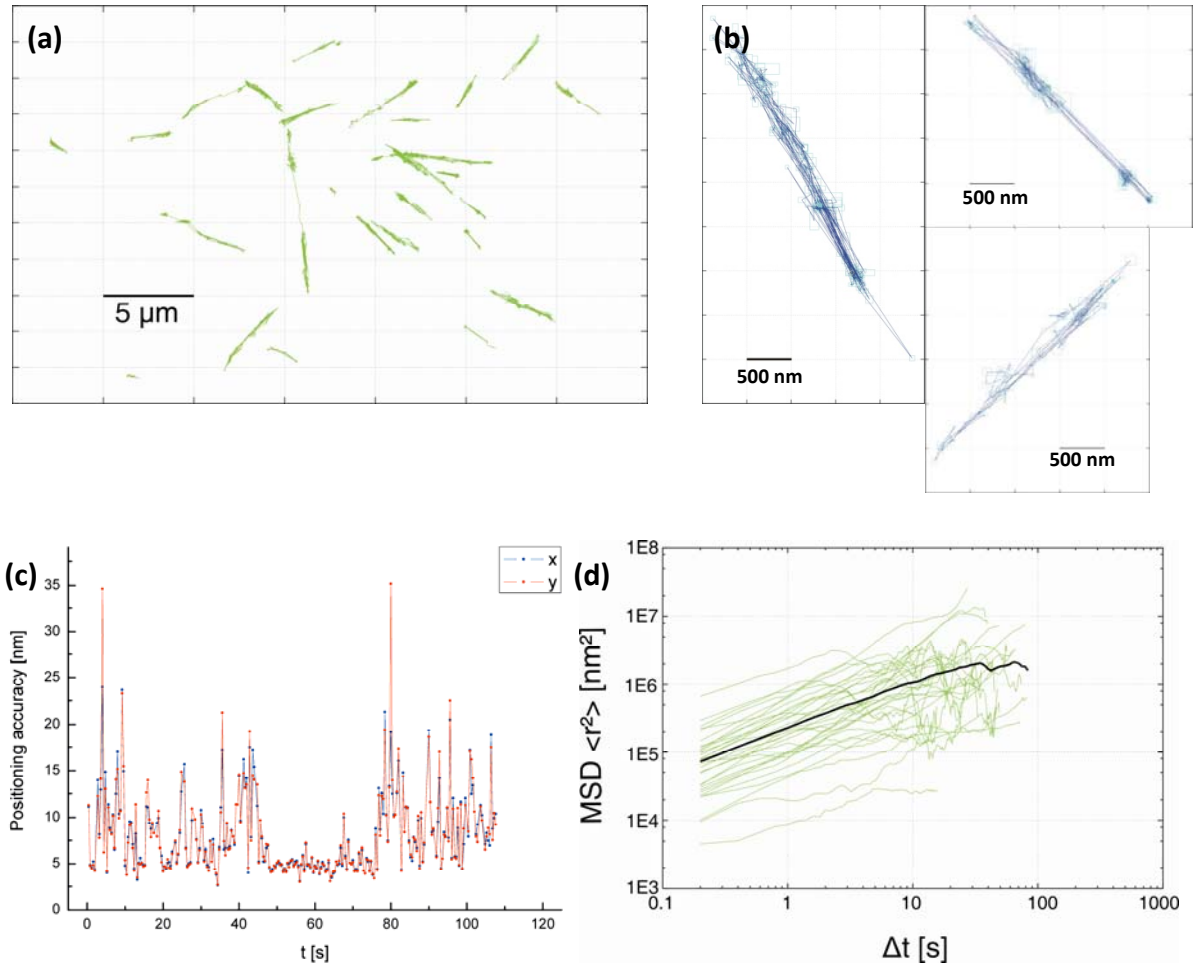

Figure 3: Diffusion analysis of single TDI dye molecules in the mesoporous host system. a) Overview of several single molecule trajectories. They have a very linear shape, consistent with the columnar structure of the mesoporous channels. b) Three examples of single TDI molecule trajectories. The experimentally determined accuracy for each observed position of a molecule is given by box-error bars. c) Positioning accuracy of one single molecule time-trace with a minimum of down to 5 nm. Changes in the brightness of the molecule, background fluorescence or another dye molecule nearby decrease the signal-to-noise ratio and thereby the positioning accuracy. d) Mean square displacements of several single TDI molecules (green). The average value is shown in black.

A statistical analysis based on the mean-square displacements (MSD)[35] was carried out for about 70 single TDI molecule trajectories. The MSD of every single molecule is displayed versus time in Figure 3d (green) and the average MSD plot of all trajectories is presented in black. In similar mesoporous materials with smaller domain sizes, such as thin films, the MSD plots of the single TDI dye molecules are linear for short time intervals and bend towards a

horizontal asymptote for large time intervals. This is typical for confined diffusion and provides an estimate of the respective domain sizes.[35, 39] In contrast, the MSD plots of the single TDI molecules diffusing in the silica filaments with oriented mesopores stay linear over the entire observed time range. Therefore, the average accessible channel length (domain size) in the new mesoporous filament host system presented here has to be much larger than in previously published mesoporous systems.[35, 39] This confirms that the synthesis method of the mesoporous silica structures inside a porous alumina membrane presented in this work generates not only highly structured, but also much longer one-dimensional mesoporous channels than in previous approaches.

The broad distribution of the single molecule MSD plots arises from structural heterogeneities at the nanometer scale of the surrounding host material. With ensemble methods, the influence of this structurally heterogeneous host environment on the diffusion of identical molecules is hidden due to averaging.

The diffusion coefficient of each single molecule can be extracted from the linear part of the MSD plots according to the Einstein-Smoluchowski relation $MSD = 2\,Dt$ assuming a one-dimensional isotropic Brownian diffusion for the step sizes much smaller than the confinement region. The obtained single molecule diffusivities show a broad distribution with a mean value of $\langle D \rangle = 1.1 \times 10^5$ nm²/s for saturated $CHCl_3$ and H_2O vapor pressure at room temperature. As previously mentioned for the MSDs, the distribution of diffusion coefficients is likewise induced by structural heterogeneities of the host environment for each single molecule.

In addition to the single molecule wide-field experiments, the samples were studied with a scanning confocal microscope with home-built rotating λ/2-plate (see S.I.) in order to perform single molecule orientation measurements. As shown in previous studies, even the orientation of guest molecules incorporated in a mesoporous host system can be controlled. One way to accomplish this is to decrease the pore diameter for rod-shaped guest molecules, such as TDI, to smaller values than the longitudinal axis of the molecule.[38] This can be achieved by using short surfactant molecules, such as cetyltrimethylammonium bromide (CTAB), for pore templating in the synthesis process. Another possibility is to utilize specific pore geometries and host-guest interactions.[35, 39] Here we used CTAB as surfactant

template to achieve small pore diameters and nitrile-propyl groups (-CN) as chemical functionalization. Although the template was removed after the synthesis by solvent extraction, the available average pore diameter of about 4 nm (as measured by nitrogen sorption isotherms) was not sufficient to allow the free rotation of the dye molecules (Figure 4a). A high concentration of TDI dye molecules was incorporated into the mesoporous channels of that sample. Therefore, no single molecule fluorescence signals appear, but instead a bright area is observed. By rotating the λ/2-plate, it can be shown by the striped fluorescence pattern that the dye molecules maintain a stable orientation. We fitted the phase of the fluorescence intensity with respect to the reference beam to obtain the orientation of the transition dipole moments of the TDI dye molecules (see S.I.), which are indicated in yellow. As the transition dipole moment of TDI is oriented along the long axis of the molecule, the dye molecules are oriented parallel to the mesoporous channels of the filaments.

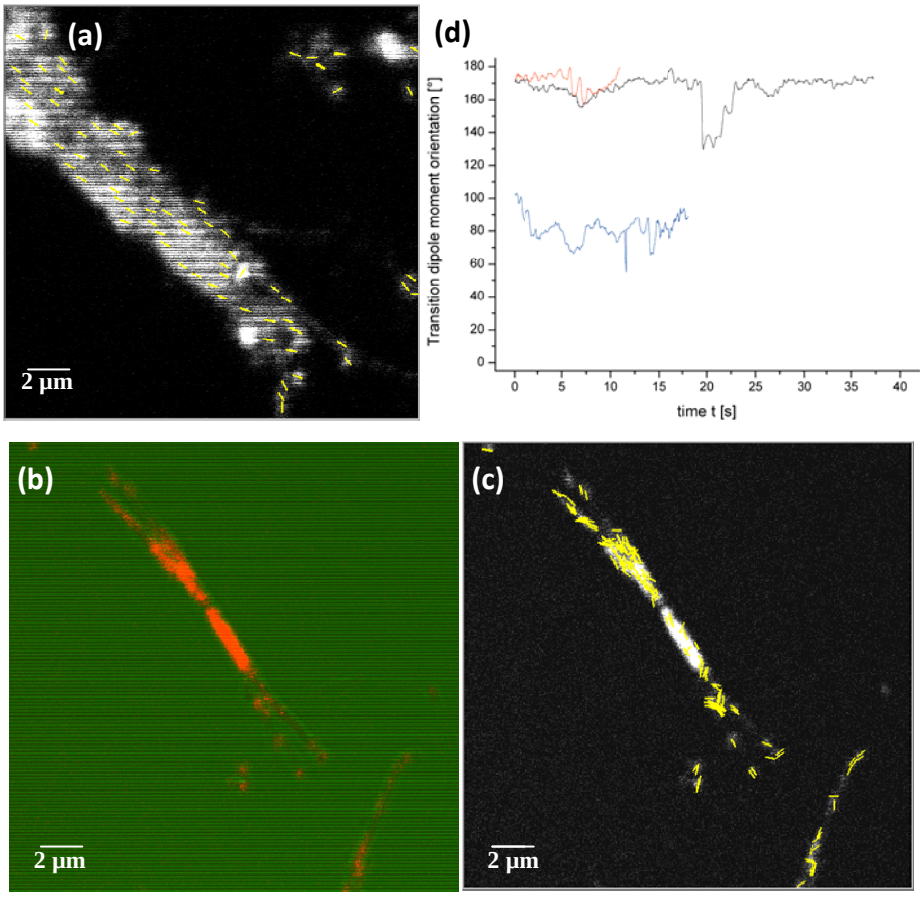

Figure 4: Confocal microscopy for the analysis of molecular orientation. (a) The filaments were loaded with an ensemble concentration of TDI molecules (from a 10^{-8} M solution). The bright fluorescence signal of the molecules within an agglomeration of many parallel

filaments can be observed as a striped pattern. Due to the rotating λ/2-plate this implies a strong orientation of the molecules, which was obtained through fitting, displayed by the yellow bars. (b) A filament sample loaded with a single molecule concentration of TDI molecules. Overlay of the fluorescence (red) and transmission (green) image. (c) Fluorescence image with the fit of the single molecule orientations (yellow bars) of Figure 4b. (d) Plots of the orientation of the transition dipole moment of three single TDI dye molecules in the channels of the mesoporous filaments. As shown, the orientation of the molecules remains nearly constant, but still the molecules can rotate to a small degree.

In addition to the orientation studies of an ensemble of molecules, single molecule orientation measurements were also performed with the described confocal setup. In Figure 4b an overlay of two detection channels is depicted: The transmission signal of the reference beam (green) and the fluorescence image (red). The transition dipole moment of the single TDI molecules was fitted using an orientation analysis similar to that of the molecular ensemble. The dipole moments are displayed as yellow bars, which represent the molecular orientation (Figure 4c). Most of the single molecules exhibit an orientation parallel to the filaments and consequently along the mesopores. In contrast to the ensemble measurements, the single molecule studies are once more able to reveal heterogeneities of the host structure, showing a distribution of orientations along the main direction parallel to the channel orientation. In Figure 4d the angles of the transition dipole moment orientation of three single TDI dye molecules inside the mesoporous structure are plotted versus time. The orientation of the molecules remains nearly constant over time, but still the molecules can rotate to a small degree.

As shown above, TDI dye molecules can be used to explore the channel system of the mesoporous host structure. However, the template-extracted and functionalized mesopores are also ideally suited to incorporate polar or charged guest molecules. In particular, bio-molecules that are easily denatured by elevated temperature or pH-changes, such as enzymes, proteins or DNA, can be stabilized upon confinement in this specifically adapted host matrix.[40, 41] Here we show the incorporation of double-stranded (ds)-DNA, which was labeled with a Cy3 dye on one strand and with a Cy5 dye on the other. The dye pair is located on the same end of the double strand and exhibits Förster Resonance Energy

Transfer (FRET). Upon excitation of the Cy3 dye, energy transfer will take place from the green Cy3 (donor) to the red Cy5 (acceptor) dye and fluorescence of the red dye can be monitored. FRET is strongly distance-dependent, and the effect can be used to determine molecular distances between 2 – 10 nm. In the case of DNA denaturation, the two single strands will be separated and no FRET signal is expected. The sample depicted in Figure 5 shows mesoporous filaments loaded with the Cy3-Cy5 labeled ds-DNA. It was coated with a thin layer of gold in order to quench the fluorescence of all dye molecules residing on the surface of the sample, as described for the TDI studies. Therefore, all fluorescence signals originate from dyes inside the mesopores. After excitation at 532 nm, the Cy3 fluorescence can be observed in the green channel (right) and emission of fluorescing Cy5 molecules upon FRET in the red channel (left). This demonstrates that the ds-DNA strands are still intact after loading into the mesoporous channels.

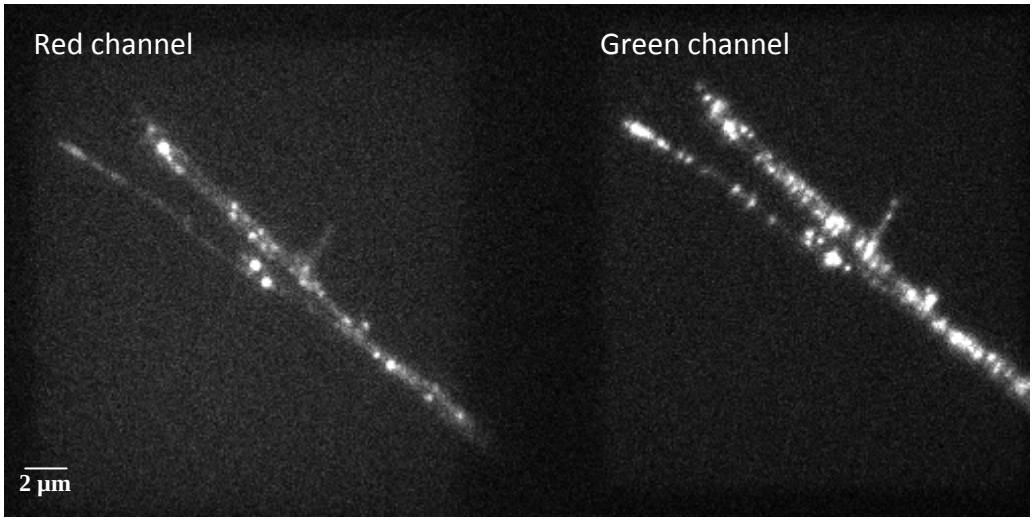

Figure 5: Single molecule FRET experiment with Cy3-Cy5 labeled ds-DNA strands in the mesoporous structure. Fluorescence images (excitation at 532 nm) of a sample with a deposited gold layer are shown. Only molecules residing in the mesoporous channels are fluorescing, while all others are quenched. Left: Red channel showing the red emission of fluorescing Cy5 molecules after FRET. This means that the ds-DNA strands are still intact. Right: Green channel showing Cy3 fluorescence.

Loading large molecules such as DNA into comparatively small-sized pores is difficult. DNA is usually described by a worm-like chain model with a persistence length of about 50 nm.[42] This implies that the ds-DNA studied here (about 5.3 nm long) will behave like a rigid rod and

that it must lose some translational and rotational entropy upon transferring it into a long but narrow columnar pore. As a result of several optimizations, we developed the combination of nitrile and amino groups to functionalize the mesopores for successful loading with the DNA molecules. Even with this favorable functionalization, the adsorption of DNA from solution into the mesopores is very slow, lasting about one week (see S.I.). In the absence of the above functional groups, i.e. with unfunctionalized or only mono-functionalized (CN-MS) filaments, no loading of DNA can be observed within this time frame. Similar to the behavior of the TDI dye, it is possible to control the diffusivity of the ds-DNA in the mesopores by changing the humidity: high humidity leads to visible diffusion, while low humidity turns off the motion of the DNA (for DNA diffusion see S-Movie 4).

In analogy to the analysis of the single TDI dye molecule diffusion, we determined the single molecule trajectories of the ds-DNA constructs (Figure 6). The obtained trajectories are highly structured and quite linear over up to 7 µm. The linear extension of these trajectories appears to be even greater than for the trajectories of the single TDI molecules. We attribute this behavior to the much greater length of the DNA double strands, which is very likely to prevent switching between neighboring channels through small defects in the silica pore walls as described for TDI. The long trajectories also prove that both the template extraction and the post-synthesis grafting with amino-propyl groups did not damage the structure of the mesopores at the nanoscale. This confirms similar results for the bulk material obtained with ensemble methods (see S.I.).

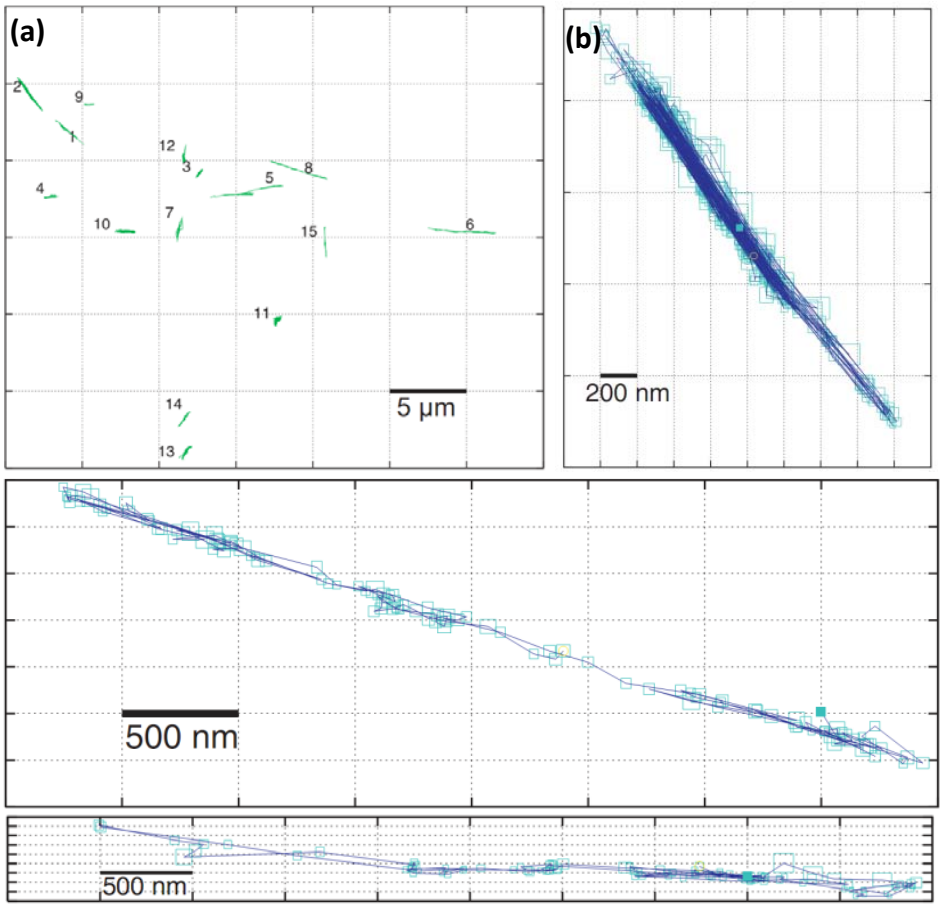

Figure 6: Single molecule trajectories of ds-DNA strands inside the mesoporous host system CN+NH_2-MS. a) Overview of several trajectories, which exhibit a linear shape due to the columnar structure of the mesoporous channels. b) Three examples of single DNA molecule trajectories. The experimentally determined positioning accuracy for each observed position of a molecule is given by box-error bars.

The single DNA molecule trajectories were further analyzed with respect to their MSDs. The single molecule MSDs (green) and the average value (black) are plotted versus time in Figure 7a. Unlike the single TDI molecule MSD plots presented earlier, the DNA MSD plots obviously bend after shorter time intervals. Hence, it is reasonable to assume that the larger and rather stiff DNA double strands are more sensitive to confinement effects in the pore system than the much smaller TDI molecules. The comparison between the average MSD plots of the two different guest molecules is depicted in Figure 7b. The difference in the shape of the MSDs is clearly visible. Additionally, the average MSD of the TDI dye molecules is only about two times larger than the one of the ds-DNA molecules. However, the diffusional behavior of a guest molecule inside a porous host system is dependent on several host-guest

interactions. This includes size and shape of the host pores and guest molecules as well as their chemical and physical properties, i.e. chemical functionalization of the pore walls or polarity (or even a charge) of the guest molecules. Therefore, it is difficult to predict the relative diffusional behavior of different guest molecules. These results show that while the larger DNA molecules take much longer time to be loaded into the mesoporous channels compared to the smaller TDI molecules as stated before, they move nearly as fast once they are inside the mesopores. The single molecule diffusion coefficients of the DNA molecules which were extracted from their MSD plots provide a calculated mean value of <D> = 5.9 x 10^4 nm²/s for saturated H_2O vapor pressure at room temperature.

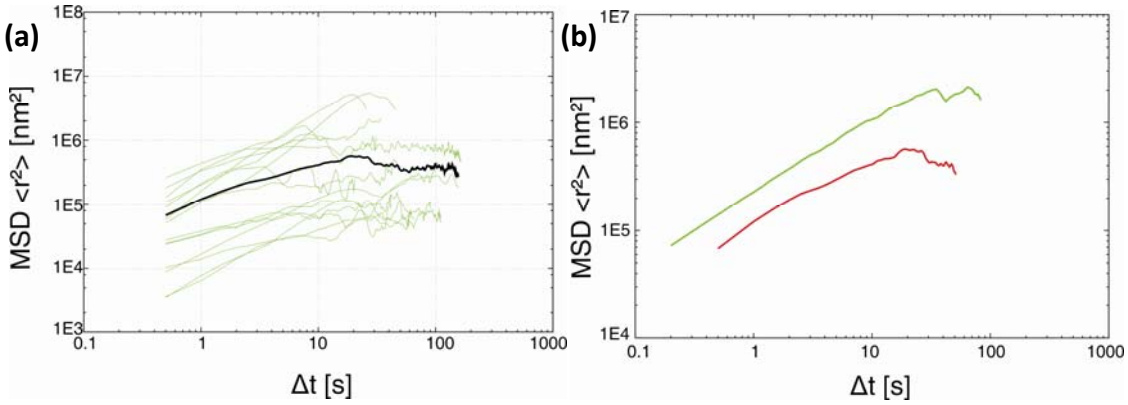

Figure 7: Single molecule diffusion analysis of ds-DNA molecules in mesoporous filaments. (a) Mean square displacement plots of several single molecules (green). The average value is shown in black. (b) Comparison of the average MSD plots of TDI (green) and ds-DNA (red) molecules in the mesoporous structure of the filaments. The MSDs of the DNA molecules are about two times lower than the MSDs of TDI. Furthermore, the difference in size of the observed guest molecule is reflected by the shape of their MSDs. While the mean MSD plot of the small TDI molecules is nearly linear (which suggests normal diffusion) over the observed time range, the mean MSD plot of the ds-DNA molecules bends for longer time intervals (due to the confined diffusion in the mesopores). This indicates that the larger DNA molecules respond more strongly to the confinement in the filaments than the TDI molecules.

In conclusion, template-free and either mono- or bi-functionalized mesoporous filaments with collinear ordered mesopores, synthesized in and then extracted from a porous alumina membrane, constitute very versatile host systems for single molecule diffusion studies under

spatial confinement. These systems contain highly structured pores that are several microns long; they are suitable for accommodating hydrophobic TDI as well as large dye-labeled ds-DNA guest molecules. The deposition of a thin layer of gold on the samples quenches the fluorescence of the dye molecules residing on the external surface of the filaments, while molecules incorporated in the mesoporous channels remain fluorescent, thus clearly demonstrating successful loading of the guest molecules. Additionally, we show that the incorporation of ds-DNA into such a host system does not damage its integrity; the intact DNA exhibits remarkably long linear trajectories in the mesoporous channels. The diffusion of both types of guest molecules could be controlled by a reversible on-off mechanism. Hereby, the exposure of the sample to water and chloroform vapors for TDI or only water vapor for DNA enabled the diffusion of both guest molecules. The single molecule experiments provide insights into the translational as well as the orientational dynamics of the guest molecules. Moreover, structural information from the viewpoint of the single guest molecules, such as domain sizes, accessible pore space, the presence of defects, interconnections and dead ends in the mesoporous host material could be obtained by direct visualization in real space. The highly structured collinear mesoporous hosts investigated here could serve as a platform for the further development of customized nanosystems for applications in bioanalytics.

Acknowledgments

Support from DFG-SFB 749, from the NIM and CIPSM Excellence Clusters (LMU Munich) and from CeNS is gratefully acknowledged. The authors also thank T. Reuther for nitrogen sorption measurements, Dr. S. Schmidt for transmission electron microscopy images, P. Altpeter for help with the deposition of the thin gold layer by thermal evaporation and F. Canepa for ToC graphics design. We are grateful to Prof. K. Müllen for providing the TDI dye.

Supporting information

Detailed synthesis procedure and incorporation of guest molecules into the mesoporous filaments, additional characterization methods of the functionalized mesoporous silica

materials, movies of diffusing fluorescent molecules. This material is available free of charge via the Internet at http://pubs.acs.org.

Synthesis of functionalized mesoporous silica rods

Mesoporous silica (MS) filaments were synthesized by hard-templating through the EISA (Evaporation-Induced Self-Assembly) process in porous Anodic Alumina Membranes (AAMs) in a two-step functionalization process. The AAMs used (47 mm, Anodisc, Whatman) have an average pore diameter of 120–200 nm and a thickness of approximately 60 μm. Tetraethylorthosilicate (TEOS, Aldrich, 99%; 1.87 g, 9 mmol) and (2-cyanoethyl)triethoxysilane (CNTES, Aldrich, 97%; 0.22 g, 1 mmol) were mixed with 0.2 M HCl (Aldrich; 3 g, 0.082 mol), distilled water (from a Millipore system Milli-Q Academic A10, 1.8 g, 0.1 mol), and ethanol (99.9% Aldrich; 5 mL, 0.086 mol), and the mixture was heated at 60 °C for 1 h to pre-hydrolyze the silica precursor under acid-catalyzed conditions. Then the pre-hydrolyzed silica was mixed with a solution of cetyltrimethylammonium bromide (CTAB, Aldrich; 0.236 g, 0.65 mmol) in ethanol (2.25 mL, 0.038 mol). The amount of 0.75 mL of the precursor solution was homogeneously distributed over the whole membrane surface of the AAM. After drying for 3–5 h at room temperature and under controlled humidity (40% r.h.), the membrane appeared dried and homogeneously filled with the mixture. Template removal was carried out first by tempering the sample at 120°C in air for 8 h (ramp 0.4 °C min^{-1}) and further by soxhlet extraction of the template in absolute ethanol for 4 hours. The sample was dried in air and is thereafter called CN-MS. Post-synthetic functionalization with aminopropyl groups was then carried out on this cyanopropyl-functionalized mesoporous silica. In particular, 0.135 g of anodic membrane containing the CN-MS was refluxed under nitrogen atmosphere in a solution of 47.13 μL with aminopropyl trimethoxysilane (APTMES, Aldrich, 99%, 48.4 mg, 0.27 mmol) and 5 mL toluene for 6 hours. The sample, thus called CN+NH_2-MS, was finally washed with acetone and ethanol and dried in air.

To extract both the cyanopropyl-functionalized and the bi-functionalized mesoporous rods from the AAM, a small piece of the samples (approximately: 5 x 5 mm in dimension) was soaked overnight in an Eppendorf containing a solution of 5 %wt phosphoric acid (Sigma TraceSelect Ultra, > 85 %, 2.44 mol) in 0.5 mL Millipore water to dissolve the alumina membrane. The resulting filaments were carefully washed 5 times with Millipore water, centrifuged at 10,000 rcf for 10 min, once in spectroscopic ethanol (Chromasolv, 99.9%, 1.5

mL, overnight in static conditions) and finally redispersed in 0.5 mL of spectroscopic ethanol or, if DNA loading was intended, in 0.5 mL Millipore water.

TDI Dye adsoption into the mesoporous rod

1 µL of N-(2,6-diisopropylphenyl)-N'-(octyl)-terrylene-3,4:11,12-tetracarboxdiimide (AS-TDI, concentration of 10^{-8} M in chloroform), a highly photostable dye with a very high fluorescence quantum yield close to unity, was added to 0.25 mL of the CN-MS filaments solution in spectroscopic ethanol and brought to 0.5 mL by adding additional solvent. After orbital shaking (200 rpm, room temperature in the dark) over night, the TDI-loaded filaments were centrifuged (10,000 rcf for 10 min) and redispersed in 0.25 mL of spectr. EtOH. The amount of 80 µL of this solution was then spin-coated at 1500 rpm for 1 minute onto a pre-cleaned (0.5% Hellmanex II solution, Hellma, at 60 °C, followed by ultrasonication) glass slides (Marienfeld, size: 20 x 20 mm, thickness: 170 µm) for fluorescence microscopy investigation. Some cover slips were coated with a ultra thin layer of gold (0.4 nm) by thermal evaporation (UHV-Aufdampfanlage BESTEC GmbH für 2"-Substrate mit Telemark Mehrtiegel-Elektronenstrahlverdampfer 271/277-32), in order to quench the fluorescence of dye molecules located on the glass substrate or on the outer surface of the mesoporous rods.

DNA adsoption into the mesoporous rod

1 µL of double-strand DNA-Cy3-Cy5 (ds-DNA-Cy3-Cy5, 15 bases: 5`-XCA CGT CGC ATC TTT Cy3-3` and 3`-Bio-AGT GCA GCG TAG AAA Cy5-5, Baseclick, conc. 50 nM in phosphate buffer) with a FRET dye pair were diluted in 0.25 mL solution of mesoporous filaments in Millipore water and 0.25 mL of water were added. Both solutions were stirred under orbital shaking (200 rpm, RT) in the dark for one night or, due to the low adsorption rate of DNA into the mesopores, the uptake was prolonged till one week. The DNA-loaded filaments were then centrifuged (10,000 rcf for 10 min) and redispersed in 0.25 mL of Millipore water. The amount of 80 µL of this solution was then spin-coated at slowly increasing rpm up to 500 for about 20 minutes onto a pre-cleaned glass substrate (as described previously) for fluorescence microscopy investigation. The samples were also coated with a ultra thin layer of gold (as described previously).

Characterization

The AAM-containing mesoporous rods were characterized by small angle X-ray scattering (SAXSess system by Anton Paar). The incident beam was shadowed with a circular beam stop and the signal was recorded after collecting the pattern for 15 min. Nitrogen sorption isotherms were performed on a Quantachrome Nova 4000e at 77K. Sample outgassing was performed at 120 °C, thus the functional groups should remain unaffected at this temperature. Pore size and pore volume were calculated by a NLDFT equilibrium model of N_2 on silica, based on the desorption branch of the isotherms. A BET model was applied to evaluate the surface area. Transmission electron microscopy (TEM, FEI Titan 80-300 KV equipped with a field emission gun) was used to image the mesoporous filaments after the alumina template dissolution. The functionalization of the mesoporous structure was monitored by Fourier-transform infrared spectroscopy (FT-IR) on a Bruker Equinox 55 operating in adsorption mode.

Atomic force microscopy (AFM, Nanoink NScriptor DPN System) in close contact mode was also used to characterize the mesoporous filaments when deposited on the glass substrate.

Wide-field Microscopy and Single Particle Tracking

Fluorescence images were recorded with a wide-field setup, using an Eclipse TE200 (Nikon) epifluorescence microscope with a high numerical aperture oil-immersion objective (Nikon Plan Apo 100x/1.40 N.A. oil). The AS-TDI was excited at 633 nm with a He-Ne gas laser (Coherent) with an intensity of 0.05-0.2 kW cm^{-2}. The ds-DNA with the Cy3-Cy5 FRET pair was excited at 532 nm with a diode pumped solid-state laser (Cobolt Samba TM Laser) with an intensity of 0.05 kW cm^{-2}. The fluorescence was detected with a back-illuminated electron-multiplying charge-coupled device (EM-CCD) camera in frame transfer mode (Andor iXon DV897, 512x512 pixels). Incident laser light was blocked by a dichroic mirror (dual line beamsplitter 532/633, AHF Analysentechnik) and by band-pass filters (675/250 and 560/40 for the green channel and 730/140 for the red channel, AHF Analysentechnik). More details about the setup have been reported previously (see reference [35]).

In order to record the wide-field movies, a sample chamber with a saturated atmosphere of chloroform and water for TDI and only water for DNA was mounted around the samples. The

samples were stored under the corresponding humidity for 10 min before the measurement started. This time proved to be sufficient for equilibration.

Single particle tracking (SPT) was employed to follow the molecules over all frames of the movies to obtain the single trajectories by fitting frame by frame theoretical diffraction patterns (described in detail elsewhere) to the spots. With this method the positions of the fluorophores can be obtained with an accuracy of down to 5 nm. The diffusion coefficient for each individual trajectory can be extracted from the linear part of the MSD plots according to the Einstein-Smoluchowski relation, MSD = 2Dt.

Confocal Microscopy: Measurement of the orientation of TDI dye molecules

For the orientation measurements the mesoporous filaments were investigated with a modified inverted confocal laser scan microscope (ZEISS LSM 410). An oil immersion objective with a high numerical aperture (ZEISS 63× 1.4 oil) and a 633 nm He-Ne laser were used for the excitation of the TDI dye molecules. The fluorescence light was separated from the laser light using a combination of filters consisting of a dichroic mirror (Q640LP AHF Analysentechnik) and a combination of two fluorescence filters (633 nm Notch Kaiser; HQ720/150 AHF Analysentechnik). The fluorescence was detected outside the microscope with a single photon counting avalanche photodiode (EG&G SPCM-AQ 141). To measure the orientation, a rotating, broad band λ/2 plate, which was placed just before the objective, was used to modulate the polarization plane of the excitation light. The fluorescence intensity of the dyes was recorded in dependence of the polarization angle of the excitation light. The orientation of the TDI molecules in the focal plane was determined by fitting a cosine-squared function to the data from a region of interest of 16 × 16 pixels centered on the molecule according to equation 1.

$$I = A_0 \cos^2(\omega t - \Phi_{ref} + \Phi_{mol}) \quad (1)$$

A_0 is the amplitude of the cosine-squared curve, ω the angular rotation velocity of the λ/2 plate, Φ_{ref} the phase of the modulated transmission signal and Φ_{mol} the in-plane angle of the molecule. The zero value for the angle is given by the direction of the main axis of the polarizer, which corresponds here to the horizontal line in the confocal fluorescence images.

The transmission signal was used as reference to obtain the absolute angle of the transition dipole moment. It passed through a polarizer and was recorded simultaneously to the fluorescence signal. The sum of the pixel intensity values of the horizontal lines of the region of interest was plotted versus time, and was fitted with equation 2.

$$I = A_1 \cos^2(\omega t - \Phi_{ref}) \quad (2)$$

A_1 is the amplitude of cosine-squared function, ω the angular speed of the λ/2 plate and Φ_{ref} the phase of the signal.

Characterization results of the mesoporous silica filaments

Prior to TDI or DNA adsorption and diffusion studies, the functionalized mesoporous silica structures inside the alumina membrane were fully characterized by small-angle X-ray scattering (SAXS), nitrogen sorption measurements, and Fourier-transform infrared spectroscopy (FT-IR). After dissolution of the alumina membrane, TEM and atomic force microscopy images were also recorded on the filaments.

Clear evidences of the mesoporosity of the structure are given by both SAXS (see main text) and nitrogen sorption measurements. The nitrogen sorption isotherm (Figure S-1) of the CN-functionalized silica in the AAM (sample CN-MS) is of type IV, which is typical for mesoporous materials, with a defined step around $p/p_0 = 0.35$ due to the filling of the mesopores. The pore diameter was evaluated through the DFT method on the desorption branch, and determined to be 4.2 nm (Figure S-1b and Table S-1). In the isotherm related to the bi-functionalized silica filaments inside the alumina (sample CN+NH_2-MS), the condensation step can be slightly observed. The pore diameter was evaluated through the DFT method on the desorption branch, and determined to be 3.8 nm (Figure S-1b and Table S-1). We assume indeed that the second post-synthetic grafting with aminopropyl-triethoxysilane shifts the pore size distribution peak to lower values, also broadening it, possibly due to the formation of interpore defects, thus modifying the accessibility of nitrogen into the mesoporous structure.

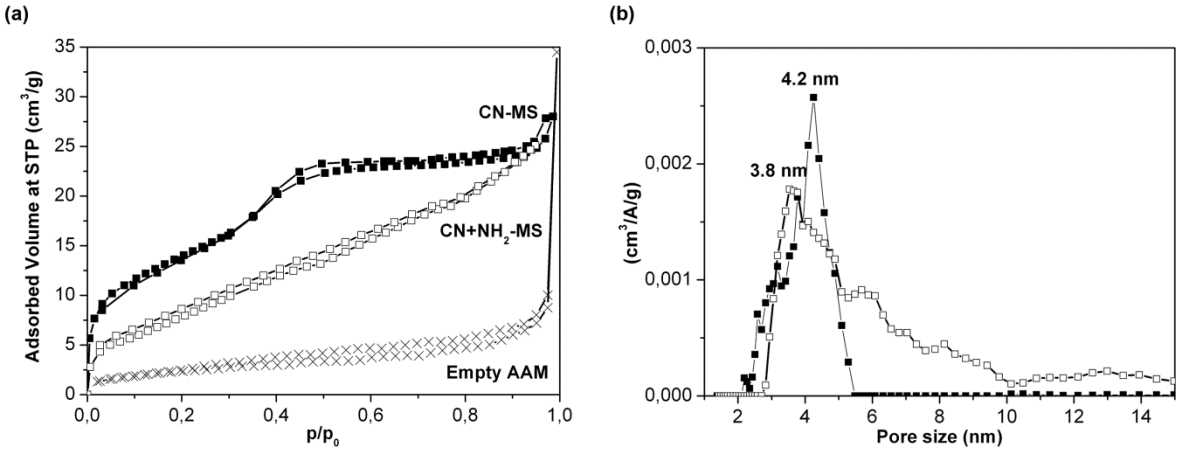

Figure S-1: (a) Nitrogen sorption isotherm and (b) DFT pore size distribution of the CN-functionalized (-o-) and CN+NH_2 functionalized (-■-) mesoporous silica in alumina.

Table S-1: Summary of the structural parameter of the two functionalized mesoporous silica samples confined in the anodic alumina membrane.

Sample	DFT Pore diameter (nm)	BET Surface Area (m^2/g)	Pore Volume (cm^3/g)
CN-MS	4.2	50.9	0.041
CN+NH_2-MS	3.8	29.9	0.037

The FT-IR measurements (Figure S-2) show in the functionalized samples (spectra B and C) the increase of organic moieties in the range 2800-3100 cm^{-1}, assigned to the -CH_x stretching, with respect to an unfunctionalized template-extracted one (spectrum A). The –CH_x stretching vibration originates from the alkyl-chain of the functional groups. In addition, the bi-functionalized sample shows the presence of amine groups in the broad band at around 3200 cm^{-1} and the shoulder at 1590 cm^{-1} (indicated by a dotted line in Figure S-2). The high hydrophilicity of this surface partially covers the amino-groups due to the increase of the bands attributed to water from 3600 to 3200 cm^{-1} and the water bending at 1630 cm^{-1}.

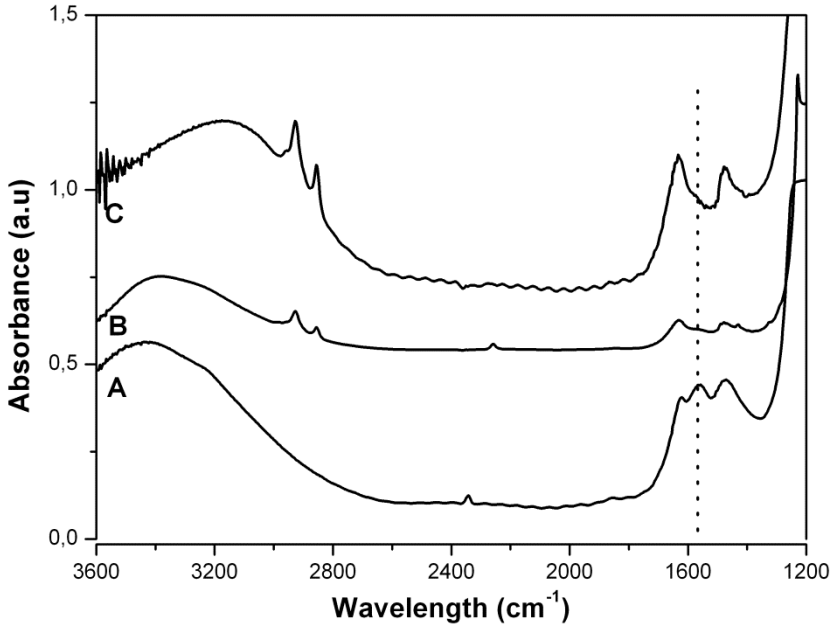

Figure S-2: Fourier-transform infrared (FT-IR) spectra of CN-functionalized mesoporous silica in alumina (spectrum B) and CN+NH_2 functionalized silica (spectrum C) compared to the unfunctionalized mesoporous silica in the alumina membrane (spectrum A). For clarity reasons, the spectra are shifted along the y-axis by 0.25 units.

Prior to fluorescence microscopy measurements, we have investigated the presence of the mesoporous filaments by AFM, collecting topographic images like those shown in Figure S-3.

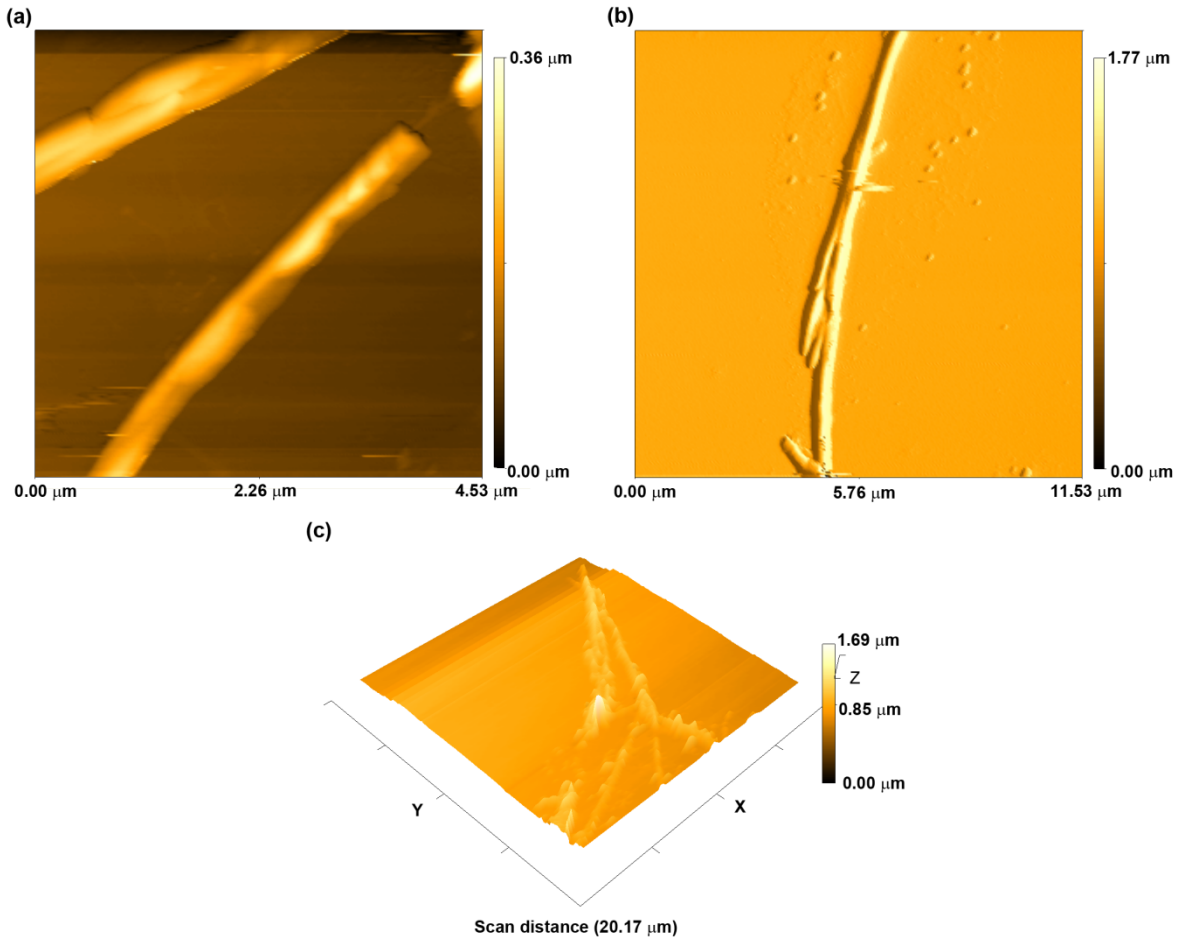

Figure S-3: Topographic images from atomic force microscopy of the (a) and (c) CN-MS filaments and (b) CN+NH_2-MS filaments on the glass substrate prior to single molecule microscopy studies.

Supporting movies available

S-Movie 1: Single TDI dye molecules appearing as bright spots are diffusing linearly along the mesoporous filament under exposure to $CHCl_3$ and H_2O vapors. Additionally, several TDI molecules distributed on the glass substrate are diffusing randomly. (Size: about 35 µm x 35 µm)

S-Movie 2 and 3: Highly structured diffusion of single TDI dye molecules in the mesoporous channels of the filaments under exposure to $CHCl_3$ and H_2O vapors. In contrast to S-Movie 1 a thin layer of gold was deposited on the surface of the sample quenching all dye molecules on the surface of the glass substrate or the mesoporous filaments. (Size: about 35 µm x 35 µm)

S-Movie 4: Single ds-DNA molecules labeled with a Cy3/Cy5-FRET dye pair are diffusing in a highly structured way inside the mesopores of the filaments under exposure to H_2O vapors. Laser excitation of the green Cy3 dye molecules was performed at 532 nm, while detecting the FRET signal of the red Cy5 dyes in the red channel is shown here. (Size: about 35 µm x 35 µm)

References

1. G. Wirnsberger, G. D. Stucky, Ordered mesostructured materials with optical functionality. *A European Journal of Chemical Physics and Physical Chemistry* **1**, 90 (2000).
2. M. Manzano *et al.*, Studies on MCM-41 mesoporous silica for drug delivery: Effect of particle morphology and amine functionalization. *Chemical Engineering Journal* **137**, 30 (2008).
3. V. Cauda, A. Schlossbauer, J. Kecht, A. Zürner, T. Bein, Multiple core-shell functionalized mesoporous silica nanoparticles. *Journal of the American Chemical Society* **131**, 11361 (2009).
4. M. E. Davis, Ordered porous materials for emerging applications. *Nature* **417**, 813 (2002).
5. M. J. Wirth, R. W. P. Fairbank, H. O. Fatunmbi, Mixed Self-Assembled Monolayers in Chemical Separations. *Science* **275**, 44 (1997).
6. S. J. L. Billinge *et al.*, Mercury binding sites in thiol-functionalized mesostructured silica. *Journal of the American Chemical Society* **127**, 8492 (2005).
7. R. Brady, B. Woonton, M. L. Gee, A. J. O'Connor, Hierarchical mesoporous silica materials for separation of functional food ingredients -- A review. *Innovative Food Science & Emerging Technologies* **9**, 243 (2008).
8. H. S. Peng *et al.*, Responsive periodic mesoporous polydiacetylene/silica nanocomposites. *Journal of the American Chemical Society* **128**, 5304 (2006).
9. J. Lei, L. Wang, J. Zhang, Ratiometric pH sensor based on mesoporous silica nanoparticles and Forster resonance energy transfer. *Chemical Communications* **46**, 8445 (2010).
10. W. M. Van Rhijn, D. E. De Vos, B. F. Sels, W. D. Bossaert, P. A. Jacobs, Sulfonic acid functionalised ordered mesoporous materials as catalysts for condensation and esterification reactions. *Chemical Communications*, 317 (1998).
11. D. E. De Vos, M. Dams, B. F. Sels, P. A. Jacobs, Ordered mesoporous and microporous molecular sieves functionalized with transition metal complexes as catalysts for selective organic transformations. *Chemical Reviews* **102**, 3615 (2002).
12. M. Gratzel, Photoelectrochemical cells. *Nature* **414**, 338 (2001).
13. J. Font *et al.*, Periodic mesoporous silica having covalently attached tris(bipyridine)ruthenium complex: synthesis, photovoltaic and electrochemiluminescent properties. *Journal of Materials Chemistry* **17**, 2336 (2007).

14. C.-Y. Lai *et al.*, A Mesoporous Silica Nanosphere-Based Carrier System with Chemically Removable CdS Nanoparticle Caps for Stimuli-Responsive Controlled Release of Neurotransmitters and Drug Molecules. *Journal of the American Chemical Society* **125**, 4451 (2003).
15. V. Cauda *et al.*, Colchicine-Loaded Lipid Bilayer-Coated 50 nm Mesoporous Nanoparticles Efficiently Induce Microtubule Depolymerization upon Cell Uptake. *Nano Letters* **10**, 2484 (2010).
16. A. Schlossbauer *et al.*, A Programmable DNA-Based Molecular Valve for Colloidal Mesoporous Silica. *Angewandte Chemie International Edition* **49**, 4734 (2010).
17. C. Liang, S. Dai, G. Guiochon, Use of gel-casting to prepare HPLC monolithic silica columns with uniform mesopores and tunable macrochannels. *Chemical Communications*, 2680 (2002).
18. V. Rebbin, R. Schmidt, M. Froba, Spherical particles of phenylene-bridged periodic mesoporous organosilica for high-performance liquid chromatography. *Angewandte Chemie International Edition* **45**, 5210 (2006).
19. D. J. Cott *et al.*, Preparation of oriented mesoporous carbon nano-filaments within the pores of anodic alumina membranes. *Journal of the American Chemical Society* **128**, 3920 (2006).
20. A. Keilbach, J. Moses, R. Köhn, M. Döblinger, T. Bein, Electrodeposition of Copper and Silver Nanowires in Hierarchical Mesoporous Silica/Anodic Alumina Nanostructures. *Chemistry of Materials* **22**, 5430 (2010).
21. M. Trau *et al.*, Microscopic patterning of orientated mesoscopic silica through guided growth. *Nature* **390**, 674 (1997).
22. S. H. Tolbert, A. Firouzi, G. D. Stucky, B. F. Chmelka, Magnetic field alignment of ordered silicate-surfactant composites and mesoporous silica. *Science* **278**, 264 (1997).
23. D. Zhao *et al.*, Continuous Mesoporous Silica Films with Highly Ordered Large Pore Structures. *Advanced Materials* **10**, 1380 (1998).
24. H. Miyata, K. Kuroda, Preferred alignment of mesochannels in a mesoporous silica film grown on a silicon (110) surface. *Journal of the American Chemical Society* **121**, 7618 (1999).
25. C. W. Wu, T. Ohsuna, T. Edura, K. Kuroda, Orientational control of hexagonally packed silica mesochannels in lithographically designed confined nanospaces. *Angewandte Chemie International Edition* **46**, 5364 (2007).
26. A. Yamaguchi *et al.*, Self-assembly of a silica-surfactant nanocomposite in a porous alumina membrane. *Nature Materials* **3**, 337 (2004).
27. B. Platschek, N. Petkov, T. Bein, Tuning the structure and orientation of hexagonally ordered mesoporous channels in anodic alumina membrane hosts: A 2D small-angle X-ray scattering study. *Angewandte Chemie International Edition* **45**, 1134 (2006).
28. C. J. Brinker, Y. Lu, A. Sellinger, H. Fan, Evaporation-induced self-assembly: Nanostructures made easy. *Advanced Materials* **11**, 579 (1999).
29. T. Lebold *et al.*, Controlling The Mobility Of Oligonucleotides In The Nanochannels Of Mesoporous Silica. *Advanced Functional Materials* **22** 106 (2012).
30. V. Kukla *et al.*, NMR Studies of Single-File Diffusion in Unidimensional Channel Zeolites. *Science* **272**, 702 (1996).
31. F. Stallmach, J. Kärger, C. Krause, M. Jeschke, U. Oberhagemann, Evidence of anisotropic self-diffusion of guest molecules in nanoporous materials of MCM-41 type. *Journal of the American Chemical Society* **122**, 9237 (2000).

32. S. G. Choi *et al.*, Application of mesoporous TiO_2 as a thermal isolation layer for infrared sensors. *Thin Solid Films* **516**, 212 (2007).
33. M. Klotz *et al.*, The true structure of hexagonal mesophase-templated silica films as revealed by X-ray scattering: Effects of thermal treatments and of nanoparticle seeding. *Chemistry of Materials* **12**, 1721 (2000).
34. F. O. Holtrup *et al.*, Terrylenimides: New NIR fluorescent dyes. *Chemistry-a European Journal* **3**, 219 (1997).
35. J. Kirstein *et al.*, Exploration of nanostructured channel systems with single-molecule probes. *Nature Materials* **6**, 303 (2007).
36. C. Jung *et al.*, Diffusion of oriented single molecules with switchable mobility in networks of long unidimensional nanochannels. *Journal of the American Chemical Society* **130**, 1638 (2008).
37. P. Horcajada *et al.*, Porous metal–organic-framework nanoscale carriers as a potential platform for drug delivery and imaging. *Nature Materials* **9**, 172 (2009).
38. C. Jung *et al.*, Visualization of the self-assembly of silica nanochannels reveals growth mechanism. *Nature Nanotechnology* **6**, 86 (2011).
39. F. Feil *et al.*, Diffusional and orientational dynamics of various single terylene diimide conjugates in mesoporous materials. *Microporous and Mesoporous Materials* **125**, 70 (2009).
40. Y. Wang, F. Caruso, Mesoporous Silica Spheres as Supports for Enzyme Immobilization and Encapsulation. *Chemistry of Materials* **17**, 953 (2005).
41. A. Schlossbauer, D. Schaffert, J. Kecht, E. Wagner, T. Bein, Click Chemistry for High-Density Biofunctionalization of Mesoporous Silica. *Journal of the American Chemical Society* **130**, 12558 (2008).
42. C. Bustamante, J. F. Marko, E. D. Siggia, S. Smith, ENTROPIC ELASTICITY OF LAMBDA-PHAGE DNA. *Science* **265**, 1599 (1994).

4.2 Diffusional and orientational dynamics of various single terrylene diimide conjugates in mesoporous materials

F. Feil, C. Jung, J. Kirstein, J. Michaelis, C. Li, F. Nolde, K. Müllen, C. Bräuchle, Diffusional and orientational dynamics of various single terrylene diimide conjugates in mesoporous materials. *Microporous and Mesoporous Materials* (Special Issue: Diffusion in micropores) **125**, 70 (2009).

Author contributions

F.F. performed the single molecule experiments and analyzed the single molecule data. This work started as master thesis of F.F. and was finished in his PhD time.

Mesoporous silica materials are ideally suited as host-guest systems in nanoscience with applications ranging from molecular sieves, catalysts, nanosensors to drug delivery systems. For all these applications a thorough understanding of the interactions between the mesoporous host system and the guest molecules is vital. Here, we investigate these interactions using single molecule spectroscopy (SMS) to study the dynamics of three different terrylene diimide (TDI) dyes acting as molecular probes in hexagonal and lamellar mesoporous silica films. The diffusion behaviour in the hexagonal phase is represented by the trajectories of the single molecules. These trajectories are highly structured and thus provide information about the underlying host structure, such as domain size or the presence of defects inside the host structure. The three structurally different TDI derivatives allowed studying the influence of the molecular structure of the guest on the translational diffusion behaviour in the hexagonal phase and the lamellar phase. In the lamellar phase, the differences between the three guests are quite dramatic. First, two populations of diffusing molecules - one with parallel orientation of the molecules to the lamellae and the other with perpendicular orientation - could be observed for two of the TDI derivatives. These populations differ drastically in their translational diffusion behaviour. Depending on the TDI derivative, the ratio between the two populations is different. Additionally, switching between the two populations was observed. These data provide new insights into host-guest interactions like the influence of the molecular

structure of the guest molecules on their diffusional as well as on their orientational behaviour in structurally confined guest systems.

Introduction

Ordered mesoporous silica materials have recently advanced to an important field of research attracting interest not only in the scientific community, but also by the chemical industry as it offers many promising approaches for new high-tech materials. Indeed, they provide very interesting host systems for many inorganic, organic as well as biological guest molecules. Moreover, the wide range of possible sizes, topologies and polarity of these host systems allows for a specific design of the desired host-guest interactions. Examples of potential applications are molecular sieving and filter membranes,[1, 2] ion exchanger,[3, 4] sensor systems,[5] laser media,[6-8] catalysts[9] or novel drug-delivery-systems.[10, 11]

For most applications the interactions between the mesoporous host and the guest molecules play a crucial role. Whereas Ensemble-measurements like NMR,[12] electron microscopy,[13] X-ray diffraction or neutron scattering[14] provide only information about the mean behaviour of the host-guest system, single molecule spectroscopy (SMS) offers insight into heterogeneities of the system and mechanistic details of dynamic processes such as spectral,[15] orientational,[16-18] and lateral diffusion.[19-22] In a recent contribution we showed how single terrylene diimide (AS-TDI, structure shown in Figure 1c) molecules can be used to investigate hexagonal and lamellar phases of Brij-56 templated mesoporous thin films[22] (a scheme of the two topologies and the structure of the template molecule are shown in Figure 1a). The dye molecules can be incorporated as guests in the template filled channels of such mesostructured materials during the synthesis procedure. In such a system the microscopic environment of the guest molecules is complex: the template micelles act as solvent for the hydrophobic AS-TDI molecules and interactions with the silica walls occur during their walk.[23] Furthermore, small molecules coming from the surrounding atmosphere like water are always present in the channels, influencing the diffusion properties.[24-26] Hence, the single dye molecules act as ideal molecular probes providing structural as well as dynamical information about the host. For example, single AS-TDI molecules could be observed travelling in the different topologies of the host systems. It was even possible to

distinguish AS-TDI molecules diffusing along the channels of the hexagonal phase from those that move very slowly in the lamellar galleries. In addition, direct information about the dynamics inside of the host system could be obtained by analyzing the single molecule trajectories. In particular, the heterogeneities of the host systems are reflected by the complex modes of motions observed for the single guest molecules.

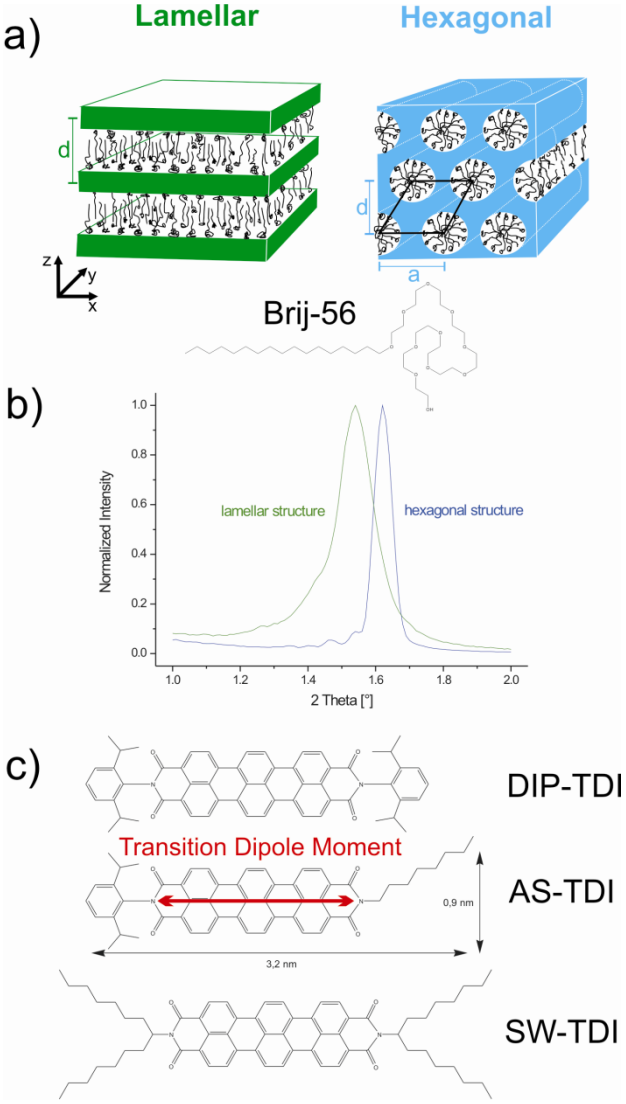

Figure 1: Overview of the host-guest system. a) Schematic diagrams of the lamellar (upper left panel) and the hexagonal (upper right panel) topologies and the respective arrangement of the template Brij-56 (structure shown in the lower panel). b) Small-angle X-ray diffraction patterns of the two mesoporous structures exhibiting a sharp peak. The lamellar phase has a layer-to-layer distance d = 5.7 ± 0.1 nm, and for the hexagonal phase d = 5.5 ± 0.1 nm (pore-to-pore distance a = 6.3 ± 0.1 nm). c) Structures of the three TDI derivatives: DIP-TDI, AS-TDI and SW-TDI.

As the host-guest interactions are expected to strongly depend on the chemical nature of both host and guest, it is of great interest to study the influence of the chemical structure of the guest molecules. This knowledge is crucial for most applications since these mesoporous systems are designed for incorporating various guest species. So far, we investigated the interplay between guest and host with the same guest molecule (AS-TDI) in different host systems.[22] AS-TDI is an asymetric molecule based on a two dimensional strongly fluorescent terrylene diimide core with an octyl tail at one end of the molecule and an 2,6-diisopropyl-phenyl substituent at the other end. In this work we used SMS to investigate the orientational and translational dynamics of three different TDI derivatives diffusing in hexagonal and lamellar phases of Brij-56 templated mesoporous films. The structural differences between the different TDI derivatives are based on the nature of the substituents (structures shown in Figure 1b). DIP-TDI and SW-TDI are two symmetric molecules with two 2,6-diisopropyl-phenyl and two 1-heptyl-octyl substituents, respectively. The third TDI derivative is the asymmetric AS-TDI molecules already used. In the following, it will be shown how the different substituents influence the interactions between the different guest molecules and the template-filled pores and lamellas, leading to dramatically different diffusional as well as orientational behaviours of the dye molecules.

Experimental Section

Synthesis. The silica films were prepared by Evaporation-Induced Self-Assembly (EISA). The precursor solutions were synthesized by mixing 2.08 g (0.01 mmol) tetraethyl orthosilicate (TEOS, Aldrich) with 3.00 g 0.2 M HCl, 1.80 g H_2O and 7.90 g EtOH and heating at 60°C for 1 h to prehydrolyze the silica precursor under acid-catalysed condition. Then 0.57 g or 2.72 g of the structure building agent Brij-56 in 7.80 g or 37.5 g EtOH were added to obtain a hexagonal or lamellar mesoporous structure, respectively. Moreover, 4 µl of a highly diluted solution (about 10^{-8} M) of a terrylene diimide (TDI) dye (AS-TDI, DIP-TDI or SW-TDI) was added to 1 ml of the precursor solutions. Finally, 80 µl of the solutions were spin-coated on previously cleaned glass substrates (Marienfeld, size 20 x 20 mm, thickness 170 µm) at 3000 rpm.

Ellipsometry. The thickness of the mesoporous films was obtained using a Woollam ESM-300 Ellipsometer.

X-Ray Diffractometry (XRD). The structure of the mesoporous films was determined with a Scintag XDS 2000 diffractometer in Bragg-Bretano scattering geometry.

Wide-Field Microscopy and Single Particle Tracking (SPT). Fluorescence images were acquired with a wide-field setup, using a Nikon Eclipse TE200 epifluorescence microscope using an oil-immersion objective with high numerical aperture (Nikon Plan Apo 100x/1.40 N.A. Oil). The TDI dye molecules were excited at 633 nm with a Coherent He-Ne gas laser (75 mW max. at 632.8 nm) with an intensity of 0.3 kW cm^{-2}. The Fluorescence was detected with an Andor iXion DV897 back-illuminated EM-CCD camera in frame transfer mode (512 x 512 px). Incident laser light was blocked by a dichroic mirror (640 nm cutoff, AHF) and a band-pass filter (730/140, AHF). More details about the setup have been reported previously.

Confocal Microscopy: Measurement of the orientation of the different TDI derivatives in the lamellar phase. For the orientation measurements the mesoporous films were investigated with a modified inverted confocal laser scan microscope (ZEISS LSM 410). An oil immersion objective with a high numerical aperture (ZEISS 63× 1.4 oil) and a 633 nm He-Ne laser were used for the excitation of the TDI dye molecules. The fluorescence light was separated from the laser light using a combination of filters consisting of a dichroic mirror (Q640LP AHF Analysentechnik) and a combination of two fluorescence filters (633 nm Notch Kaiser; HQ720/150 AHF Analysentechnik). The fluorescence is detected outside the microscope with a single photon counting avalanche photodiode (EG&G SPCM-AQ 141). For the measurements of the pure lamellar phase, the bottom of the substrate was embedded in water to obtain a better matching of the refractive indices. To measure the orientation, a rotating, broad band λ/2 plate, which is placed just before the objective, is used to modulate the polarization plane of the excitation light. The fluorescence intensity of the dyes is recorded in dependence of the polarization angle of the excitation light. The orientation of the TDI molecules in the focal plane was determined by fitting a cosine-squared function to

the data from a region of interest of 16 × 16 pixels centered on the molecule according to equation 1.

$$I = A_0 \cos^2(\omega t - \Phi_{ref} + \Phi_{mol}) \quad (1)$$

A_0 is the amplitude of the cosine-squared curve, ω the angular rotation velocity of the λ/2 plate, Φ_{ref} the phase of the modulated transmission signal and Φ_{mol} the in-plane angle of the molecule. The zero value for the angle is given by the direction of the main axis of the polarizer, which corresponds here to the horizontal line in the confocal fluorescence images.
The transmission signal was used as reference to obtain the absolute angle of the transition dipole moment. It passed through a polarizer and was recorded simultaneously to the fluorescence signal. The sum of the pixel intensity values of the horizontal lines of the region of interest was plotted versus time, and was fitted with equation 2.

$$I = A_1 \cos^2(\omega t - \Phi_{ref}) \quad (2)$$

A_1 is the amplitude of cosine-squared function, ω the angular speed of the λ/2 plate and Φ_{ref} the phase of the signal.
Experiments have been carried out with a pure lamellar phase film aligned perpendicular to the focal plane containing TDI molecules at high concentration (10^{-5} M in the synthesis solution).

Results and Discussion

The investigated mesoporous silica materials were synthesized as thin films by spontaneous self-assembly of template and polymerisable silica precursor molecules.[27] Depending on the surfactant / silica molar ratio, we could produce either hexagonal or lamellar phases (for details see Experimental Section). The different TDI molecules were inserted at very low concentration (10^{-10} M) in the synthesis solutions of the mesoporous films to ascertain single molecule observation.

X-Ray Diffractometry (XRD) was first used to determine the structure of the mesoporous films. Typical X-ray diffractograms are shown in Figure 1b for a hexagonal and a lamellar topology (blue and green plots, respectively). Both curves exhibit a sharp peak, indicating that the hexagonal and lamellar mesoporous phases are well structured. The 2θ values of the peaks can be used to calculate the average pore-to-pore distance *a* and the layer-to-layer distance *d* (see Fig 1a). In the case of the hexagonal phase we find 2θ = 1.62 °, which results in *a* = 6.3 ± 0.1 nm and *d* = 5.5 ± 0.1 nm. For the lamellar phase the 2θ value of the maximum is 2θ = 1.54 °, resulting in a layer-to-layer distance *d* = 5.7 ± 0.1 nm. As in these systems the wall thickness lies typically in the range of 1-2 nm, the pore diameter of the hexagonal structure would amount to about 4 - 5 nm, while the spacing of the lamellas is about 0.5 nm smaller. These values, however, can vary with time due to silica condensation leading to shrinkage of the mesoporous films.[28] Hence, all measurements presented here were carried out at the same time (2 days after synthesis) to assure comparability. X-Ray Diffractometry is a typical ensemble method which does not provide any information about the host-guest interactions and dynamics. Therefore, we used SMS to overcome this drawback.

Wide-field microscopy was performed to collect the fluorescence signal of the dye molecules and monitor their pathways inside the porous systems. Series of 1000 frames were recorded with a temporal resolution of down to 100 ms per frame. The insert in Figure 2a shows a typical fluorescence image extracted from a movie of DIP-TDI molecules travelling in a hexagonal mesoporous phase. The single dye molecules appear as bright spots on a dark background. Single particle tracking (SPT) was employed to follow the molecules over all frames of the movies to obtain the single trajectories by fitting frame by frame theoretical diffraction patterns to the spots. With this method the positions of the fluorophores can be obtained with an accuracy of down to 10 nm.[29] Here we present first the results for the single molecule diffusion of the three TDI derivatives in the hexagonal phase, and then discuss the translational diffusion as well as the orientational behaviour of the guest molecules in the lamellar samples.

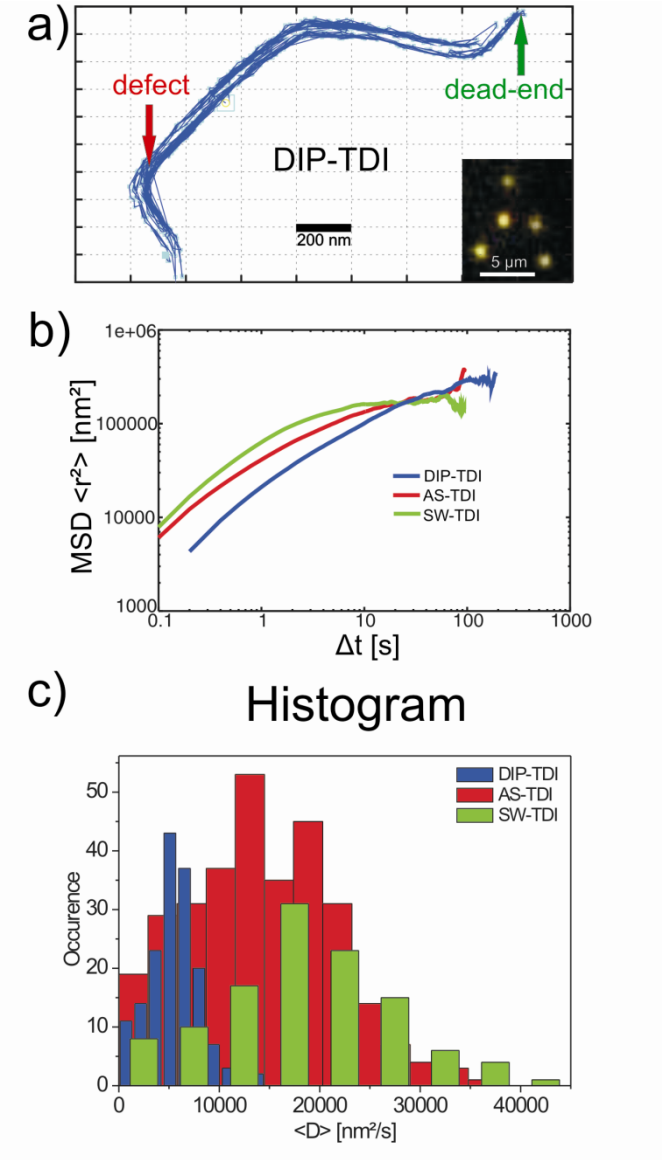

Figure 2: Diffusional behaviour of the three TDI dyes in the hexagonal pore system. a) Highly structured trajectory of a single DIP-TDI molecule travelling inside the hexagonal channels. The insert displays a wide-field fluorescent image extracted from a movie (Movie 1 in Supplementary Materials) showing single DIP-TDI molecules diffusing in a hexagonal mesoporous film. b) Mean square displacements (MSD) versus time averaged over about 250 single molecules trajectories for DIP-TDI (blue line), AS-TDI (red line) and SW-TDI (green line). c) Histogram of the mean diffusion coefficients *D* extracted from the linear part of the individual MSD plots for the three TDI derivatives.

Figure 2 shows the results for the hexagonal samples. Movies 1-3 (in Supplementary Material) show the diffusion in hexagonal samples of single DIP-TDI, AS-TDI and SW-TDI molecules, respectively. Similarly to what is observed in Figure 2a for DIP-TDI, the single

molecules of AS-TDI and SW-TDI appear solely as Gaussian-shaped diffraction patterns in the wide-field movies. Another immediate observation is that all the three TDI-dyes exhibit a very structured diffusional behaviour. A typical trajectory is displayed in Figure 2a for DIP-TDI. The pathway of the molecule can be nicely followed as it explores the nanochannel system. This provides detailed information about the host structure such as sizes of domains of parallel pores and can reveal the presence of defects within the host structure like dead ends (green arrow) where the pores are closed. Also small openings have to be present in the silica walls (red arrow) through which the dye molecule can move to neighbouring channels as seen in high resolution experiments.[30] A statistical analysis based on the mean-square displacements (MSD) was performed for about 250 single molecule trajectories of each TDI derivative. For clarity, only the average MSD over all trajectories is plotted versus time in Figure 2b for DIP-TDI (blue line), AS-TDI (red line) and DIP-TDI (green line). From this graph it becomes apparent that for short time lags the MSDs of each dye are linear and well separated, and for large time intervals they bend towards the similar horizontal asymptote at about 200,000 nm^2. This behaviour is characteristic for confined diffusion and does not just reflect the channel curvature since we found nearly perfectly linear trajectories exhibiting a similar bending of the MSD plot. It is known that the hexagonal mesoporous structures are organized in small domains of parallel channels.[31-33] Such domains correspond to the confinement regions, which is confirmed by the fact that the confinement areas of all the trajectories are in the same order of magnitude giving directly the typical domain size. The diffusion coefficients for each individual trajectory can be extracted from the linear part of the MSD plots according to the Einstein-Smoluchowski relation,

$$MSD = 4\,D\,t \qquad (3)$$

assuming a two-dimensional Brownian diffusion for the step sizes much smaller than the confinement area (in this case the ten first step sizes were taken into account). Figure 2c displays the histograms of the diffusion coefficients for all the single trajectories of the three TDI conjugates. Clearly, the distributions are well separated with the trend for the diffusion coefficients: $\langle D \rangle_{SW\text{-}TDI} > \langle D \rangle_{AS\text{-}TDI} > \langle D \rangle_{DIP\text{-}TDI}$. The mean diffusion coefficients and their standard deviations are shown in Table 1.

Table 1: Diffusion coefficients and standard deviations of the three TDI derivatives in the hexagonal phase.

Dye	<D> [nm²/s]
DIP-TDI	$(0.6 \pm 0.2) \cdot 10^4$
AS-TDI	$(1.3 \pm 0.9) \cdot 10^4$
SW-TDI	$(1.9 \pm 0.7) \cdot 10^4$

The differences between the diffusion coefficients of the different TDI-dyes are induced by the different interactions of the substituents with the template molecules and the silica walls. It is known that the guest molecules can interact strongly with the silica walls of the mesoporous host structure at adsorption sites such as silanol groups.[2, 23-25, 34] This phenomenon hinders the diffusion, giving rise to lower diffusion coefficients. SW-TDI, with four alkyl chains, is expected to dissolve better than AS-TDI (with only one alkyl chain) in the cylindrical micelles of Brij-56. Hence, the tendency to adsorb occasionally to the silica walls is lowered, leading to a higher diffusion coefficient. DIP-TDI, with no alkyl chains, has consequently the lowest mean diffusion coefficient. The standard deviations given in Table 1 were obtained from the width of the Gaussian fit of the histograms in Figure 2c. They reflect the presence of heterogeneities in the system, e.g. of the silica matrix, template arrangement or structure of the guest molecule.

Whereas different TDI structures result mainly in different diffusion coefficients in the hexagonal phase, the picture is much more complex with the lamellar samples. Figure 3a shows a frame extracted from a sequence of wide-field fluorescence images (Movie 4 in Supplementary Material) acquired with a time resolution of 100 ms / frame, and showing single DIP-TDI molecules diffusing in a lamellar phase. The dye molecules appear with the typical Gaussian-shaped diffraction patterns, and exhibit a fast, totally unstructured diffusion. Figure 3b displays an exemplary trajectory of such a DIP-TDI molecule diffusing in a random manner. This stands in contrast with the highly structured trajectories obtained in the hexagonal phase (illustrated in Figure 2a), and is consistent with the random motion in the surfactant layers between the silica planes which allows two-dimensional diffusion. For AS-TDI and SW-TDI, the picture becomes more complicated. Indeed, the observation of the

wide-field images of these two conjugates in the lamellar topologies reveals the presence of two populations of single molecule patterns as can be seen in Figures 3c and 3e (frames extracted from Movies 5 and 7 for AS-TDI, and Movies 6 and 8 for SW-TDI in Supplementary Materials). One population exhibits fast and the other one slow diffusion. Therefore, these fluorescence images recorded from the same sample of a given TDI derivative were measured with two different integration times (100 ms / frame for the left panels; 8s / frame for the right panels) which allows resolving the dynamics occurring at different timescales. The two movies acquired with short integration time (100 ms / frame) show for both dyes fast, randomly diffusing molecules appearing with Gaussian-shaped diffraction patterns, similarly to what was observed with DIP-TDI. In contrast, in the movies acquired with longer integration time (8 s / frame) the single molecules appear as doughnuts. Such doughnut-shaped diffraction patterns have been previously reported in the lamellar phase for AS-TDI[22] and have been assigned to single molecules whose transition dipole moment (for TDI conjugates the long molecular axis) is constantly aligned along the optical axis of the microscope. This means that these molecules are oriented perpendicular to the glass substrate and thus normal to the silica planes of the lamellar phase. An additional observation is that the doughnuts move in a random way similarly to the Gaussian-shaped molecules as can be seen in the trajectory displayed in Figure 3d. However, the diffusion of the doughnuts is much slower according to the 80-times longer integration time. In our previous work we explained the preferential z-orientation of the doughnuts by strong interactions between the AS-TDI molecules and the template molecules. This results in the alignment of the AS-TDI molecules along the template chains, i.e. perpendicular to the silica layers. Obviously, in the case of DIP-TDI these interactions are not strong enough to be able to orient the molecules, which is probably due to the absence of an alkyl tail in the guest structure. Hence, the DIP-TDI molecules are able to take different orientations within the surfactant-filled layers. In the case of SW-TDI which have four alkyl chains we observe behaviour similar to the one of AS-TDI. Indeed, two populations of diffusing molecules are observed: fast Gaussian-shaped molecules and slow doughnut-shaped molecules oriented perpendicular to the mesoporous film.

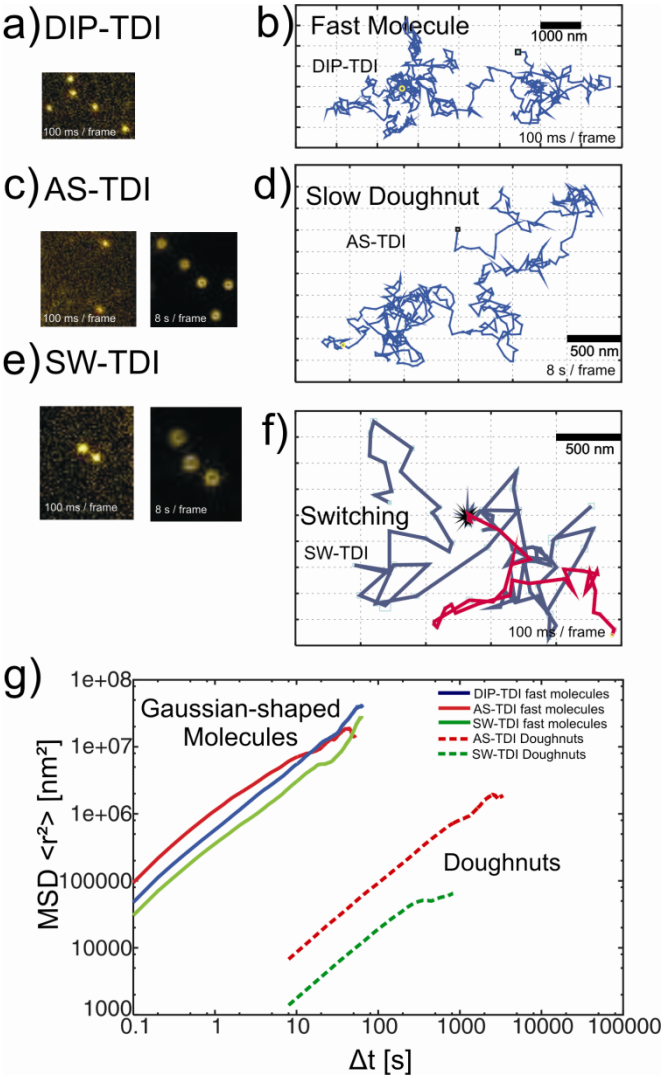

Figure 3: Diffusional and orientational behaviour of the three TDI dyes in the lamellar structure. a) Wide-field fluorescence images of single DIP-TDI molecules acquired with 100 ms / frame. b) Trajectory of a fast Gaussian-shaped DIP-TDI molecule travelling randomly inside the template-filled lamellas. c) Wide-field images of single AS-TDI molecules diffusing in a lamellar phase acquired with 100 ms / frame (left panel) and 8 s / frame (right panel) showing Gaussian- and doughnut-shaped molecules, respectively. d) Unstructured trajectory of a slow, z-oriented AS-TDI doughnut-shaped molecule. e) Wide-field images of single SW-TDI molecules acquired with 100 ms / frame and 8 s / frame. f) Individual SW-TDI molecule undergoing switches between Gaussian- (red and blue tracks) and Doughnut-shaped pattern (black track). g) Mean square displacements (each curve averaged over about 30 single molecule trajectories) for the three TDI conjugates diffusing in the lamellas. Two populations can be distinguished: Fast molecules with Gaussian-shaped patterns (straight lines) and slow molecules with doughnut-shaped patterns (dotted lines).

In summary, DIP-TDI molecules diffusing in a lamellar phase exhibit Gaussian-shaped patterns, whereas for AS-TDI and SW-TDI one can distinguish two sub-populations of diffusing single molecules: fast Gaussian-shaped and slow doughnut-shaped molecules oriented perpendicular to the silica planes. We estimated roughly the ratio of the two populations by counting the number of Gaussian- and doughnut-shaped molecules (see Table 2).

Table 2: Ratio of fast Gaussian-shaped molecules to slow Doughnut-shaped molecules for the three TDI dyes in the lamellar phase.

Dye	Ratio (Gaussian-shaped molecules (fast) / Doughnut-shaped molecules (slow)) [%]
DIP-TDI	100 : 0
AS-TDI	10 : 90[35]
SW-TDI	45 : 55

Hence, while no doughnut at all could be observed with DIP-TDI, the AS-TDI molecules exhibit about 90% doughnuts, and in the case of SW-TDI we found a ratio of about 1:1 for the two populations.

Interestingly, transitions between the sub-populations could even be observed for AS-TDI as well as for SW-TDI. This is illustrated in Figure 3f which shows the trajectory of a single SW-TDI molecule travelling at first rapidly with a Gaussian-shaped pattern (red track), and after 8.6 s switches its shape into a doughnut (black) being nearly immobile at this integration time (100 ms / frame). Then, 12.7 s later, the molecule's shape changes again into a Gaussian-shaped pattern diffusing fast again (blue track). Such switches transforming fast Gaussian-shaped molecules into slow doughnuts and the other way round are encountered occasionally (roughly one switching event is observed after 2 min of observation time for about 20 % of the molecules, the other molecules showing no switching event). They indicate a sudden change in the orientation of the molecules accompanied with a dramatic change of the diffusion coefficient.

The average MSDs for the Gaussian- and the doughnuts-shaped molecules are plotted in Figure 3g for DIP-TDI (blue line), AS-TDI (full and dotted red lines, respectively), and SW-TDI (full and dotted green lines, respectively). All the MSD plots are linear, confirming that the diffusion behaviour of both populations for the three TDI derivatives can be described by two-dimensional random walks. The mean diffusion coefficients were obtained with linear fits of the MSD plots according to equation 3 and are shown in Table 3.

Table 3: Diffusion coefficients and standard deviations of the three TDI derivatives in the lamellar phase.

Dye	Gaussian-shaped molecules		Doughnut-shaped molecules
	<D> [nm²/s]	<D>(lam)/<D>(hex)	<D> [nm²/s]
DIP-TDI	$(1.6 \pm 0.5) \cdot 10^5$	26.7	-
AS-TDI	$(2.8 \pm 0.7) \cdot 10^5$	17.5	230 ± 120
SW-TDI	$(0.8 \pm 0.4) \cdot 10^5$	4.2	65 ± 82

Overall, the diffusion coefficients of the fast TDI molecules with Gaussian-shaped patterns in the lamellar structure are about one order of magnitude higher than in the hexagonal pores. This may be explained by the more dense packing of the surfactant molecules in the hexagonal phase leading to a more viscous medium. Indeed, a perfect coverage of the silica walls with template molecules would result in a much higher density of the alkyl chains of Brij-56 in the middle of the pore due to the cylindrical geometry in the hexagonal phase. However, the trend in the lamellar phase ($\langle D \rangle_{AS\text{-}TDI} > \langle D \rangle_{DIP\text{-}TDI} > \langle D \rangle_{SW\text{-}TDI}$) is also different than in the hexagonal phase ($\langle D \rangle_{SW\text{-}TDI} > \langle D \rangle_{AS\text{-}TDI} > \langle D \rangle_{DIP\text{-}TDI}$). Indeed, the ratio between the diffusion coefficients in the lamellar and the hexagonal phase (<D>(lam)/<D>(hex)) is very different for the three TDI derivatives as shown in Table 3. Whereas DIP-TDI diffuses 26.7 times faster in the lamellar than in the hexagonal structure, AS-TDI diffuses 17.5 times faster and SW-TDI only 4.2 times.

In particular, SW-TDI, which was the fastest dye inside the hexagonal pores, becomes the slowest one between the lamellas. These strong differences in the diffusional behaviour are

unexpected, and are likely caused by the different geometry of the silica structure as well as the template's arrangement in the lamellar phase, which may induce different host-guest interactions. For example, the alkyl chain of AS-TDI might interact stronger with the parallel alkyl chains of the template in the lamellar phase than with the radial oriented template in the hexagonal phase. Hence, the movement of the dye is hindered in the lamellar phase compared to DIP-TDI, which has no alkyl chain. This effect seems even stronger for SW-TDI, whose all four alkyl chains might even align parallel to the template molecules in the lamellar structure.

Furthermore, another striking observation is that the diffusion coefficients of the doughnuts are about three orders of magnitude lower than those of the Gaussian-shaped molecules. The AS-TDI and SW-TDI doughnuts are most probably hindered in their movement by strong interactions with the surfactant molecules aligned parallel. This assumption is supported by the 3.5 times lower diffusion coefficient of the doughnuts of SW-TDI compared to those of AS-TDI (230 nm^2 / s and 65 nm^2 / s, respectively). Indeed, it is expected that the four chains of SW-TDI induce more interactions with the template molecules than the single octyl chain of AS-TDI, hence hindering the movement. Finally, for the Gaussian-shaped molecules in the lamellar phase the same trend for the diffusion coefficients was observed: $D_{AS\text{-}TDI} > D_{SW\text{-}TDI}$. This is a hint, that for the two populations the relative interactions of AS-TDI and SW-TDI molecules with the template are similar and depend only on the structures of the dye molecules, i.e. in this case on the alkyl chains. Therefore, SW-TDI molecules holding four alkyl chains present stronger interactions with the alkyl chains of the template than AS-TDI with only one alkyl chain and consequently being slowed down in a stronger way.

The presence of two populations of diffusing molecules in the lamellar phase as well as of switching events between those is quite surprising. The Wide-field measurements indicate already that the two populations exhibit a different orientational behaviour. It has also been shown that for one population the TDI molecules are oriented perpendicular to the substrate, showing up as doughnut diffraction limited patterns. However, the orientation of the fast molecules forming the second population is not known exactly. To gain a deeper insight, polarization modulation dependent confocal microscopy was used to measure the orientational behaviour of the TDI conjugates in the lamellar phase. Hence, a sample was

observed from the side in order to obtain a better excitation of the fluorophores, especially of the doughnuts (see Figure 4a). The dye molecules were embedded in the mesoporous film at ensemble concentration to provide a sufficient fluorescence signal in this geometry, and the excitation polarization of the laser was rotated continuously (for details see Experimental Section).

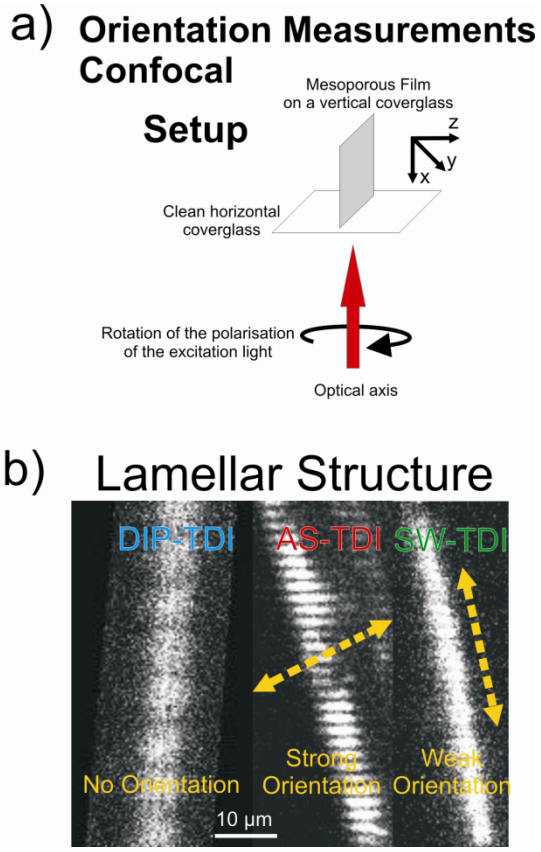

Figure 4: Measurements of the orientation of the TDI conjugates in the lamellar phase. a) Sketch of the alignment of the lamellar film perpendicular to the focal plane. b) Polarization modulated confocal images for DIP-TDI (left panel), AS-TDI (middle panel), and SW-TDI (right panel) inside the lamellar phase. Whereas DIP-TDI exhibits a homogeneous fluorescence signal indicating that its molecules can rotate freely inside the lamellas, the AS-TDI shows a striped fluorescence pattern which reveals an overall strong orientation perpendicular to the silica lamellas. In the case of SW-TDI, the fluorescence signal is only weakly polarized, indicating a more complex orientational behaviour (see text for details).

Figure 4b (left panel) shows an excerpt extracted from the fluorescence image of a lamellar phase loaded with DIP-TDI. The mesoporous film appears here as a bright, homogeneous

fluorescence signal. As the excitation polarization of the laser was rotated continuously during the confocal scan this means that the transition dipole moments of the DIP-TDI molecules point in every direction, and consequently has no preferential orientation. This is consistent with the wide-field measurement in which the single DIP-TDI molecules appear only as Gaussian-shaped patterns. These observations suggest that the DIP-TDI is able to rotate freely within the lamellas. Indeed, the inter-plane distance, estimated to be 3.7-4.7 nm, provides enough space for the DIP-TDI molecules (about 3 nm in length) to reorient their dipole moments. This also indicates that the interactions with the template are most probably much weaker than for AS-TDI and SW-TDI, probably because of the absence of alkyl chains in the structure of DIP-TDI.

In contrast, the fluorescence of the mesoporous film loaded with AS-TDI appears as a thin, striped vertical line, as shown in Figure 4b (middle panel). This reveals that the AS-TDI dye molecules are not oriented randomly within the lamellar phase, but are mostly aligned in the same direction. This was indeed expected as most of the molecules appear as doughnuts in the wide-field images. To determine the average direction of the alignment the modulation of the transmission light was detected behind a fixed polarizer and acts as a reference for the determination of the angles (the angle of a horizontal line in Figure 4b is set to 0°). Both fluorescence and reference images were used to determine the orientation at several chosen positions (for details, see Experimental Section). The average extracted angle is 15° ± 3°, which is the mean angle of the distribution of the orientations of the transition dipole moments of the AS-TDI molecules. This angle corresponds exactly to the direction perpendicular to the mesoporous film and thus perpendicular to the silica planes of the lamellar phase, which is consistent with the z-oriented doughnuts observed in the wide-field movies. However, the orientation of the other population of Gaussian-shaped pattern molecules could not be determined by the confocal measurements. As AS-TDI was used at an ensemble concentration, this population constituted by only 10% of the molecules shows much weaker fluorescence intensity than the other population which is overlaid in the fluorescence image, and hence can not be easily detected. However there are two possibilities for the configuration for the transition dipole moment of these molecules leading to Gaussian-shaped patterns in the wide-field movies:

- The AS-TDI molecules constantly reorient their transition dipole moment, similarly to the DIP-TDI molecules
- Their transition dipole moment remains in the xy plane of the wide-field setup, i.e. in the silica planes.

For SW-TDI, the fluorescence image (Fig 4b, right panel) shows a slightly striped line, indicating only a partial orientation of the dye molecules. Surprisingly, in this case the extracted angle corresponds to the direction of the mesoporous film plane (99° ± 3°). From the wide-field measurements it was expected that the doughnuts would cause an overall orientation perpendicular to the lamellas of the mesoporous film, similarly to what was observed for AS-TDI. We suggest that the different orientation observed with the confocal setup arise from the other population which is constituted by the Gaussian-shaped molecules. The only possible configuration for these SW-TDI molecules which can explain the overall orientation along the film is an alignment of their transition dipole moment parallel to the lamellas. However, a condition for such an orientation is that these molecules are brighter than those of the other population. This condition could be fulfilled if the molecules of the two populations couple differently to their direct surrounding. For example, different interactions with the template or the silica walls might provide two distinct environments for the two configurations of TDI molecules. Furthermore, at ensemble concentration inter-molecular interactions might occur between the guest molecules and influence the ratio of the two populations of diffusing molecules compared to the single molecule concentration. Hence, it is possible that much more fast diffusing Gaussian-shaped SW-TDI molecules are present at ensemble concentration resulting in a brighter fluorescence signal for this population.

Altogether, these results enable us to suggest a picture of the behaviour of the three TDI dyes in the lamellar structure, as depicted schematically in Figure 5. The DIP-TDI molecules do not keep a preferential orientation, but constantly reorient during their walk within the template filled lamellas (see Figure 5a). In this system the host-guest interactions are probably relatively weak and do not influence the orientation of the DIP-TDI molecules significantly.

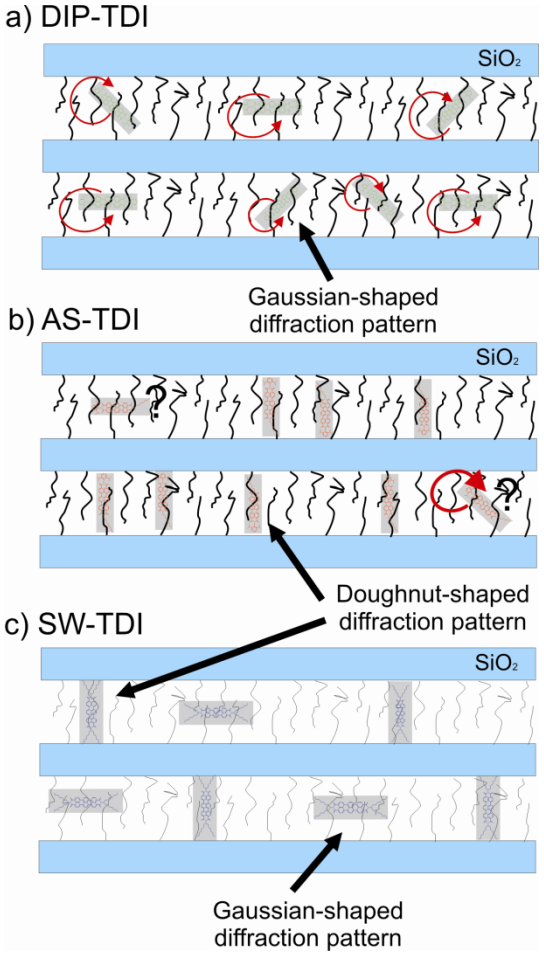

Figure 5: Schematic of the proposed orientational behaviour in the lamellar structure for the three TDI derivatives. a) The DIP-TDI molecules undergo constant reorientation of their transition dipole moment during their walk. b) For AS-TDI two populations of diffusing molecules are observed: the slow doughnuts oriented perpendicular to the silica walls, and the Gaussian-shaped pattern molecules which are either freely rotating or whose orientation lies parallel to the silica planes. c) In the case of SW-TDI two populations are also observed: the z-oriented doughnuts similarly to AS-TDI, and the Gaussian-shaped pattern molecules lying in the plane of the silica layers.

In contrast, 90 % of the AS-TDI molecules align along the template molecules due to strong interactions, and diffuse slowly in this configuration appearing as doughnuts in the wide-field movies. The other 10 %, the fast Gaussian-shaped molecules, may rotate freely, similarly to DIP-TDI. Another possibility for their transition dipole moment is to lie between the silica planes, as can be seen in Figure 5b.

Finally, the SW-TDI molecules exhibit two distinct preferential orientations with about equal ratio. The first population (the doughnuts in the wide-field movies) corresponds to molecules oriented perpendicular to the lamellas, whereas the transition dipole moment of the molecules of the second population (Gaussian-shaped patterns) remains in the lamellar planes during their walk. Strong interactions between the four alky tails of SW-TDI and the template molecules are assumed to dictate these two preferential configurations. Moreover, switches between these two populations can occur, as already mentioned. This shows that although the two populations refer to two energetically favoured orientations, the molecules are able to overcome the energetic barriers occasionally, maybe at defect sites in the silica walls or in the template of the host structure. It is also interesting to note that although SW-TDI has more alkyl chains and should align better with the template molecules than AS-TDI, the ratio of doughnuts to fast molecules is surprisingly smaller than for AS-TDI. An explanation might be that a configuration parallel to the lamellas is energetically more favourable for SW-TDI than for AS-TDI due to stronger interactions between the four alkyl chains and the template molecules. Nevertheless, other effects may also have to be considered. In the case of SW-TDI for instance, sterical hindrance due to interactions between the four long alkyl chains and the silica walls in the doughnut configuration may explain the smaller ratio of doughnuts. In summary, the presence of one or more alkyl chains in the structure of TDI has a tremendous influence on the orientational behaviour of the guest molecules.

Conclusion

Wide-field microscopy was used to investigate the dynamics of single molecules of three different TDI derivatives incorporated as guests in mesoporous silica host systems. The dye molecules are dissolved in the micelles of the template with occasional interactions with the silica walls of the pores during their walk. The diffusional behaviour in the hexagonal phase differs dramatically from unrestricted diffusion, e.g. in a liquid medium, as the motion of the single molecules is confined in the host channels. For the three TDI derivatives the highly structured trajectories reveal details about the underlying host structure like domain sizes, connectivity between the different channels, the presence of defects sites like holes in the silica wall or dead ends where the pores are closed. Moreover, dynamical information could

be obtained. The three TDI conjugates show clearly distinct mean diffusion coefficients (with $\langle D \rangle_{SW\text{-}TDI} > \langle D \rangle_{AS\text{-}TDI} > \langle D \rangle_{DIP\text{-}TDI}$) caused by the presence of different substituents in the guest molecules.

The behaviour of the TDI molecules differs dramatically in the lamellar host structure compared to the hexagonal phase. Whereas DIP-TDI exhibits only one population of diffusing molecules with Gaussian-shaped diffraction pattern, two sub-populations have been observed for AS-TDI and SW-TDI: fast diffusing molecules with Gaussian-shaped patterns and slowly diffusing molecules with doughnut-shaped patterns. For both populations, the single dye molecules diffuse in a random walk, contrasting with the highly structured trajectories in the hexagonal phase. Furthermore, information about the orientational behaviour of the different TDI molecules could be gathered. Whereas the Gaussian-shaped molecules of DIP-TDI reorient constantly during their walk in the lamellar galleries, AS-TDI and SW-TDI exhibit two different orientational behaviours. The molecules with doughnut-shaped patterns were attributed to molecules whose transition dipole moment is oriented perpendicular to the lamellas due to interactions between the alkyl chains of AS-TDI and SW-TDI with the template molecules. The faster Gaussian-shaped molecules of SW-TDI are probably oriented parallel to the lamellas, whereas in the case of AS-TDI either free rotation or an orientation of the transition dipole moment lying parallel to the silica planes are possible. Finally, transitions between the two orientational states were observed occasionally at the single molecule level. To conclude, this contribution is the first step in designing guests with adapted diffusion properties in order to gain better control over the host-guest interactions.

Acknowledgements

We thank the group of T. Bein (LMU, Munich, Germany) for providing the recipes for the synthesis of the mesoporous films and for supplying the facility for the XRD-measurements. This work was funded by the SFB 486, the SFB 749 and the Nanosystems Initiative Munich (NIM).

Dedication

With this publication we would like to honour Professor Dr. Jörg Kärger for his excellent contributions to the field of molecular diffusion over many years.

Supporting information

Movie 1: Very structured diffusion of single DIP-TDI molecules in the hexagonal phase. Image size: 35x35 µm. Time scale: 25 fps. Time resolution: 200 ms / frame. Movie 2: Very structured diffusion of single AS-TDI molecules in the hexagonal phase. Image size: 35x35 µm. Time scale: 25 fps. Time resolution: 100 ms / frame. Movie 3: Very structured diffusion of single SW-TDI molecules in the hexagonal phase. Image size: 35x35 µm. Time scale: 25 fps. Time resolution: 100 ms / frame. Movie 4: Random diffusion of single Gaussian-shaped DIP-TDI molecules in the lamellar phase. Image size: 35x35 µm. Time scale: 25 fps. Time resolution: 100 ms / frame. Movie 5: Random diffusion of single Gaussian-shaped AS-TDI molecules in the lamellar phase. Here, also very weak single molecule signals of Doughnut-shaped molecules can be observed, which seem nearly immobile with the time resolution used in this measurement. Image size: 35x35 µm. Time scale: 25 fps. Time resolution: 100 ms / frame. Movie 6: Random diffusion of single Gaussian-shaped SW-TDI molecules in the lamellar phase. Here, also very weak single molecule signals of Doughnut-shaped molecules can be observed, which seem nearly immobile with the time resolution used in this measurement. Image size: 35x35 µm. Time scale: 25 fps. Time resolution: 100 ms / frame. Movie 7: Random diffusion of single Doughnut-shaped AS-TDI molecules in the lamellar phase. Image size: 35x35 µm. Time scale: 25 fps. Time resolution: 8 s / frame. Movie 8: Random diffusion of single Doughnut-shaped SW-TDI molecules in the lamellar phase. Image size: 35x35 µm. Time scale: 25 fps. Time resolution: 8 s / frame.

References

1. M. J. Wirth, R. W. P. Fairbank, H. O. Fatunmbi, Mixed Self-Assembled Monolayers in Chemical Separations. *Science* **275**, 44 (1997).
2. M. J. Wirth, D. J. Swinton, M. D. Ludes, Adsorption and Diffusion of Single Molecules at Chromatographic Interfaces. *Journal of Physical Chemistry B* **107**, 6258 (2003).

3. M. Jaroniec, *Molecular Sieves: Science and Technology*. *Postsynthesis Modification I*. H. G. Karge, J. Weitkamp, Eds., (Springer-Verlag, Berlin, Heidelberg, New York, 2002), vol. 3.
4. H. G. Karge, H. K. Beyer, *Solid-State Ion Exchange in Microporous and Mesoporous Materials*. *Molecular Sieves - Science and Technology*. (Springer, Berlin, Heidelberg, 2002), vol. 3.
5. P. C. Pandey, S. Upadhyay, H. C. Pathak, A new glucose sensor based on encapsulated glucose oxidase within organically modified sol-gel glass. *Sensors and Actuators B: Chemical* **60**, 83 (1999).
6. R. Reisfeld, Lasers based on sol-gel technology. *Journal of Luminescence* **72-74**, 7 (1997).
7. P. Yang *et al.*, Mirrorless Lasing from Mesostructured Waveguides Patterned by Soft Lithography. *Science* **287**, 465 (2000).
8. Ö. Weiss, J. Loerke, U. Wüstefeld, F. Marlow, F. Schüth, Host-Guest Interactions and Laser Activity in AlPO4-5/Laser Dye Composites. *Journal of Solid State Chemistry* **167**, 302 (2002).
9. A. Corma, From Microporous to Mesoporous Molecular Sieve Materials and Their Use in Catalysis. *Chemical Reviews* **97**, 2373 (1997).
10. C.-Y. Lai *et al.*, A Mesoporous Silica Nanosphere-Based Carrier System with Chemically Removable CdS Nanoparticle Caps for Stimuli-Responsive Controlled Release of Neurotransmitters and Drug Molecules. *Journal of the American Chemical Society* **125**, 4451 (2003).
11. I. Roy *et al.*, Optical tracking of organically modified silica nanoparticles as DNA carriers: A nonviral, nanomedicine approach for gene delivery. *Proceedings of the National Academy of Sciences of the United States of America* **102**, 279 (2005).
12. V. Kukla *et al.*, NMR Studies of Single-File Diffusion in Unidimensional Channel Zeolites. *Science* **272**, 702 (1996).
13. O. Terasaki, Z. Liu, T. Ohsuna, H. J. Shin, R. Ryoo, Electron Microscopy Study of Novel Pt Nanowires Synthesized in the Spaces of Silica Mesoporous Materials. *Microscopy and Microanalysis* **8**, 35 (2002).
14. N. E. Benes, H. Jobic, H. Verweij, Quasi-elastic neutron scattering study of the mobility of methane in microporous silica. *Microporous and Mesoporous Materials* **43**, 147 (2001).
15. T. Basché, S. Kummer, C. Bräuchle, DIRECT SPECTROSCOPIC OBSERVATION OF QUANTUM JUMPS OF A SINGLE-MOLECULE. *Nature* **373**, 132 (1995).
16. S. Megelski *et al.*, Orientation of Fluorescent Dyes in the Nano Channels of Zeolithe L. *Journal of Physical Chemistry B* **105**, 25 (2001).
17. A. P. Bartko, R. M. Dickson, Imaging Three-Dimensional Single Molecule Orientations. *Journal of Physical Chemistry B* **103**, 11237 (1999).
18. C. Jung, C. Hellriegel, J. Michaelis, C. Bräuchle, Single Molecule Traffic in Mesoporous Materials: Translational, Orientational and Spectral Dynamics. *Advanced Materials* **19**, 956 (2007).
19. C. Seebacher *et al.*, Observation of Translational Diffusion of single Terrylenediimide Molecules in a Mesostructured Molecular Sieve. *Journal of Physical Chemistry B* **106**, 5591 (2002).
20. M. J. Saxton, K. Jacobsen, Single-Particle Tracking: Applications to membrane Dynamics. *Annual Review of Biophysics and Biomolecular Structure* **26**, 373 (1997).

21. J. Schuster, F. Cichos, C. v. Borczyskowski, Diffusion Measurements by Single-Molecule Spot Size Analysis. *Journal of Physical Chemistry A* **106**, 5403 (2002).
22. J. Kirstein *et al.*, Exploration of nanostructured channel systems with single-molecule probes. *Nature Materials* **6**, 303 (2007).
23. C. Jung *et al.*, Simultaneous measurement of orientational and spectral dynamics of single molecules in nanostructured host-guest materials. *Journal of the American Chemical Society* **129**, 5570 (2007).
24. Y. Fu, M. M. Collinson, D. A. Higgins, Single-molecule spectroscopy studies of microenvironmental acidity in silicate thin films. *Journal of the American Chemical Society* **126**, 13838 (2004).
25. Y. Fu, F. M. Ye, W. G. Sanders, M. M. Collinson, D. A. Higgins, Single molecule spectroscopy studies of diffusion in mesoporous silica thin films. *Journal of Physical Chemistry B* **110**, 9164 (2006).
26. T. Lebold *et al.*, Tuning Single-Molecule Dynamics in Functionalized Mesoporous Silica. *Chemistry - A European Journal* **15**, 1661 (2009).
27. C. J. Brinker, Y. Lu, A. Sellinger, H. Fan, Evaporation-Induced Self-Assembly: Nanostructures Made Easy. *Advanced Materials* **11**, 579 (1999).
28. D. Grosso, F. Babonneau, G. J. d. A. A. Soler-Illia, P.-A. Albouy, H. Amenitsch, Phase transformation during cubic mesostructured silica film formation. *Chemical Communications*, 748 (2002).
29. C. Hellriegel, J. Kirstein, C. Bräuchle, Tracking of single molecules as a powerful method to characterize diffusivity of organic species in mesoporous materials. *New Journal of Physics* **7**, 23 (2005).
30. C. Jung *et al.*, Diffusion of oriented single molecules with switchable mobility in networks of long unidimensional nanochannels. *Journal of the American Chemical Society* **130**, 1638 (2008).
31. A. Zürner, J. Kirstein, M. Döblinger, C. Bräuchle, T. Bein, Visualizing single-molecule diffusion in mesoporous materials. *Nature* **450**, 705 (2007).
32. R. Bandyopadhyaya, E. Nativ-Roth, R. Yerushalmi-Rozen, O. Regev, Transferable thin films of mesoporous silica. *Chemistry of Materials* **15**, 3619 (2003).
33. M. Matheron *et al.*, Highly ordered CTAB-templated organosilicate films. *Journal of Materials Chemistry* **15**, 4741 (2005).
34. M. J. Wirth, M. Ludes, D. Swinton, D. J., Spectroscopic Observation of Adsorption to Active Silanols. *Analytical Chemistry* **71**, 3911 (1999).
35. The presence of the Gaussian-shaped AS-TDI molecules in the pure lamellar phase was overlooked in our previous publication[22] because of their small ratio compared to the doughnuts and the difficulty to distinguish them from molecules at the surface of the mesoporous films. Here, an additional experiment based on polymer coating clearly allowed a distinct differenciation (data not shown).

5 Studies of plasmonic coupling with single particle resolution

5.1 Plasmon enhancement and quenching of single dye molecules and quantum dots diffusing in mesoporous silica channels on silver island films

The field of plasmonics has recently emerged to a prominent topic in nanotechnology[1-3] due to the unique interactions of the density waves of electrons, the so-called plasmon, with light. Light is an excellent carrier for information, which is widely used in optical data transfer via fiber optic cables. Thereby, high bandwidths can be achieved and photonic devices might replace electronic circuits in computer chips in the future. However, due to interference caused by nearby light waves, the width of an optical fiber must be at least half of the wavelength and thus bulky wires are required. In contrast electronic data transfer is transmitted via very small wires, but is limited to inferior frequencies. Plasmonics combines the advantages of both optical and electronic data transfer by transmission of data at optical frequencies along the surface of a nano-sized metal wire. Thereby, the data is transferred as electron density distributions rather than photons or electrons. Apart from this highly desired application, plasmonics has already been successfully utilized in several other approaches, such as gas or bio-molecular sensors,[4, 5] full color holograms[6] and coupling to luminescent particles, such as dye molecules,[7-9] quantum dots[10, 11] or metal nano-particles.[12] In order to develop customized plasmonic systems for possible applications, a thorough understanding of the plasmonic properties is essential. In this investigation a well defined system was conceived to study plasmon coupling of organic TDI dyes and quantum dots diffusing in mesoporous thin films to nano-structured silver-island films on a single molecule basis. This plasmon coupling can influence, e.g. enhance, the fluorescence emission of the single fluorophores. Silver-island films (SIF) have been demonstrated to enhance the fluorescence emission of light harvesting complexes immobilized in a polymer layer.[13] In order to study the effect of the relative distance between the fluorophore and the silver nano-structure on the fluorescence emission, mesoporous thin films, which constitute a versatile host system for the diffusion of guest molecules as shown in previous studies,[14, 15]

were prepared on SIFs. A schematic illustration of the sample system investigated in this study is shown in Figure 1. As the distance dependence of plasmon coupling is usually strongest in the range of up to 20 nm, mesoporous films of only about 20 nm thickness were synthesized to minimize the amount of uncoupled fluorophores.

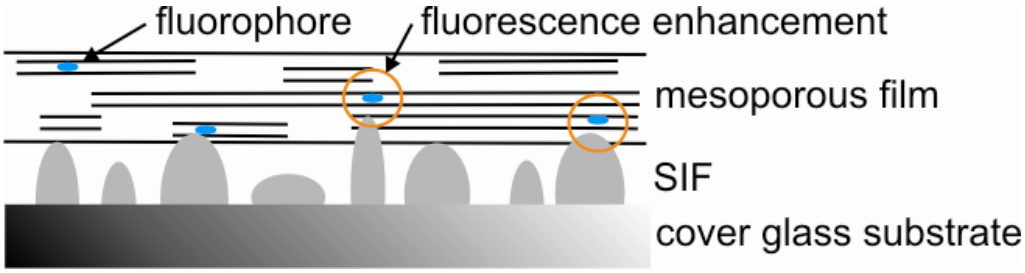

Figure 1: Scheme of the sample system. The mesoporous film is deposited on top of the SIF. Organic TDI dye molecules or quantum dots diffusing within the mesopores can interact with the plasmon of the SIF leading to fluorescence enhancement or quenching.

Experimental section

Preparation of SIFs

Silver nitrate (0.375 g, 0.0022 moL) was dissolved in 45 mL deionized water in a beaker. The solution was stirred on a Rotamax 120 (Heidolph) and 1.5 mL of a 5% (w/v) sodium hydroxide solution was added. The resulting grey-brown precipitate of silver hydroxide was dissolved slowly upon the addition of 1 mL ammonium hydroxide solution and a colorless, cationic complex $[Ag(NH_3)_2]^+$ was obtained (solution 1). The prepared solution was cooled at 0°C for several minutes. In a second beaker D-glucose (0.540 g, 0.0030 mmoL) and 11 mL deionized water were mixed and the solution was also cooled at 0°C (solution 2). For the preparation of the SIF, a cover glass was placed into a culture dish and 2.5 mL of the cooled solution 1 and 0.5 mL of solution 2 were added. Next, the sample was stirred on a Rotamax 120 at 100 rpm. A color change of the reaction mixture could be observed from yellowish to greenish and finally to silver after about 4 minutes. The reaction was interrupted by washing the cover glass with deionized water to prevent the forming silver film from growing too thick. This is vital as the high reflectivity of a thick silver mirror would hinder excitation light passing through the sample. The prepared SIFs were stored in deionized water to protect them against dust and oxidation.

Preparation of ultra-thin mesoporous films

Mesoporous films were prepared similar to the procedure described in chapter 4.2 for hexagonal films. However, sample solutions were diluted with ethanol in order to obtain ultra-thin hexagonal mesoporous films. In the following, samples of the dilution series will be referred to Brij-Hex-1 (undiluted), Brij-Hex-2 (precursor solution to ethanol 2:1), Brij-Hex-3 (1:1), Brij-Hex-4 (1:2) and Brij-Hex-5 (1:4). Next, 80 µl of these solutions including the desired fluorophore (TDI dyes or quantum dots) were spin-coated on a cover glass at 3000 rpm for 30 s using a SCS P6700 (Speedline Technologies).

Wide-field microscopy

Fluorescence images were recorded with the wide-field setup described in detail in chapter 2.4.2. The TDI dyes were excited at 633 nm with a He-Ne gas laser (Coherent) with an intensity of 0.2 kW cm^{-2}. The quantum dots (kindly provided by Prof. A. Rogach, LMU Munich) were excited at 532 nm with a diode pumped solid-state laser (Cobolt Samba TM Laser) with an intensity of 0.1 kW cm^{-2}. Band-pass filters 730/140 and 585/70 (AHF Analysentechnik) were used to block incident laser light for excitation at 633 nm and 532 nm, respectively.

Sample characterization

The thickness of the SIFs and of the mesoporous films was obtained by ellipsometry using a Woollam ESM-300 Ellipsometer. Silicon wavers were used as substrate for all samples prepared for ellipsometry measurements. The experimental data could be well approximated with calculated values (Figure 2). The calculated values for the thickness of a single SIF, an ultra-thin mesoporous film and an ultra-thin mesoporous film on top of a SIF are given in Table 1. Both the SIFs and the ultra-thin mesoporous films are about 15-20 nm in thickness.

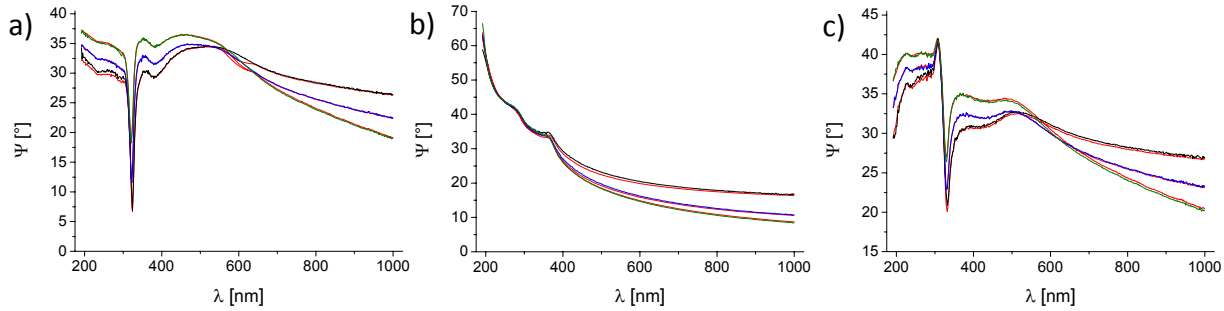

Figure 2: Experimental data and calculated fit of ellipsometry measurements of a) a single SIF, b) an ultra-thin mesoporous films and c) an ultra-thin mesoporous film on top of a SIF. Silicon wavers were used as substrate for all film coatings. Fit (red) and measurements at Ψ values of 65° (black), 70° (blue) and 75° (green).

Table 1: Determined thicknesses of respective film coatings on silicon wavers using ellipsometry measurements.

sample / layer	SIF	Ultra-thin mesoporous film	Ultra-thin mesoporous film on top of a SIF
Ag	19.584 nm	--	18.683 nm
mesoporous film	--	20.287 nm	14.960 nm
SiO_2	3.000 nm	3.000 nm	3.000 nm
Si	1.000 mm	1.000 mm	1.000 mm

The surface of the SIFs was scanned by atomic force microscopy (AFM) showing a rough, granular shape reflecting the island structure of the silver films (Figure 3a). By applying a scratch to a mesoporous ultra-thin film on top of a SIF (Figure 3b) and subsequent scanning by AFM provided a combined thickness of about 35 nm (Figure 3c). This value is consistent with the respective result of the ellipsometry measurement.

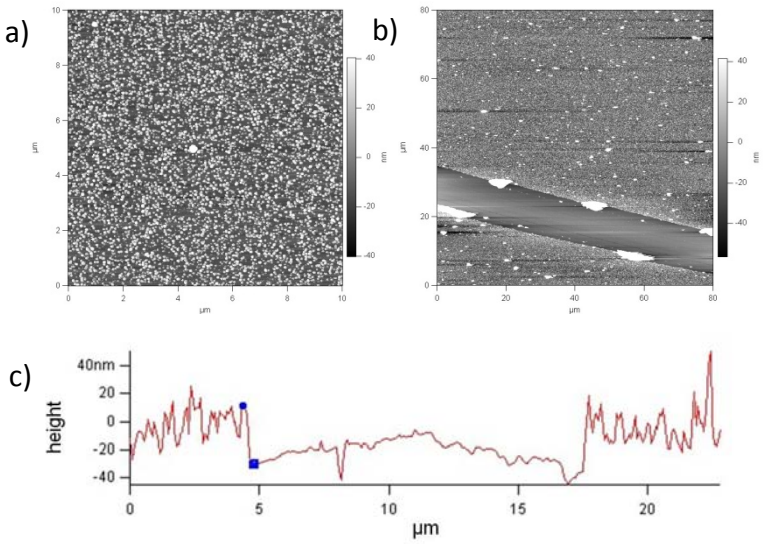

Figure 3: Images taken using AFM. a) SIF and b) ultra-thin mesoporous film on top of a SIF. The dimension of the scratch visible in b) was measured by AFM and is shown in c). The thickness of the combined mesoporous film and SIF amounts to about 35 nm, which is in good agreement with the result of the ellipsometry measurement.

The structure of the mesoporous films was determined by X-ray diffractometry (XRD) using a Scintag XDS 2000 diffractometer in Bragg-Bretano geometry. The sharp peaks of the diffraction data in Figure 4 indicate that the 200 nm thick mesoporous films and also thinner films are well structured and hexagonal. As described in the previous chapter, the 2θ values of the peaks can be used to calculate the average pore-to-pore distance *a* and the layer-to-layer distance *d*. Similar to the previous results, the hexagonal mesopores exhibit values of about 2θ = 1.6 ° and thus *a* = 6.3 ± 0.1 nm and *d* = 5.5 ± 0.1 nm. Going from 200 nm thick films to thinner mesoporous films results in the appearance of additional peaks of higher order as shown in Figure 4.

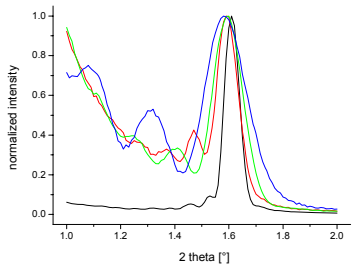

Figure 4: X-ray diffractograms of thin hexagonal mesoporous films on top of a SIF. Brij-Hex-1 (black), Brij-Hex-2 (red), Brij-Hex-3 (green) and Brij-Hex-4 (blue). For thinner films additional peaks of higher order can be observed.

Results

Single molecule fluorescence microscopy and single particle tracking (SPT) were employed to analyze the translational diffusion of the single fluorophores similar to studies presented previously in chapter 4.2. The trajectories of organic TDI (AS-, DIP- and SW-TDI) dyes in 200 nm thick mesoporous film exhibit well structured shapes in the low micrometer regime as shown in chapter 4.2. Repeating analogue measurements with these guest molecules in the ultra-thin 20 nm mesoporous films provides still structured trajectories, however, the overall domain size is smaller on average and the mesopores seem slightly less well structured (Figure 5).

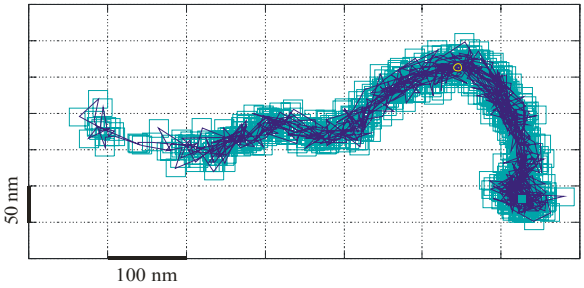

Figure 5: Exemplary single molecule trajectory of the AS-TDI dye in the mesoporous channels of a 20 nm thick film. The experimentally determined positioning accuracy for each observed position of a molecule is given by box-error bars.

In contrast to the previous study on mesoporous films in chapter 4.2, the fluorescence intensity of the single fluorophores investigated here changes dramatically during the diffusion along the mesoporous channels deposited on top of the SIF. An example is shown in Figure 6. The fluorescence of the TDI molecule is obviously enhanced or quenched when coupled to the plasmon of the silver nanostructure.

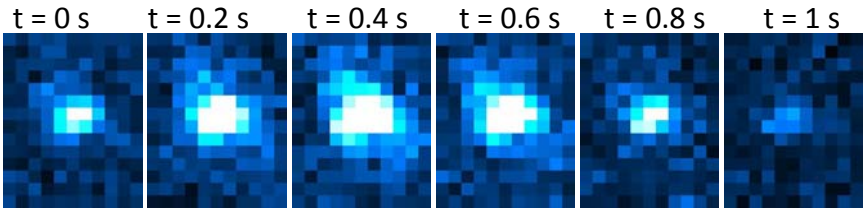

Figure 6: Images sequence of one single dye molecule diffusing in an ultra-thin mesoporous film. The fluorescence intensity of the dye molecule gets enhanced due to coupling to the SIF.

Hence the question arises, whether fluorescence enhancement and quenching by the plasmon is dependent on the specific position of the fluorophores in relation to the silver nanostructures or not. Therefore, the two-dimensional translational trajectories provided by SPT can be correlated to the respective fluorescence intensities of the fluorophores at each determined position in every single image taken. Consequently this yields a three-dimensional trajectory consisting of the spatial position versus intensity as shown in Figure 7. This three-dimensional trajectory exhibits a quite linear shape for the spatial extent, however, the fluorescence intensity of the single dye molecule increases significantly while moving from the left end to the right and vice versa. While the minimal intensity of the TDI dye molecule in Figure 8 is similar to typical fluorescence intensities of single TDI dyes in mesoporous films without SIF, the intensity maximum is about 10-fold enhanced here due to interaction with the silver nanostructure. As this behavior is observed multiple times, it can be concluded that these interactions leading to fluorescence enhancement occur at defined locations. These locations correspond most likely to positions, where the distance between the dye molecules and the metal nanostructure is minimal, i.e. close to silver islands, but not so close that quenching of the fluorophores occurs.

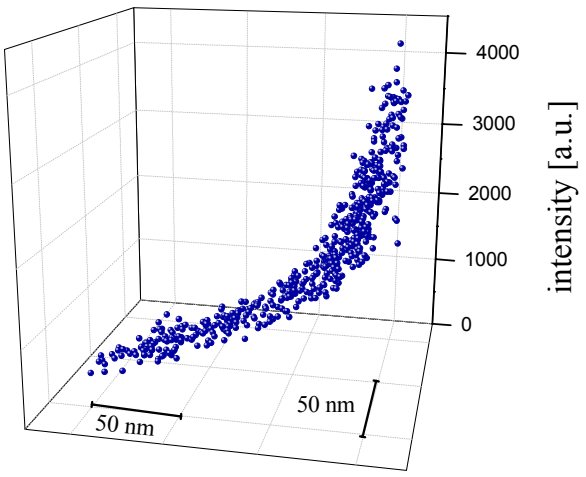

Figure 7: Exemplary plot of the two-dimensional spatial x- and y- position versus the respective fluorescence intensity of a single AS-TDI dye molecule. The emission is clearly enhanced (about 10-fold) close to one specific spatial location.

In summary, the organic TDI dyes incorporated and diffusing in ultra-thin mesoporous films on top of SIFs showed significantly increased fluorescence emission close to specific locations, which most likely correspond to the silver islands. Although the TDI dyes exhibit excellent photostability, they do still undergo photobleaching. To overcome this limitation and increase the survival time of the fluorophores in order to achieve longer observation times, CdSe quantum dots were chosen as fluorophores in replacement for the organic TDI dyes. Such semiconductor quantum dots have the advantage of significantly increased survival times of about two orders of magnitude compared to common organic dyes. The composition, size and shape of the used quantum dots (QD) are shown in Figure 8. QD 2, 3 and 4 posses protective shells to prevent degradation of the quantum dots for example by oxidation.

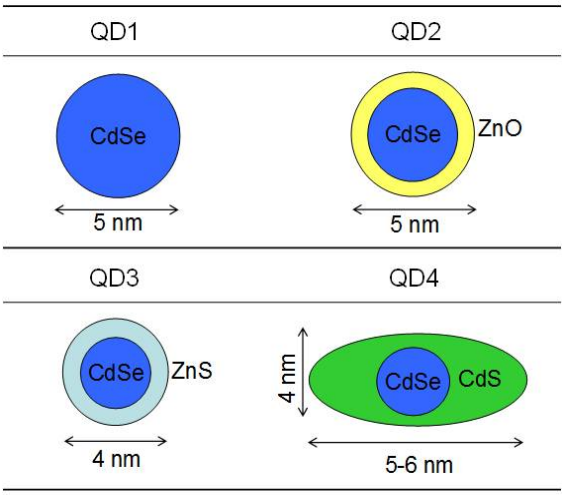

Figure 8: Schematic figure of the four different Cd-Se quantum dots and their respective sizes.

As the diffusion of quantum dots in mesoporous systems has not been investigated so far, initial pre-measurements using QD 1-4 in similar mesoporous films and under analogue conditions as described for the TDI dyes were performed. Similar to the TDI dyes, single QD 3 and 4 exhibit highly structured trajectories with domain sizes in the low micrometer regime in 200 nm thick mesoporous films (Figure 9a) and slightly less well structured trajectories in 20 nm thick mesoporous films (Figure 9b). Therefore, QD 3 with a diameter of 4 nm and QD 4 with an ellipsoid shape and a minor axis of 4 nm obviously fit quite well into the silica mesopores with pore sizes of about 4-6 nm. In contrast, QD 1 and 2 are mostly immobile in

the mesoporous structure and only show unstructured diffusion, which can be attributed to motion within defect regions within the structure. Therefore, both spherical quantum dots with diameters of 5 nm (QD 1 and 2) are too large to move in the mesoporous channels.

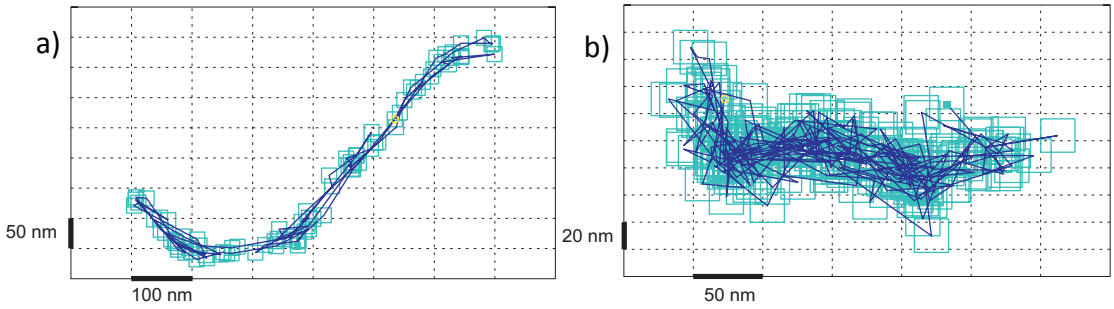

Figure 9: Exemplary trajectories of QD 4 inside a mesoporous film with a thickness of a) 200 nm and b) 20 nm. The experimentally determined positioning accuracy for each observed position of the quantum dot is given by box-error bars.

The two-dimensional spatial trajectories of single QD 3 and 4 were plotted versus the emitted fluorescence intensities similar to the data shown for TDI previously. An example for QD 4 is depicted in Figure 10. The emission of the single quantum dot is about 17-fold enhanced close to a specific location due to coupling with the silver islands.

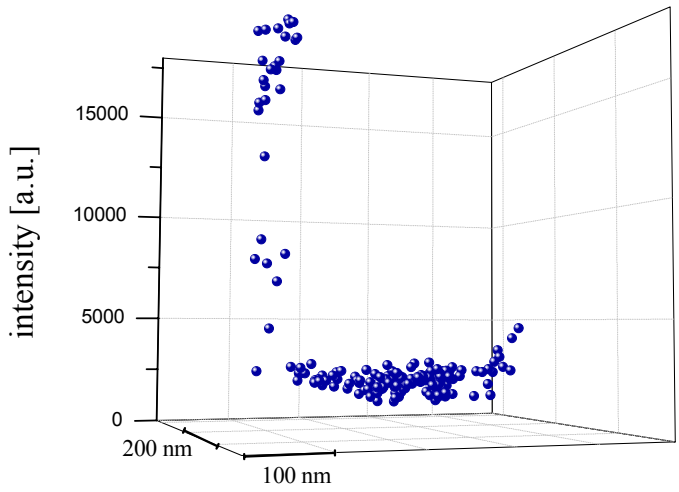

Figure 10: The two-dimensional spatial trajectory of a single QD 4 is plotted versus the respective fluorescence intensity. Emission enhancement (about 17-fold) occurs close to one specific spatial location of the trajectory.

In conclusion, this study is devoted to the manipulation of the fluorescence emission of organic TDI dyes and quantum dots diffusing in mesoporous thin films via plasmon coupling to silver-island films. The correlation of the spatial trajectories of the fluorophores with the respective fluorescence intensities revealed that TDI dye molecules as well as quantum dots can couple to the plasmon of the silver nanostructure leading to fluorescence enhancement of about one order of magnitude. The results provided in this investigation can serve as a platform for more sophisticated approaches towards customized nano-scaled systems utilizing plasmon enhancement in the future.

References

1. W. L. Barnes, A. Dereux, T. W. Ebbesen, Surface plasmon subwavelength optics. *Nature* **424**, 824 (2003).
2. E. Ozbay, Plasmonics: Merging photonics and electronics at nanoscale dimensions. *Science* **311**, 189 (2006).
3. R. Kolesov *et al.*, Wave-particle duality of single surface plasmon polaritons. *Nature Physics* **5**, 470 (2009).
4. B. J. Murray, Q. Li, J. T. Newberg, J. C. Hemminger, R. M. Penner, Silver oxide microwires: Electrodeposition and observation of reversible resistance modulation upon exposure to ammonia vapor. *Chemistry of Materials* **17**, 6611 (2005).
5. S. E. Brunker, K. B. Cederquist, C. D. Keating, Metallic barcodes for multiplexed bioassays. *Nanomedicine* **2**, 695 (2007).
6. M. Ozaki, J. Kato, S. Kawata, Surface-Plasmon Holography with White-Light Illumination. *Science* **332**, 218 (2011).
7. S. L. Pan, L. J. Rothberg, Enhancement of platinum octaethyl porphyrin phosphorescence near nanotextured silver surfaces. *Journal of the American Chemical Society* **127**, 6087 (2005).
8. S. L. Pan, Z. J. Wang, L. J. Rothberg, Enhancement of adsorbed dye monolayer fluorescence by a silver nanoparticle overlayer. *Journal of Physical Chemistry B* **110**, 17383 (2006).
9. S. H. Guo, D. G. Britti, J. J. Heetderks, H. C. Kan, R. J. Phaneuf, Spacer Layer Effect in Fluorescence Enhancement from Silver Nanowires over a Silver Film; Switching of Optimum Polarization. *Nano Letters* **9**, 2666 (2009).
10. A. V. Akimov *et al.*, Generation of single optical plasmons in metallic nanowires coupled to quantum dots. *Nature* **450**, 402 (2007).
11. C. Grillet *et al.*, Nanowire coupling to photonic crystal nanocavities for single photon sources. *Optics Express* **15**, 1267 (2007).
12. Z. Y. Fang *et al.*, Plasmonic Coupling of Bow Tie Antennas with Ag Nanowire. *Nano Letters* **11**, 1676 (2011).
13. S. Mackowski *et al.*, Metal-enhanced fluorescence of chlorophylls in single light-harvesting complexes. *Nano Letters* **8**, 558 (2008).

14. F. Feil *et al.*, Diffusional and orientational dynamics of various single terylene diimide conjugates in mesoporous materials. *Microporous and Mesoporous Materials* **125**, 70 (2009).
15. J. Kirstein *et al.*, Exploration of nanostructured channel systems with single-molecule probes. *Nature Materials* **6**, 303 (2007).

5.2 Synchronous emission from nanometric silver particles through plasmonic coupling on silver nano-wires

M. Davies*, A. Wochnik*, F. Feil*, C. Jung, C. Bräuchle, C. Scheu, J. Michaelis, Synchronous emission from nanometric silver particles through plasmonic coupling on silver nano-wires. *ACS Nano*, submitted.

[∗] These authors contributed equally to this work.

Author contributions

F.F. performed the single molecule experiments, conceived the analysis routine, analyzed the single molecule data and performed the statistical investigation of the distribution of the distances of the cooperative effect. M.D. also performed the single molecule experiments and additionally performed the single molecule part of the overlay of fluorescence images and TEM and analyzed the corresponding data. A.W. performed the TEM and EDX measurements and analyzed the TEM and EDX data.

We investigated silver nano-wires using correlative wide-field fluorescence- and transmission electron microscopy. In the wide-field fluorescence images synchronous emission from different distinct positions along the silver nano-wires was observed. The sites of emission were separated spatially by up to several micrometers. Nano-wires emitting in such cooperative manner were then also investigated with a combination of transmission electron microscopy based techniques, e.g. high-resolution, bright field imaging, electron diffraction, high angle angular dark field imaging and energy dispersive X-ray spectroscopy. In particular, analyzing the chemical composition of the emissive areas using energy dispersive X-ray spectroscopy, led to the model that the emissive centers are small silver clusters generated photochemically and that individual clusters are coupled via surface plasmons of the nano-wire.

In recent years there has been a growing interest in the synthesis and control of nano-structures of (noble) metal assemblies. Their unique optical properties caused by the collective oscillation of free electrons, known as plasmon resonances, are a central subject of most recent research.[1-3] In particular, silver is known for exhibiting plasmon resonances for

particle sizes in the nanometer regime. Also the shape of the metal, such as the aspect ratio of silver nano-wires, has a tremendous influence on the plasmonic properties.[4] Consequently, a thorough understanding of these properties is essential for the development of customized plasmonic systems for nanotechnology applications. Such potential utilizations include surface-enhanced Raman scattering (SERS),[5-8] plasmon wave-guiding,[9-13] gas or bio-molecular sensors[14, 15] and coupling to luminescent particles, such as dye molecules,[16-18] quantum dots[19, 20] or metal nano-particles.[21] Despite the extensive efforts put into the investigation of synthesis conditions of metal nano-particles, such as silver nano-wires (Ag-NW), and their plasmonic properties for spectroscopic enhancement, only few studies on their luminescence after photo-activation exist as high detection sensitivity is required.[22, 23]

Uniform silver-nano-wires are usually synthesized by templating methods using either hard templates, such as porous alumina,[24] or soft templates, including cetyltrimethyl-ammonium bromide (CTAB),[25] polyvinylpyrrolidone (PVP)[26, 27] or trisodium citrate.[28] It is known that small defects in the nano-wire as well as the presence of silver nano-particles in the close vicinity of the nano-wire can have tremendous influence on their emission properties. One important example is the photo-chemical formation of silver nano-cluster in such defects, which form local emitting entities. The formation of such entities has recently been described.[29-32] First, pure silver is oxidized, followed by the generation of small silver-clusters within the silver oxide layer caused by irradiation with a laser beam.

Important insight into the emission characteristics of metal nano-particles can be obtained by single molecule spectroscopy (SMS) experiments, where a single particle or molecule is observed continuously over a long time interval, providing a direct view on the heterogeneity of molecular behavior.[33-36] With SMS subpopulations, rare events and the influence of structural heterogeneous environment on the different single particles can be revealed. However, detailed structural analysis of the nano-wires and nano-clusters is hindered due to the limited spatial resolution.

Here, we investigated silver nano-wires using a combination of SMS and transmission electron microscopy (TEM) including analytical techniques. Using wide-field illumination we observed synchronous fluorescence emission from emitters located at distinct positions

along single nano-wires. By correlating fluorescence, high resolution TEM and energy dispersive X-ray spectroscopy we were able to attribute the cooperative behavior to spectroscopic features of the silver nano-wires.

Results and Discussion

Single crystalline silvers nano-wires, synthesized by a seedless wet-chemical approach (Methods), were imaged using bright field electron microscopy (Materials and Methods). The image of an exemplary silver nano-wire (Ag-NW) in Figure 1a shows an around 11 µm long and 80 nm thick Ag-NW deposited on a holey coated carbon copper grid. As can be seen, the nano-wire has a rather homogeneous thickness over the entire length.

Higher magnification images and diffraction studies revealed more detailed information of the Ag-NWs structure. Figure 1b shows a higher magnification bright field image of a selected region of this Ag-NW (indicated by red square in Figure 1a). An about 10-20 nm thick layer surrounding the Ag-NW can be observed which is attributed to the sodium citrate used for the growth and stabilization of the Ag-NWs during their synthesis (Materials and Methods). Additionally, particles of about 5-10 nm in size can be seen in this citrate layer. The electron diffraction pattern (Figure 1b inset) taken in the middle of the Ag-NW from Figure 1b displays spots corresponding to Ag reflections. In addition, reflections due to twinning, i.e. two or more separate crystals sharing some of the same crystal lattice points in a symmetrical manner, of the Ag-NW occur in accordance to the observations reported in literature where fivefold twinning is frequently observed for Ag-NWs and nano-particles.[37, 38] Moreover, diffraction experiments and fast Fourier transformation (FFT) analysis of high resolution TEM (HRTEM) micrographs analysis taken at various positions along the surface of the Ag-NW and of particles in the citrate layer showed additional weaker reflections attributed to silver oxide. Hence, the particles in the citrate layers are primarily pure Ag-particles, and only some of them are composed of silver oxide.

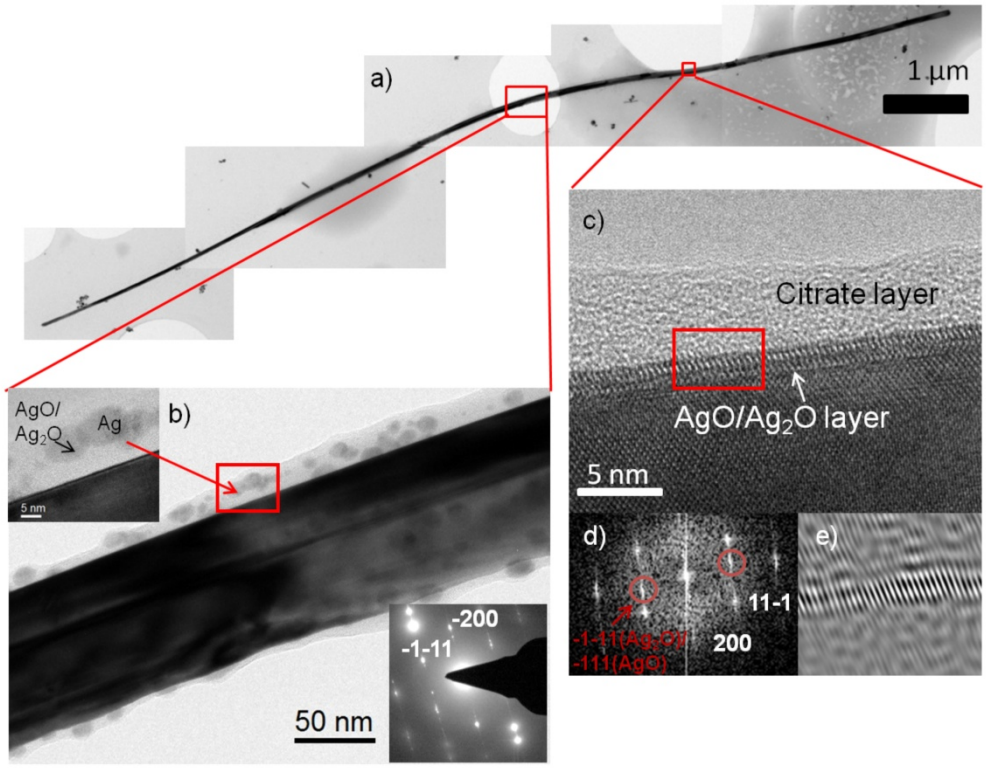

Figure 1: a) Bright field TEM image of an exemplary silver nano-wire with dimension of about 11 µm length and 80 nm thickness. The red squares indicate specific areas that were then imaged at higher magnifications. b) Higher magnified TEM image of a selected area showing an about 10-20 nm thick layer surrounding the Ag-NW, which was attributed to citrate. The inset in the upper left shows the Ag-NW surface at even higher magnification. In the citrate layer particles of about 5-10 nm can be observed, which are attributed to AgO, Ag_2O or Ag. The recorded electron diffraction pattern of the Ag-NW indicates the presences of pure Ag (second inset). c) High resolution image of a specific region from a) showing the citrate layer surrounding the Ag-NW and an additionally 2-3 thick layer on the interface between NW and citrate layer. d) The fast Fourier tranformation of the marked area (red) in Figure 1c shows an [011] orientation of the nano-wire and indicates reflections corresponding to the *d*-values of Ag. One additional set of reflections (marked red) was found, which matches to the (-1-11) plane of Ag_2O or (-111) of AgO. e) The inverse fast Fourier transformation (FFT) of this additional set of reflections (marked red in Figure 1d) indicates that it can be assigned to the surface layer.

When imaged at a higher magnification, an additional, about 1 nm thick layer is observed at the interface between NW and citrate layer, consisting of 2-3 atomic layers (Figure 1c). The FFT of the marked area (red) from Figure 1c indicates reflections corresponding to the *d*-values of Ag and shows the same orientation as the nano-wire in [011] (Figure 1d). Furthermore, one additional set of reflections was found (marked red in Figure 1d), which either corresponds to the (-1-11) plane of Ag_2O or to the (-111) of AgO. By comparing the inverse FFT of these reflections to the original image, it becomes clear, that these reflections stem from the surface layer (Figure 1e). Thus, the Ag-NWs possess a thin silver oxide layer, in accordance with data from additional diffraction experiments and FFT analysis (data not shown).

In order to unravel the optical properties of the Ag-NWs the luminescence of individual NWs was investigated using a wide-field optical microscope with single molecule fluorescence sensitivity (Materials and Methods). Typically each NW had several localized spots from where luminescence emission occurred. Single particle tracking (SPT) was used to determine the positions of these emitting entities on the silver nano-wires by fitting, frame-by-frame, a two-dimensional Gaussian function to the fluorescence spots:

$$I = A_0 \exp\left(-\frac{(x-x_0)^2}{2\sigma^2}\right) \exp\left(-\frac{(y-y_0)^2}{2\sigma^2}\right) \quad (1)$$

where A_0 and σ^2 are the amplitude and the variance of the two-dimensional Gaussian curve, and x_0 and y_0 the coordinates of the position of the individual emitting entities. With this method the positions of the entities can be determined with a positioning accuracy of up to 5 nm (on glass substrates) depending on the signal-to-noise ratio. Changes in the brightness of the emitting entities, background fluorescence or other emitters nearby can decrease the signal-to-noise ratio and thereby the positioning accuracy. For experiments requiring an overlay of TEM and fluorescence images, a Si_3N_4-membrane was used as a substrate (Materials and Methods). This resulted in a reduced signal-to-noise ratio and thus a lower positioning accuracy (typically about 20-25 nm) as compared to experiments on glass substrates, which were only used for fluorescence measurements.

The fluorescence from the spots was not continuous, but blinking and changes in fluorescence intensity was observed (Figure 2). This effect has been reported previously using confocal microscopy[23] and was attributed to random surface diffusion and agglomeration of Ag atoms which form photoactive Ag nano-clusters[39] or photo-activated silver oxide.[22] Interestingly, using the wide-field excitation we find that oftentimes the emission from several spots on a single NW is highly cooperative, i.e. blinking and intensity fluctuations are observed exactly at the same time, given our time-resolution of 10 ms. As an example of the cooperative effect, Figure 2 displays three consecutive frames extracted from a sequence of images (Movie S1 in Supporting Information) showing the synchronous appearance and disappearance of two spatially separated fluorescence spots along a single Ag-NW (the approximate shape of the nano-wire as observed using bright field microscopy (data not shown) is indicated by the yellow striped line). The fluorescence patterns of the spots were fitted with two-dimensional Gaussian functions (equation 1). The two centers of emission (marked by arrows in Figures 2a and b) were separated by a distance of about 1.5 µm. The recorded trajectories of the fluorescence intensity of both emitters show repetitive correlated blinking events (Figure 2c). The time at which emission occurs, appears to be stochastic, but the fluorescence emission from both emitters is perfectly synchronized (as indicated by the grey doted lines). Additionally, a statistical analysis of 120 distances between pairs of synchronous emitters was performed. The distribution of these distances (Figure S2 in the Supporting Information) is continuous and decays with longer distances. This observation can be explained by the exponential decay of the intensity of surface plasmons along metal surfaces. This plasmon damping is caused by power loss in the metal. Moreover, while the exemplary trace from Figure 2 shows rather long on-times, oftentimes observed on-times were below our time resolution of 10 ms, i.e. we observed only a single "on-frame". Interestingly, we never observed such a cooperative effect with freshly prepared Ag-NW, but only after an aging time of the nano-wires under air atmosphere of at least one day after preparation. This indicates that the presence of silver oxide may be required for the occurrence of the observed cooperative emission.

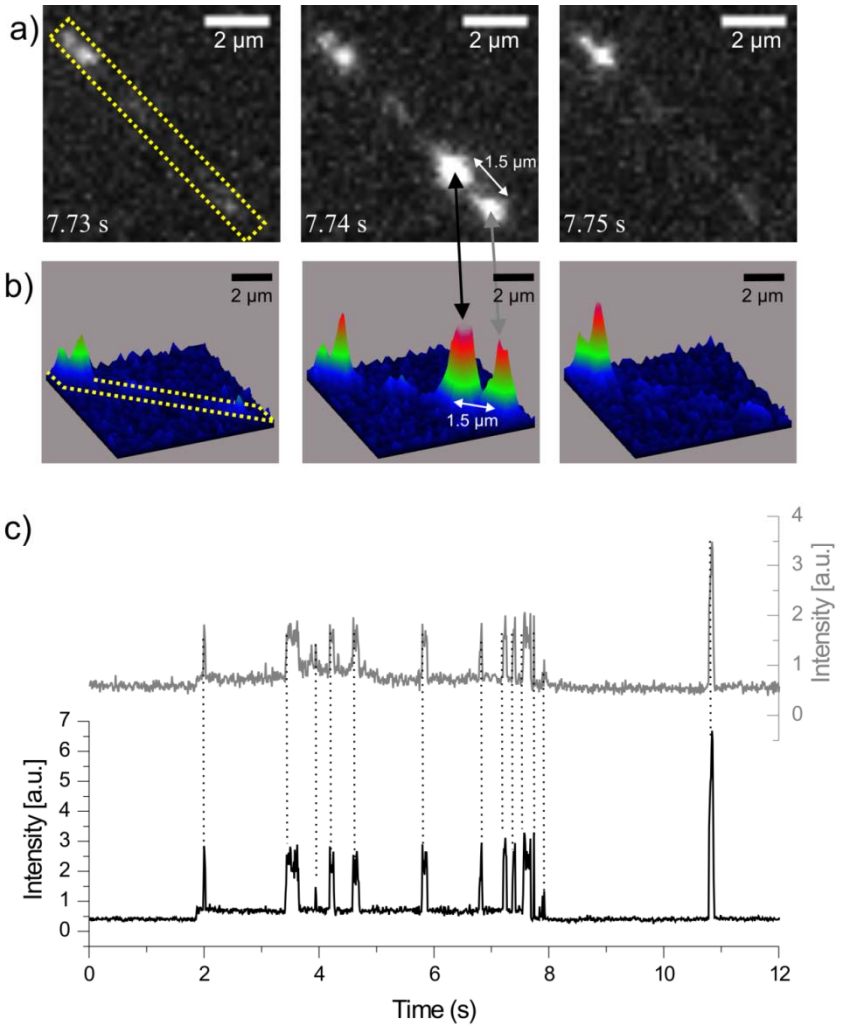

Figure 2: Wide-field fluorescence study of a Ag-NW. a) Series of wide-field images of emitting entities exhibiting a cooperative fluorescence emission. The positions of the emitters are marked with a black and grey arrow in the middle panel. b) Corresponding 3D surface plots of the fluorescence intensity. c) Fluorescence intensity trajectories over time for both emitters (gray and black lines matching the color of the respective arrows in a)). Exemplary synchronous emission events are highlighted by dashed lines.

To unravel structural and chemical reasons for the occurrence of the cooperative effect, we imaged a nano-wire by TEM, for which the cooperative effect was observed in the wide-field fluorescence measurements. The TEM image (Figure 3a) shows an about 1.38 µm long and 80 nm thick Ag-NW surrounded by several small particles. The NW and the nano-particles were characterized with energy dispersive X-ray spectroscopy (EDX) measurements in

scanning transmission electron microscopy (STEM) mode in detail to correlate optical and chemical properties (Supporting Table S1).

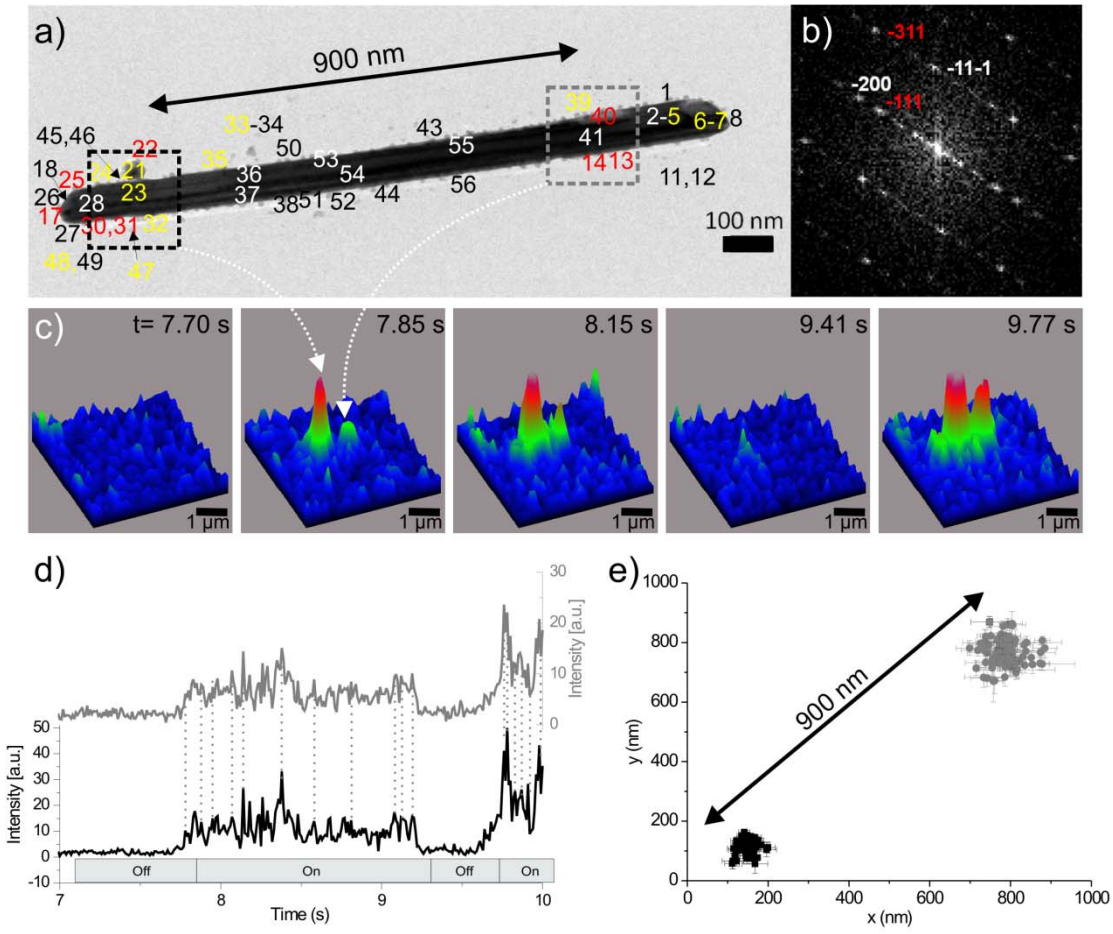

Figure 3: a) Bright field TEM image of an Ag-NW, showing cooperative fluorescence emission. The position investigated by EDX measurements (data shown in Supporting Information Table S1) are marked with numbers (black/ white numbers show high Ag values, red numbers contain beside Ag high O values; yellow numbers contain beside Ag high S values). b) The FFT taken from a part of the surface indicates reflection of Ag (marked white) and Ag_2O (marked red) and shows an orientation in [001]. c) Snapshots of the fluorescence intensity distribution emitted from the same NW displayed by 3D surface plots. The cooperative emission from two spots is marked by arrows. d) Fluorescence time trajectories of both emitters showing interesting fluctuations of the cooperative effect (marked with dashed lines). e) Determined positions with corresponding error bars (on average 15 nm (black) and 32 nm (grey)) for both emitters.

To find out which parts of the nano-wire cause the emission, approximately 50 EDX measurements were performed at different parts of the nano-wire and surrounding nano-particles using an electron beam size of about 1 nm. Figure 3a shows the bright field image of the Ag-NW together with numbers indicating the positions of the EDX measurements. The values of the quantification of the EDX spectra are given in Table S1 (Supporting Information). Besides Ag which was detected at all positions along the nano-wire, also O (red numbers) and some traces of S (yellow numbers) were found. The O stems most likely from the thin surface layer described above. The FFT taken from a part of the surface of the Ag-NW (Figure 3b) shows reflections of Ag (reflections marked in white) and silver oxide (reflections marked in red). Both, the diffraction as well as the FFT data show that most of the particles investigated by EDX contain mainly Ag, some have a high O content supporting the presence of silver oxide (e.g. positions 13, 14, 17, 42, 22, 25, 30 and 31). In addition, S, probably originating from air, is detected in parts of the citrate film and in some of the nano-particles (EDX measurements 5, 6, 7, 14, 21-25, 32, 33, 35, 39, 40, 47 and 48).

The 3D surface plots of the fluorescence intensity (Figure 3c) for five frames extracted from a wide-field fluorescence movie (Movie S2 in the Supporting Information) show the coupling of the fluorescence emission between two entities along the nano-wire (as imaged by TEM). The corresponding fluorescence intensity time trajectories are depicted in Figure 3d (grey and black curves corresponding to the left and right fluorescent spot, respectively). Both appear simultaneously (i.e. within less than 10 ms, the experimental time resolution) at about 7.8 s and disappear simultaneously at about 9.2 s. In between, strong fluorescence intensity fluctuations are detected which also appear to be synchronized, as highlighted by the dotted line between exemplary simultaneous fluorescence burst events. After 9.6 s the signals appear again before the measurement stops. For each frame, the determined positions of the two emitters are plotted in Figure 3e (gray and black). The average distance between the two cooperative emitters was found to be 911 ± 49 nm.

As the length of this nano-wire is 1.38 µm (as determined by TEM) the two emitters are not located at the ends of the NW. However, by inspecting the “map” of the EDX measurements displayed in Figure 3a, we were able to identify two regions with high O content (red numbers) separated by about 900 nm (highlighted with the gray and black dotted squares). This observation, and the necessity for sample aging in the presence of oxygen for

synchronous emission mentioned are strongly suggests that one can attribute cooperative emitters to silver clusters which are generated photochemically from silver oxide[29-32] and which are optically coupled through the silver nano-wire.

Additional support for the interpretation that the coupled emitters are silver clusters generated photochemically from silver oxide comes from the following observations: TEM studies showed that there is a 2-3 nm thin silver oxide layer around the silver nano-wires. During the TEM measurements it could be observed that exposure of the sample to the electron beam over long time scales damages the citrate layer around the nano-wires and also the silver oxide layer. Fluorescence measurements performed directly afterwards showed no fluorescence of previously emitting nano-wires. Additionally, EDX studies showed that some nano-wires, which did not exhibit any fluorescence emission, contained a relatively high amount of sulfide, which might prevent the formation of a silver oxide layer and thus the generation of silver cluster.

Moreover, additional support that coupling of the emitter occurs via the Ag-NW, most likely through surface plasmons comes from the fact that emitters on different NWs were never observed to emit simultaneously even when they were at comparable distances (data not shown). The question than arises whether the two emissive sites are both either active or whether one of them behaves in a passive fashion as a scatterer. In the case of one active center the laser beam would excite one entity which could emit itself but also couple energy to the surface plasmon of the nano-wire. This energy could then be transmitted to a passive center (like e.g. a defect site or a nano-particle), located on the same wire, but separated by some distance. In this case the emitted fluorescence intensity of both sites should be perfectly correlated. In contrast, we observed that the fluorescence signal of both emitting sites is coupled in some time ranges, but not correlated in other time intervals (Figure 4). This suggests that two or more active centers are involved. Thus, there have to be distinct emitting silver nano-cluster which are coupled trough plasmons.

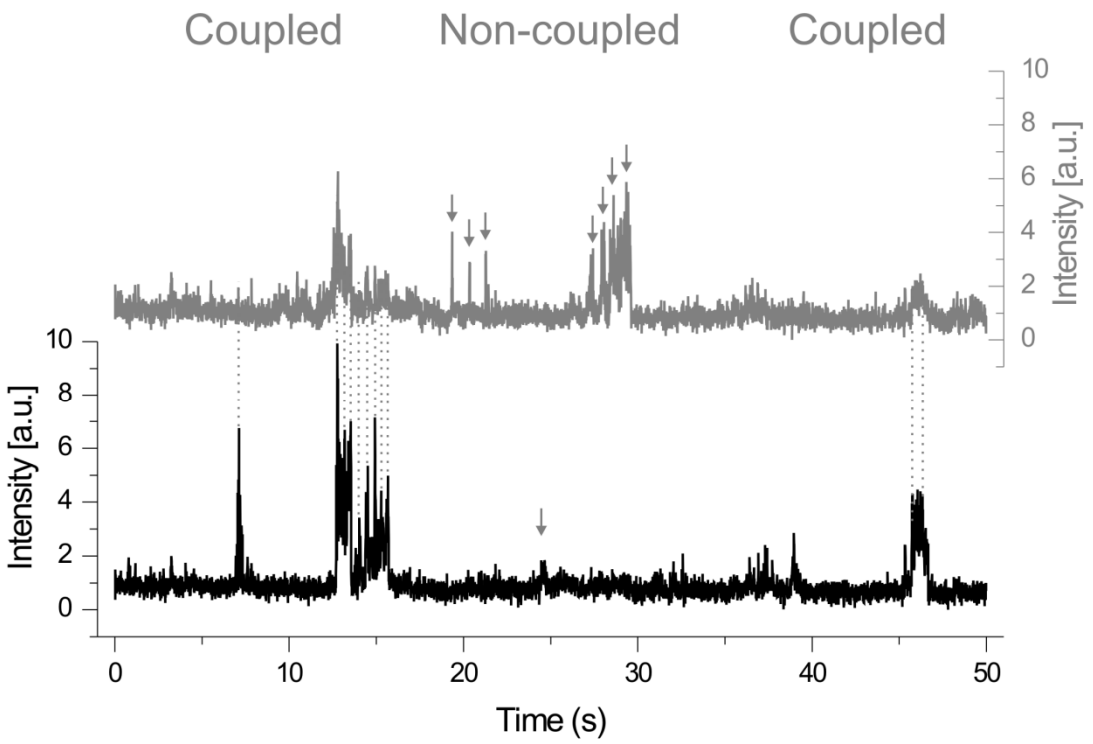

Figure 4: Fluorescence intensity time trajectories for two active emitting entities, which sometimes show the cooperative effect (indicated with dashed lines) but also show non-cooperative burst events (marked with arrows).

Conclusions

In summary, while emission of single entities on silver nano-structures is well studied, we observed a coupled emission for some of the investigated NWs (about 40 %). Such a coupled emission can only be observed if several emitters are investigated simultaneously. Since the emitters are located within a few µm on the NW, the coupled emission can be attributed to plasmonic coupling through the wire.

Materials and Methods

Crystalline Ag-NWs were synthesized using a seedless, surfactantless wet chemical fabrication developed by Caswell *et al.*[28] This solution, containing about 100 nm thick and up to 15 µm long Ag-NWs, was then spin-coated onto a glass cover slide (20 mm x 20 mm,

thickness 170 µm, Marienfeld). Fluorescence signals from individual nano-wires was then collected using a wide-field setup described previously.[40] Briefly, an Eclipse TE200 (Nikon) epi-fluorescence microscope with a high numerical aperture (NA) oil-immersion objective (Nikon Plan Apo 100x, NA = 1.40) was used and the nano-wires were excited at 633 nm with a He-Ne gas laser with an excitation power of 7 mW (measured in front of the microscope). Fluorescence was collected using a combination of filters (dicroic mirror 640 nm cutoff and bandpass 730/140 AHF) and imaged onto a back-illuminated electron multiplying charge-coupled device (EM-CCD) camera (Andor, iXon DV897). Series of typically 1000 fluorescence images were recorded with a temporal resolution of 10 ms per frame. To combine optical and structural properties we also performed experiments for which Ag-NWs were deposited on silicon nitride membranes (Si_3N_4, Agar Scientific). For these samples, a different objective lens (Nikon water immersion objective, NA 1.20 63x) was used. Some of the optically investigated nano-wires were then also studied by TEM in order to correlate fluorescence and structural features. These investigations were done using a FEI Titan 80-300 (S)TEM microscope equipped with a Gatan Tridiem image filter and an EDAX energy dispersive X-ray spectroscopy detector for analytical measurements. The Titan was operated with 300 kV. A high angle annular dark field (HAADF) detector from Fischione Instruments (Model 3000) is attached to the microscope for scanning TEM imaging.

Besides the correlative optical and TEM measurements some Ag-NWs were also investigated only using the TEM measurements and for these measurements samples were prepared by placing the Ag-NW on a carbon coated copper grid (Plano).

Acknowledgments

Financial support from DFG-SFB 749 and the cluster of excellence Nanosystems Initiative Munich (NIM) is gratefully acknowledged. The authors also thank C. Hohmann for TOC graphics design.

Supporting information

Movie S1. Series of 200 consecutive 3D surface plot images of the fluorescence intensity extracted from a wide-field fluorescence movie with 5000 frames showing the coupling of

the fluorescence emission between two entities along the nano-wire (10 frames / s, 1/10 real time, scale bar 2 µm).

Movie S2. Series of 200 consecutive 3D surface plot images of the fluorescence intensity extracted from a wide-field fluorescence movie with 5000 frames showing the coupling of the fluorescence emission between two entities along the nano-wire (10 frames / s, 1/10 real time, scale bar 1 µm).

Movie S3. Series of 200 consecutive wide-field fluorescence images extracted from a movie with 5000 frames showing a silver nano-wire exhibiting the cooperative effect at eight different emission sites simultaneously (10 frames / s, 1/10 real time, scale bar 2 µm).

This material is available free of charge *via* the Internet at http://pubs.acs.org.

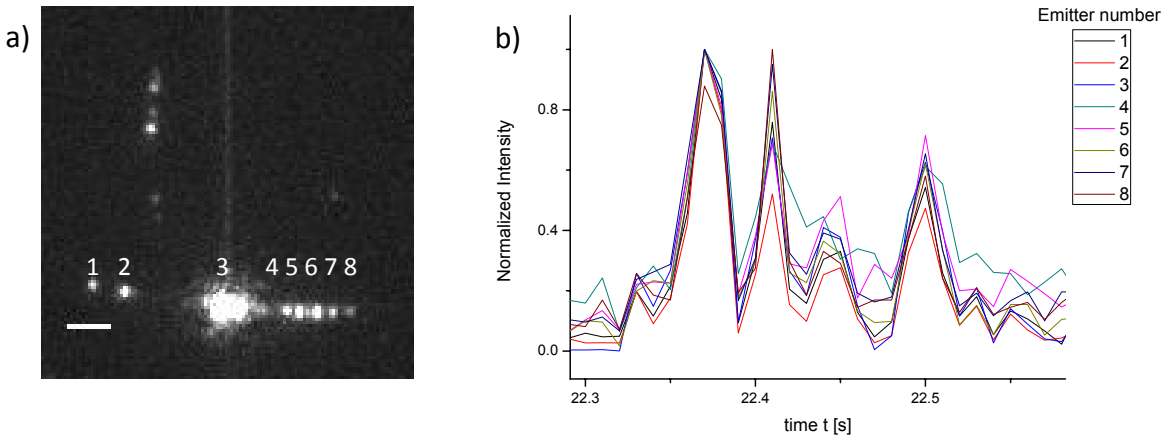

Figure S1: a) One selected wide-field fluorescence image of Movie 4-S showing a synchronous emission event of all eight emitters of one single nano-wire (scale bar is 2 µm). b) Magnification of a burst event in the fluorescence intensity time trace of the coupled emission of the eight emission sites from 1-S a. The coupled emission from all sites is clearly visible.

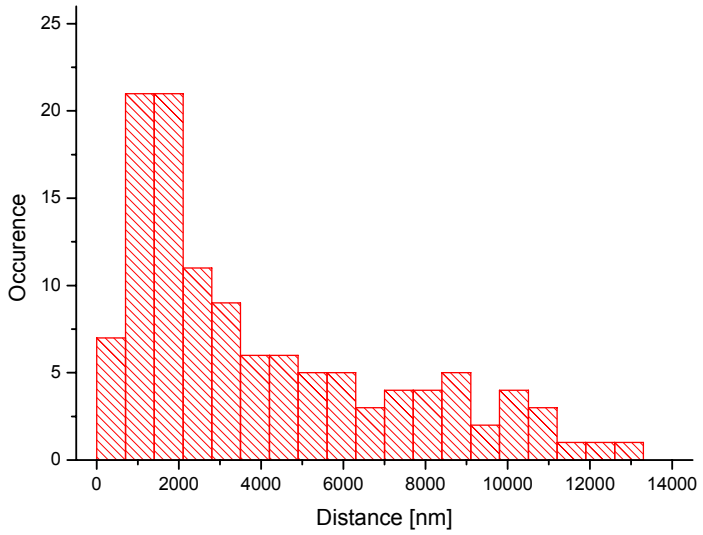

Figure S2: Histogram of the determined distances between several pairs of coupled emitters showing the cooperative effect. The distribution of these distances is continuous and decays with longer distances.

Table S1: Values of the quantification of the EDX spectra in order to find out which parts of the nano-wire in Figure 3a cause the emission, approximately 50 EDX measurements have been performed at different parts of the nano-wire and surrounding nano-particles using a electron beam size of about 1nm.

	1	**2**	**3**	**4**	**5**	**6**	**7**	**8**	**11**
O	56,04	38,03	20,34	17,40	17,91	52,91	30,23	13,08	95,60
S	3,32	1,06	1,32	2,33	5,49	4,14	4,69	4,01	2,37
Ag	40,32	60,63	78,33	80,26	76,57	42,95	65,06	82,90	2,01
	12	**13**	**14**	**15**	**17**	**18**	**21**	**22**	**23**
O	87,85	75,65	79,36	47,67	75,26	73,94	34,72	71,15	29,26
S	2,41	0	7,94	4,26	3,45	1,80	7,25	10,59	4,90
Ag	9,72	24,34	12,68	48,05	21,28	24,25	58,02	18,25	65,83
	24	**25**	**28**	**30**	**31**	**32**	**33**	**34**	**35**
O	48,42	75,56	22,77	87,52	88,38	67,01	53,21	40,71	41,25
S	7,03	8,85	4,10	2,81	2,94	11,37	6,48	3,70	7,13
Ag	44,53	15,57	73,10	9,96	8,66	21,61	40,30	55,58	51,81
	36	**37**	**39**	**40**	**41**	**43**	**44**	**45**	**46**
O	8,68	54,61	57,86	26,17	20,74	25,68	19,26	48,97	27,43
S	3,36	2,04	7,67	5,00	2,18	5,52	4,68	6,54	3,67
Ag	87,95	43,26	34,64	68,81	77,06	68,78	76,05	44,47	68,88
	47	**48**	**49**	**50**	**52**	**53**	**54**	**55**	**56**
O	36,71	41,59	26,77	35,91	40,39	36,19	15,78	41,30	42,53
S	6,03	4,49	3,84	4,58	5,80	4,02	3,13	2,92	3,15
Ag	57,25	53,91	69,37	59,49	53,80	59,77	81,08	55,79	54,30

References

1. W. L. Barnes, A. Dereux, T. W. Ebbesen, Surface plasmon subwavelength optics. *Nature* **424**, 824 (2003).
2. E. Ozbay, Plasmonics: Merging photonics and electronics at nanoscale dimensions. *Science* **311**, 189 (2006).

3. R. Kolesov *et al.*, Wave-particle duality of single surface plasmon polaritons. *Nature Physics* **5**, 470 (2009).
4. L. Novotny, Effective wavelength scaling for optical antennas. *Physical Review Letters* **98**, (2007).
5. P. Mohanty *et al.*, Simple vapor-phase synthesis of single-crystalline Ag nanowires and single-nanowire surface-enhanced raman scattering. *Journal of the American Chemical Society* **129**, 9576 (2007).
6. J. M. Baik, S. J. Lee, M. Moskovits, Polarized Surface-Enhanced Raman Spectroscopy from Molecules Adsorbed in Nano-Gaps Produced by Electromigration in Silver Nanowires. *Nano Letters* **9**, 672 (2009).
7. Y. R. Fang, H. Wei, F. Hao, P. Nordlander, H. X. Xu, Remote-Excitation Surface-Enhanced Raman Scattering Using Propagating Ag Nanowire Plasmons. *Nano Letters* **9**, 2049 (2009).
8. I. Yoon *et al.*, Single Nanowire on a Film as an Efficient SERS-Active Platform. *Journal of the American Chemical Society* **131**, 758 (2009).
9. J. C. Ashley, L. C. Emerson, DISPERSION-RELATIONS FOR NON-RADIATIVE SURFACE PLASMONS ON CYLINDERS. *Surface Science* **41**, 615 (1974).
10. J. Takahara, S. Yamagishi, H. Taki, A. Morimoto, T. Kobayashi, Guiding of a one-dimensional optical beam with nanometer diameter. *Optics Letters* **22**, 475 (1997).
11. J. C. Weeber, A. Dereux, C. Girard, J. R. Krenn, J. P. Goudonnet, Plasmon polaritons of metallic nanowires for controlling submicron propagation of light. *Physical Review B* **60**, 9061 (1999).
12. R. M. Dickson, L. A. Lyon, Unidirectional plasmon propagation in metallic nanowires. *Journal of Physical Chemistry B* **104**, 6095 (2000).
13. J. R. Krenn *et al.*, Non diffraction-limited light transport by gold nanowires. *Europhysics Letters* **60**, 663 (2002).
14. B. J. Murray, Q. Li, J. T. Newberg, J. C. Hemminger, R. M. Penner, Silver oxide microwires: Electrodeposition and observation of reversible resistance modulation upon exposure to ammonia vapor. *Chemistry of Materials* **17**, 6611 (2005).
15. S. E. Brunker, K. B. Cederquist, C. D. Keating, Metallic barcodes for multiplexed bioassays. *Nanomedicine* **2**, 695 (2007).
16. S. L. Pan, L. J. Rothberg, Enhancement of platinum octaethyl porphyrin phosphorescence near nanotextured silver surfaces. *Journal of the American Chemical Society* **127**, 6087 (2005).
17. S. L. Pan, Z. J. Wang, L. J. Rothberg, Enhancement of adsorbed dye monolayer fluorescence by a silver nanoparticle overlayer. *Journal of Physical Chemistry B* **110**, 17383 (2006).
18. S. H. Guo, D. G. Britti, J. J. Heetderks, H. C. Kan, R. J. Phaneuf, Spacer Layer Effect in Fluorescence Enhancement from Silver Nanowires over a Silver Film; Switching of Optimum Polarization. *Nano Letters* **9**, 2666 (2009).
19. A. V. Akimov *et al.*, Generation of single optical plasmons in metallic nanowires coupled to quantum dots. *Nature* **450**, 402 (2007).
20. C. Grillet *et al.*, Nanowire coupling to photonic crystal nanocavities for single photon sources. *Optics Express* **15**, 1267 (2007).
21. Z. Y. Fang *et al.*, Plasmonic Coupling of Bow Tie Antennas with Ag Nanowire. *Nano Letters* **11**, 1676 (2011).
22. L. A. Peyser, A. E. Vinson, A. P. Bartko, R. M. Dickson, Photoactivated fluorescence from individual silver nanoclusters. *Science* **291**, 103 (2001).

23. D. A. Clayton, D. M. Benoist, Y. Zhu, S. L. Pan, Photoluminescence and Spectroelectrochemistry of Single Ag Nanowires. *Acs Nano* **4**, 2363 (2010).
24. R. L. Zong *et al.*, Synthesis and optical properties of silver nanowire arrays embedded in anodic alumina membrane. *Journal of Physical Chemistry B* **108**, 16713 (2004).
25. N. R. Jana, L. Gearheart, C. J. Murphy, Wet chemical synthesis of silver nanorods and nanowires of controllable aspect ratio. *Chemical Communications*, 617 (2001).
26. Y. G. Sun, B. Gates, B. Mayers, Y. N. Xia, Crystalline silver nanowires by soft solution processing. *Nano Letters* **2**, 165 (2002).
27. B. Wiley, Y. G. Sun, Y. N. Xia, Synthesis of silver nanostructures with controlled shapes and properties. *Accounts of Chemical Research* **40**, 1067 (2007).
28. K. K. Caswell, C. M. Bender, C. J. Murphy, Seedless, surfactantless wet chemical synthesis of silver nanowires. *Nano Letters* **3**, 667 (2003).
29. R. Kötz, E. Yeager, Raman studies of the silver/silver oxide electrode. *Journal of Electroanalytical Chemistry and Interfacial Electrochemistry* **111**, 105 (1980).
30. T. Watanabe, O. Kawanami, K. Honda, B. Pettinger, EVIDENCE FOR SURFACE AG+ COMPLEXES AS THE SERS-ACTIVE SITES ON AG ELECTRODES. *Chemical Physics Letters* **102**, 565 (1983).
31. E. S. Brandt, SELECTIVE ENHANCED RAMAN-SCATTERING FROM AN OXACARBOCYANINE DYE AND 1-PHENYL-5-MERCAPTOTETRAZOLE ADSORBED TO SILVER AND SILVER-HALIDE SURFACES IN PHOTOGRAPHIC FILMS. *Applied Spectroscopy* **47**, 85 (1993).
32. X. Wang *et al.*, Enhancement mechanism of SERS from cyanine dyes adsorbed on Ag_2O colloids. *Spectrochimica Acta Part a-Molecular and Biomolecular Spectroscopy* **53**, 2495 (1997).
33. X. S. Xie, Single-molecule spectroscopy and dynamics at room temperature. *Accounts of Chemical Research* **29**, 598 (1996).
34. R. M. Dickson, A. B. Cubitt, R. Y. Tsien, W. E. Moerner, On/off blinking and switching behaviour of single molecules of green fluorescent protein. *Nature* **388**, 355 (1997).
35. A. P. Bartko, R. M. Dickson, Imaging three-dimensional single molecule orientations. *Journal of Physical Chemistry B* **103**, 11237 (1999).
36. W. E. Moerner, M. Orrit, Illuminating single molecules in condensed matter. *Science* **283**, 1670 (1999).
37. H. Chen *et al.*, Transmission-Electron-Microscopy Study on Fivefold Twinned Silver Nanorods. *The Journal of Physical Chemistry B* **108**, 12038 (2004).
38. C. Damm *et al.*, Shape Transformation Mechanism of Silver Nanorods in Aqueous Solution. *Small* **7**, 147 (2011).
39. X. Y. Wu, E. K. L. Yeow, Fluorescence blinking dynamics of silver nanoparticle and silver nanorod films. *Nanotechnology* **19**, 035706 (2008).
40. J. Kirstein *et al.*, Exploration of nanostructured channel systems with single-molecule probes. *Nature materials* **6**, 303 (2007).

6 Release pathways of interferon α2a molecules from lipid twin screw extrudates revealed by single molecule fluorescence microscopy

G. Sax*, F. Feil*, S. Schulze, C. Jung, C. Bräuchle, G. Winter, Release pathways of interferon α2a molecules from lipid twin screw extrudates revealed by single molecule fluorescence microscopy. *Journal of Controlled Release*, submitted.

[*] These authors contributed equally to this work.

Author contributions

F.F. labeled the proteins, conceived and performed the single molecule experiments and analyzed the single molecule data. G.S. fabricated the tsc-extrudates, recorded the SEM images, conceived and performed the release experiments.

1. Introduction

The sustained release of protein drugs from drug reservoirs is a very promising however challenging approach for long term delivery in patients. Usually, protein drugs are administered by subcutaneous injection or intravenous infusion and until today no product addressing e.g. nasal, pulmonary or transdermal delivery routes has been marketed except for Exubera® (inhalable insulin) which was withdrawn in 2007.[1, 2] After application, most protein drugs have only short half lives *in-vivo* which results in the need for frequent injections, short dosing intervals and thereby diminishes patient compliance. Thus, the production of depot formulations and implants offers a great potential to improve treatment efficacy and patient safety. Various materials have been used for the preparation of sustained release devices for macromolecules including hydroxyethylmethacrylate,[3] ethylene-vinyl-acetate copolymer,[3, 4] polyvinyl alcohol,[3] polylactic acid (PLA) and polylactic-co-glycolic acid (PLGA).[5, 6] However, problems regarding the stability of the drug during production and/or release and unfavorable biodegradation properties of the matrices rendered all materials so far unfeasible. As a consequence, until today only one parenteral

depot system (Nutropin Depot®, Genentech, 1998) for the sustained release of a protein drug (human growth hormone) was marketed but withdrawn in 2004.

During the last decade, lipids gained more and more interest as matrix materials for the preparation of parenterally applicable formulations[7-11] as they show good biocompatibility[12, 13] and biodegradability.[12, 14] Sustained release of macromolecules from various lipidic devices was proven for protein drugs including brain-derived neurotrophic factor (BDNF)[15], recombinant human interferon α2a (IFNα)[7, 15-17], insulin[7] and interleukin-18.[9] Schulze *et al.* introduced a new preparation technique for the production of protein loaded triglyceride based lipid implants by twin screw extrusion (tsc-extrusion)[18] featuring the advantages of being an up-scalable, continuous production process with gentle preparation temperatures and without the use of organic solvents. The resulting implants were rod-shaped and thus easily applicable. It was shown that tsc-extrusion results in a more sustained protein release behavior than e.g. compression and offers a favorable production platform for the preparation of lipid based implants. However, the mechanism by which the more sustained protein release was achieved has not been fully understood.

The general mechanisms of sustained protein release from inert matrices were already extensively reviewed.[4, 19, 20] Various factors including drug/compound particle sizes, drug load, implant geometry and preparation technique have been identified to influence protein release kinetics.[21] Furthermore, it was found that macromolecular drug release from such devices is much more sustained than mathematical models predicted even if varying porosity values of the devices and smaller diffusion coefficients of the incorporated drugs were taken into account.[19] Multiple factors were identified to account for the sustained release: concentration dependent diffusion, random pore topology, sealing effects and a constricted pore geometry.[4, 20] Based on the groundbreaking work of Langer *et al.*[3, 4, 19, 20] it is common sense that the “constricted pore-geometry” leads to a so-called “random walk” of the protein within the inert implant matrix and is a major contributor to the sustained release behavior. Hereby, the protein diffuses upon hydration within water-filled pores inside the implant and is trapped within each pore until it finds its way out through a narrow connecting channel.[19] Due to this retention within individual pores, the release becomes

sustained and very slow release rates can be achieved. However, this "random walk" could never be visualized or proven by any other technique than mathematical modeling.[22]

Today, new techniques are available which allow the tracking of single molecules, e.g. within mesoporous matrices by wide-field fluorescence microscopy.[23, 24] In this study we used this technique to track individual fluorescently labeled recombinant human IFNα protein molecules within lipid tsc-extrudates and directly determined the real diffusion coefficients of these molecules for the first time. Hereby we were able to elucidate the major mechanisms which contribute to the sustained release from tsc-extrudates. The first mechanism, which has also been reported before, is the formation of large pores by polyethylene glycol (PEG) dissolution within the lipidic host matrix (consisting of the high-melting lipid D118 and the low melting lipid H12) upon incubation in a buffer solution. In addition to this, we found that the lipidic implant matrix is in fact not as "inert" as it has been presumed in the previous studies described above. In particular, the low melting lipid H12 partially melts during the production process at elevated temperatures and some amount of the protein molecules gets embedded into this H12 melt. Therefore, these molecules are trapped at incubation temperatures below H12 melting and only get released from molten H12. The release from this lipid phase is the second mechanism contributing to the more sustained release from tsc-extrudates, because the diffusion coefficient of protein molecules in the triglyceride melt is much slower than within the large pores formed by PEG.

In the special case of incubation at temperatures below the melting point of H12, protein molecules diffusing within small micropores with sizes of up to a few micrometers were detected within the implants. We assumed that these protein molecules were diffusing in PEG-buffer-solutions in cracks of the lipid matrix. The protein molecules in this case were trapped within cavities until they randomly found an accessible connection to the next one. This diffusional behavior is similar to the "random walk" between neighboring cavities described by Siegel and Langer,[19] however it takes place at a length scale which is about two orders of magnitude smaller. Analogue to their finding, the retention within the micropores can be considered as a third mechanism for the sustained release from tsc-extrudates at temperatures below H12 melting.

2. Materials and methods

2.1. Materials

Triglycerides (H12, Dynasan D118) were a gift from Sasol (Witten, Germany). PEG 6000 was donated from Clariant (Wiesbaden, Germany). Hydroxypropyl-β-cyclodextrin (HP-β-CD) was provided from Wacker (Burghausen, Germany). For dye labeling ATTO647N NHS-ester was purchased from ATTO-TEC (Siegen, Germany). Recombinant human interferon α2a (IFNα) was a gift from Roche (Penzberg, Germany). The µ-Stick 8-well microscopy slides and hydrophobic uncoated 0.2 mm µ-Slide Luer® ibiTreat microscopy slides were purchased from ibidi GmbH (Martinsried, Germany). Buffer salts were of analytical grade and bought from Merck (Darmstadt, Germany).

2.2. Fluorescence labeling of IFNα

30 µL of an IFNα solution (1.56 mg/mL, MW = 19.2 kDa, n = $2.44 \cdot 10^{-9}$ mol) were mixed with 70 µL of a PBS solution of pH 8.0. Then approximately 0.1 mg of ATTO647N NHS-ester (M = 843 g/mol, n = $1.18 \cdot 10^{-7}$ mol) were added. The mixture was heated at 30°C for 1.5 h and vortexed shortly each 10 min. Excess unlabeled dye was removed afterwards from the fluorescent labeled proteins (fluo-IFNα) by centrifugation at 2000 rcf for 1 min in a Micro Bio-Spin 6 Chromatography Column (Bio-Rad Laboratories) where the free dye was bound to the column but the labeled protein stayed in solution.

2.3. Protein analysis

IFNα was quantified by SE-HPLC in analogy to the method described by Mohl *et al.* (Dionex Ultimate 3000, flow rate: 0.5 mL/min, UV: 215 nm+280 nm, Tosoh TSKgel 3000SWXL).[16] Samples were additionally assessed by a fluorescence detector (exc. 644 nm; em. 669 nm) after separation by SE-HPLC.

2.4 Preparation of IFNα lyophilisates

IFNα was lyophilized as described by Herrmann and Mohl.[25] In brief, HP-β-CD and IFNα were mixed in a ratio of 3:1 (m/m) and spiked with a dilution of freshly labeled fluo-IFNα. The solution was adjusted to pH 4.2 (with acetic acid) and lyophilized. The resulting cake comprised 10^{-9} (m/m) fluo-IFNα.

2.5 Preparation of lipid twin-screw extrudates and protein-lipid dispersions for wide-field fluorescence spectroscopy

Lipid tsc-extrudates were prepared as described by Schulze *et al.*[18] with a Haake MiniLab® Micro Rheology Compounder (Thermo Haake GmbH, Karlsruhe, Germany). In brief, a lipid powder blend comprising D118 as high melting lipid and H12 as low melting lipid was mixed with 10% of lyophilized PEG 6000 and 10% of IFNα lyophilisate (1:3 with HP-β-CD). Extrusion of rod-shaped implants was performed through a 1.9 mm outlet die in steady-state mode with closed bypass.

Rod shaped implants were forged into a flatter cylinder by the application of pressure on the warm and formable implant after tsc-extrusion. The flat cylinder was placed into a µ-Stick 8-well microscopy slide (ibidi GmbH, Martinsried, Germany) and incubated in PBS pH 4.0 for wide-field fluorescence microscopy (Figure 1, left).

Additionally lyophilized IFNα was mixed with pure H12 in a ratio of 1:10 (w/w) and heated in a beaker until the lipid became creamy. The melt was casted into µ-Stick 8-well microscopy slides (Figure 1, right). The protein-lipid dispersion was also analyzed by wide-field fluorescence microscopy.

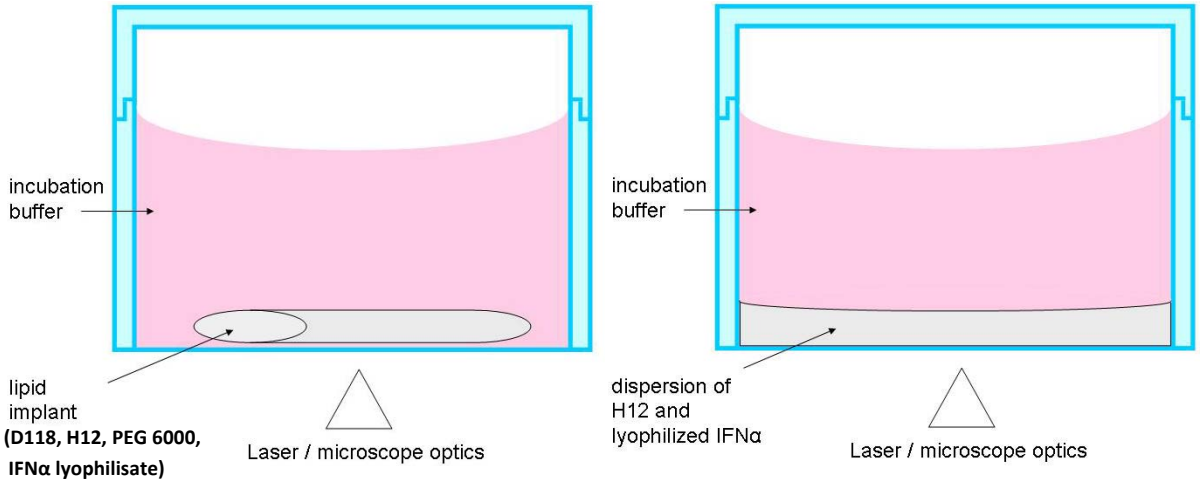

Figure 1: Experimental setup for single molecule wide-field fluorescence spectroscopy studies of fluo-IFNα molecules in tsc-extrudates (left) and protein-lipid dispersions (right).

2.6 Preparation of PEG samples for fluorescence microscopy

PEG 6000 was dissolved in PBS pH 4.0 to give final concentrations of 30%, 40% and 53% (w/w). 15 mL of these solutions were spiked with 15 µL of a solution of IFNα (conc. 1.56 mg/mL) which comprised 1.0 x 10^{-9} mg/mL of fluo-IFNα. Thus, the theoretical concentration of fluo-IFNα was 1.0 x 10^{-12} mg/mL in the PEG solutions. The solution was injected into a 0.2 mm µ-Slide Luer® ibiTreat microscopy slide (ibidi GmbH, Martinsried, Germany) and single molecule wide-field fluorescence microscopy was performed.

2.7 Scanning electron microscopy (SEM)

SEM was performed with a 6500F (Jeol GmbH, Eching, Germany). Samples were dried in a vacuum chamber (VO 200, Mammert, Schwabach, Germany) at 25°C and 20 mbar for 6 days and analyzed without coating.

2.8 Wide-field fluorescence microscopy

Fluorescence images were acquired with a wide-field setup, using a Nikon Eclipse TE200 epifluorescence microscope and an oil-immersion objective with high numerical aperture (Nikon Plan Apo 100x/1.40 N.A. Oil). The Atto647N dye molecules were excited at 633 nm

with a Coherent He-Ne gas laser (75 mW max. at 632.8 nm) with an intensity of 0.1-0.7 kW cm^{-2}. The fluorescence was detected with an Andor iXion DV897 back-illuminated EM-CCD camera in frame transfer mode (512 px x 512 px). Incident laser light was blocked by a dichroic mirror (640 nm cutoff, AHF) and a band-pass filter (730/140, AHF). More details about the setup have been reported previously.[23] Fluorescence microscopy was performed at ambient temperatures or at 37°C which resembles the incubation temperature during protein release tests.

2.9 Protein tracking, visualization of the random walk and calculation of diffusion coefficients

Single particle tracking (SPT) was employed to track the positions of the single molecules in the acquired fluorescence images and obtain the single trajectories by fitting frame by frame theoretical diffraction patterns (described in detail by Kirstein *et al.*[23]) to the fluorescence signals. With this method the positions of the fluorophores can be obtained with an accuracy of down to 10 nm.

The diffusion coefficient for each individual trajectory can be extracted from the linear part of the mean square displacement (MSD) plots according to the Einstein-Smoluchowski relation MSD = 4 Dt assuming an isotropic Brownian diffusion in all three dimensions while only using the two-dimensional projection of the recorded images.

2.10 Protein release studies

Tsc-extrudates were cut into rod-shaped implants with 2.5 cm length and incubated in protein low-bind tubes (Eppendorf AG, Hamburg, Germany). For release studies from protein-lipid dispersions, the triglyceride H12 was molten at 40°C and admixed with 10% of IFNα lyophilisate. Afterwards the dispersion was cast into protein low-bind Eppendorf tubes.

Protein release studies were performed in 1.9 mL isotonic PBS buffer pH 4.0 (+0.05% sodium acid). At predetermined time points the incubation buffer was completely exchanged and the samples were assessed for protein content by SE-HPLC as described above. Tsc-extrudates were incubated at 37°C in a water bath without agitation. Protein release from lipid-protein dispersions was assessed at 20°C, 29°C, 33°C and 37°C.

3. Results and discussion

3.1 Scanning electron microscopy

Scanning electron microscopy of tsc-extrudates before release tests showed a smooth and compact surface and a compact matrix with no porous structure in the core (Figure 2 A). After the release test (27 days) the matrix of the implant changed and pores and channels became visible with diameters ranging between 1-100 µm (Figure 2 B). The creation of large pores and an interconnected pore network is explained by dissolution and release of lyophilized PEG and protein powder from the matrix. Various authors described the formation of such a pore network to be the major driving force for total drug release from inert matrices[4, 19] and the formation of pores and channels within similar lipidic devices has already been described.[16]

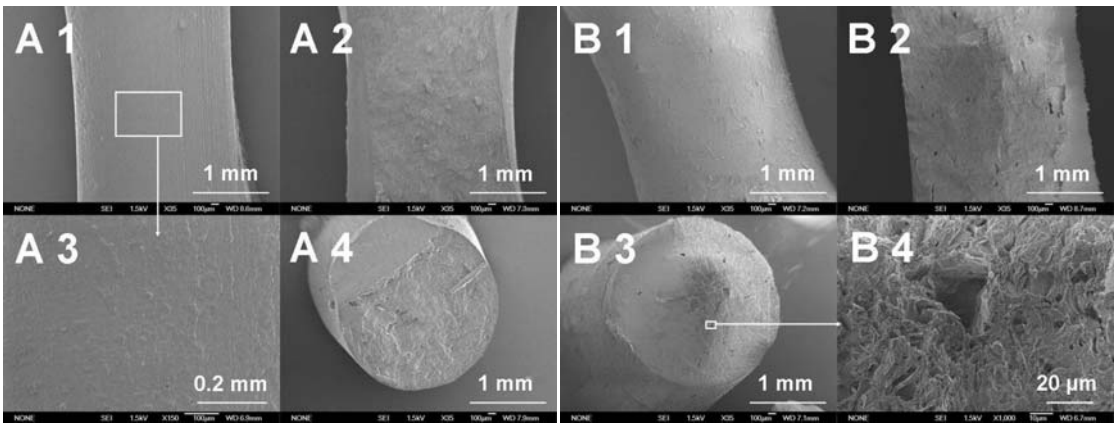

Figure 2: Scanning electron microscopy images of tsc-extrudates before (A) and after (B) *in-vitro* release tests. A 1 + B 1: Implant surface; A 2 + B 2: longitudinal cross-section; A 3: close-up of implant surface; A 4 + B 3: upright cross section; B 4: close-up of upright cross section.

3.2 Quantification of fluo-IFNα

Determination of the total protein concentration after fluorescence labeling by UV detection (215 nm + 280 nm after SE-HPLC) showed a decrease of the protein concentration from 1.6 mg/mL to 1.0 mg/mL which can be attributed to the labeling process and the subsequent protein purification steps. Neither the UV chromatographs nor the fluorescence chromatographs show the presence of dimers or soluble oligomers after the labeling process and thus all labeled protein is ascertained to be monomeric. The slight shift between the retention times of the UV and the fluorescence signal results from the in-line connection of the fluorescence detector after the UV detector (Figure 3).

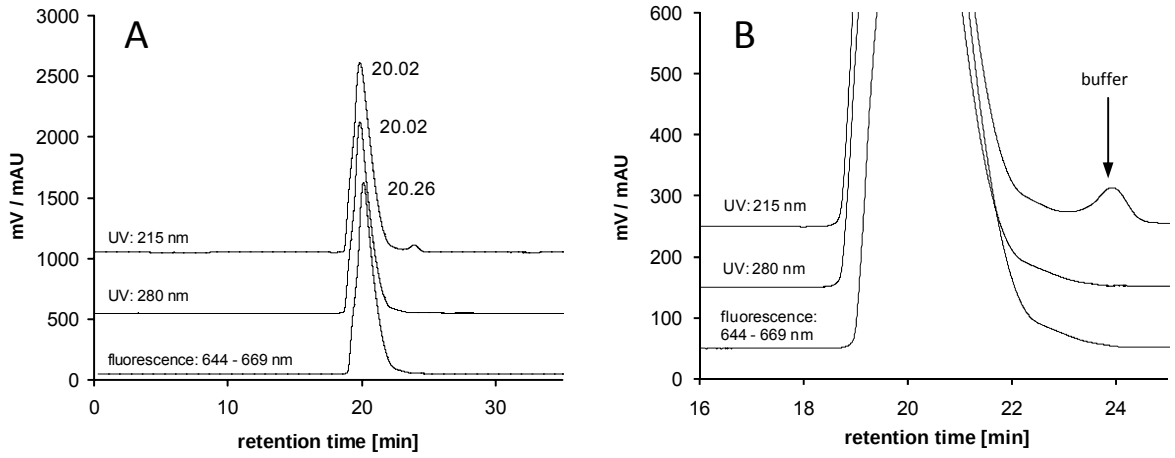

Figure 3: A) SEC chromatographs with UV (215 nm and 280 nm) and fluorescence (exc: 644 nm, em: 669 nm) detection of Atto647N dye labeled IFNα (fluo-IFNα) after SE-HPLC separation. B) Magnification of the time interval, in which the signals were detected, from Figure 3A.

3.3 IFNα release studies from tsc-extrudates

The tsc-extrudates used for the IFNα release studies contained high melting lipid D118, low melting lipid H12, 10% of lyophilized PEG 6000 and 10% of IFNα lyophilisate (1:3 with HP-β-CD; for details see 2.4 and 2.5). The protein was released from the tsc-extrudates at pH 4.0 and 37°C in a diffusion controlled way over a period of 27 days liberating up to 96% of the incorporated protein mass. Incubation pH was set to 4.0 to prevent IFNα precipitation in

the presence of PEG 6000 as reported by Herrmann *et al.*[25, 26] They studied IFNα release in the presence of PEG at two pHs (4.0 and 7.4) and showed that PEG can be used to achieve a triphasic IFNα release profile from lipid implants at pH 7.4 which was induced by a protein precipitation step. However, release at pH 4.0 resulted in a normal, diffusion controlled IFNα release over time. In this study we observed a similar release profile. Directly upon incubation a burst-release occured first, liberating protein molecules from the surface and outer regions of the tsc-extrudate (Figure 4 and Figure 4 inset). Afterwards a linear relation between the released amount of IFNα and the square-root of time ($t^{1/2}$) could be established in our measurements (Figure 4 inset). This is a typical characteristic for a diffusion controlled release from inert matrices according to Higuchi's square root of time kinetics.[27] Higuchi's approximation for the release from inert matrices describes our data quite well up to about 70% of drug release. For higher amounts of released protein the release was slowed down. So far the underlying reason for this more sustained release has not been quite understood. We will identify and present the associated mechanism responsible for this more sustained release later in this study.

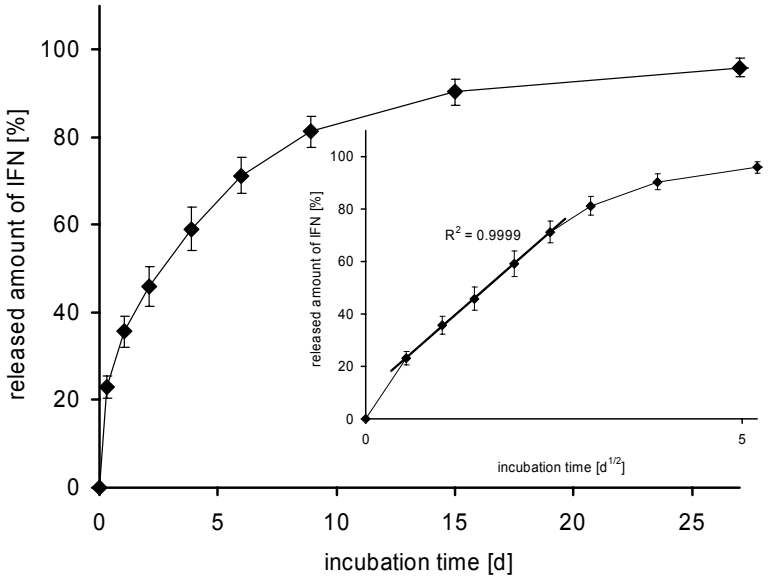

Figure 4: IFNα release from tsc-extrudates (n = 6) at 37°C in PBS buffer pH 4.0. A linear correlation between the square root of time and the released amount of protein is shown in the inset derived from Figure 4 by plotting the square root of the incubation time. Data points are connected by straight lines for guidance of the eye.

3.4 IFNα release from protein-lipid dispersions

In order to mimic the behavior of H12 triglyceride rich phases within tsc-extrudates, release experiments from formulations of protein lyophilisate dispersed in pure H12-protein were performed. Release kinetics from such dispersions were found to be strongly dependent on incubation temperature. At 20°C and 29°C an initial burst release of about 4% was detected and afterwards a linear release phase started which lasted until day 14 and leveled into a plateau phase liberating a maximum of only 25% IFNα (Figure 5 curves 1 and 2). Differential scanning calorimetry (DSC) thermograms (data not shown for pure H12 samples) showed that the triglyceride was solid at these temperatures and thus only a small fraction of the protein, probably from the surface or cracks within the implant, was released whereas the main fraction remained trapped within the inert triglyceride matrix. At 33°C, the release kinetics accelerated due to partial melting of H12 thus increasing the mobility of the embedded proteins and 91% of the protein was released within 14 days (Figure 5 curve 3). Only a part of the lipid was molten at 33°C and the lipid-protein dispersion became "waxy" but remained at the bottom of the eppendorf tube during the release test. Immediate and complete IFNα release (99% within 1 day) was achieved if the incubation temperature was increased to 37°C (Figure 5 curve 4). Hereby the lipid was completely molten and separated on top of the aqueous phase. Thus, a strong influence of temperature on the release of IFNα from H12 lipid was found.

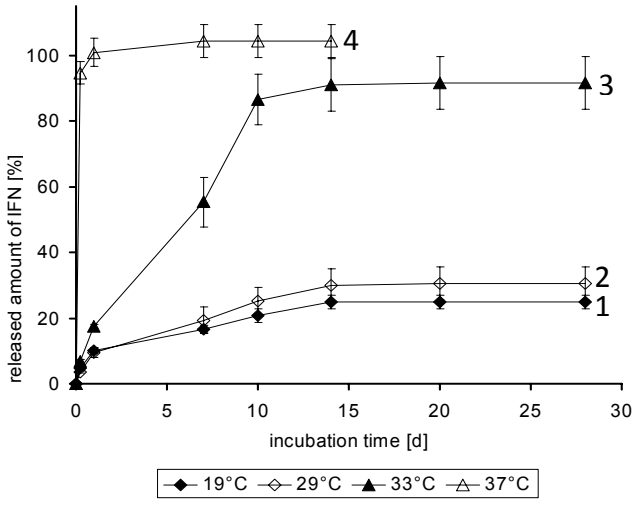

Figure 5: IFNα release from lipid-protein dispersions at different temperatures (19°C, 29°C, 33°C, 37°C). Data points are connected by straight lines for guidance of the eye.

3.5 Wide-field fluorescence microscopy of tsc-extrudates

Taking into account the production process in which the four solid compounds (D118, H12, PEG 6000 and IFNα lyophilisate with HP-β-CD; for details see 2.4 and 2.5) were mixed, one would expect a more or less heterogeneous distribution of small domains of these solid components in the implants before incubation. Moreover, only regions with IFNα lyophilisate and HP-β-CD containing fluorescently marked protein (fluo-IFNα) molecules should show fluorescence, while all other regions (D118, H12 and PEG 6000) should be dark. This expectation is supported by the presumption of an "inert" matrix described by Langer *et al.*[3, 4, 19, 20] Indeed, fluorescence microscopy of lipid tsc-extrudates at room temperature and before incubation in PBS buffer revealed an extensive heterogeneity of the implant matrix with two different types of phases. The first type showed large areas with strong fluorescence signals (type 1 areas), which had dimensions of about 1-100 µm in diameter. They can be attributed to regions with IFNα lyophilisate and HP-β-CD containing a high amount of fluo-IFNα particles (Figure 6a). Surprisingly, all other areas (Figure 6b) were not completely dark. Instead, a second type of area containing fluorescence signals of protein molecules in a very low concentration was detected (type 2 areas) indicating finely distributed protein all over the implant (Figure 6b). Therefore, the tsc-exrudates do not possess a totally "inert", empty lipid matrix as it has been proposed so far. In a next step we then observed the situation evolving during release.

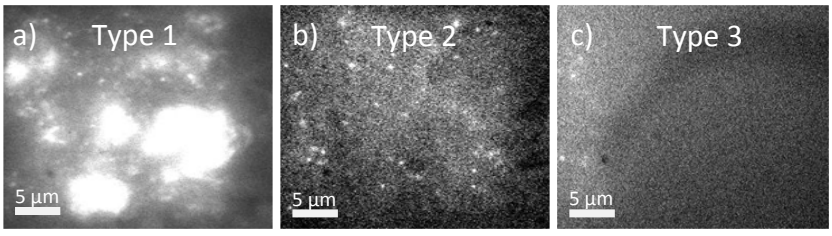

Figure 6: Fluorescence microscopy images of tsc-extrudates. a) Dye-labeled protein particle reservoirs. b) Finely distributed single protein molecules. c) Former protein reservoir which vanished after incubation with buffer solution forming large pores.

Upon incubation in PBS buffer (37°C, pH 4.0) the situation within the implant changed and areas with strong fluorescence (type 1 areas) containing IFNα lyophilisate with HP-β-CD vanished over time (within a few days) and merged into "dark areas" (type 3 areas). These

areas of type 3 (Figure 6c) had dimensions of about of 10-200 µm and were apparently slightly larger than the areas containing IFNα lyophilisate with HP-β-CD of type 1. Additionally, the areas of type 3 are correlated well in size and shape with the porous structure as shown in SEM images (Figure 2B). Therefore, we concluded that areas of type 3 might correspond to areas where the water soluble parts of the tsc-extrudate, namely IFNα lyophilisate with HP-β-CD and PEG 6000, were dissolved by PBS buffer and released from the implant forming large "pores". Within such large pores the diffusivity of the protein molecules was expected to be very high, probably similar to the diffusivity in pure PBS buffer solution. Usually we are not able to resolve molecular diffusion in a pure low viscous solution with our microscopic technique, because of the limited time resolution of the CCD-camera. Therefore, we could not visualize protein molecules within the large pores of the implant in most cases. However, in some cases we were able to detect and track a few fluo-IFNα molecules diffusing inside such large pores (Movie 1-S). For each of those molecules the trajectory could be analyzed (see 2.9) and the mean square displacement (MSD) was plotted as a function of time (Figure 7 red curves). All plots were linear over time Δ t following the relation for normal diffusion MSD = 4Dt, where D is the diffusion coefficient. The spread of the single molecule MSD plots is typical for single molecule experiments and shows the local heterogeneities at the nanometer scale of the surrounding medium for each molecule. Using ensemble methods, the influence of this locally heterogeneous environment on the diffusion of structurally identical molecules is hidden due to averaging. The mean diffusion coefficient of $\langle D \rangle = 8.5 \pm 2.5 \times 10^6$ [nm^2/s] was extracted from the averaged MSD plot (Figure 7 black line).

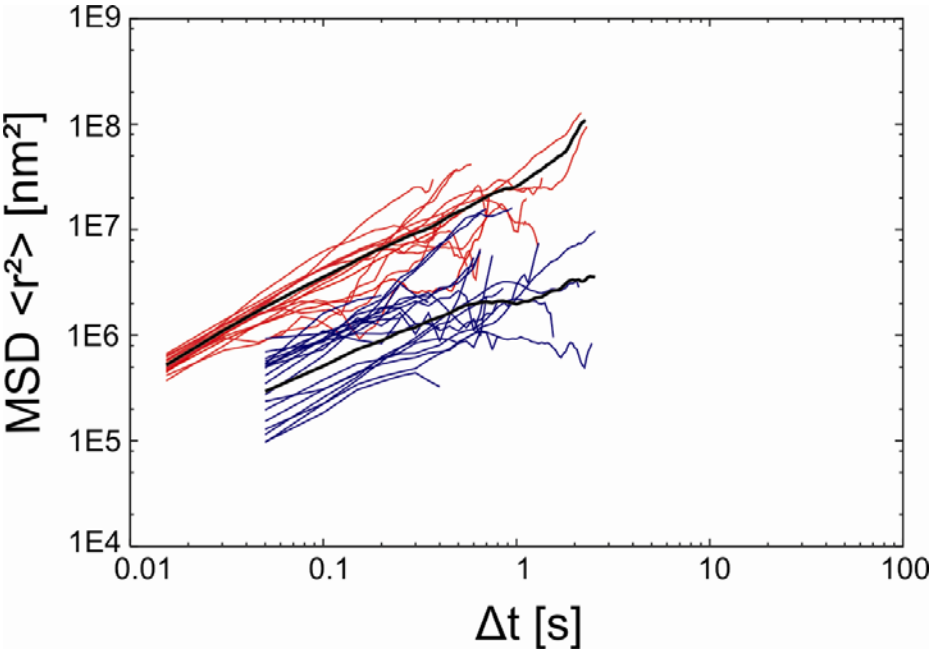

Figure 7: Mean square displacements (MSDs) of fast (red) and slow (blue) single IFNα molecules diffusing in a large pore of a type 3 area or a type 2 area, respectively, of a tsc-extrudate at 37° C and pH 4.0. The black lines show the average MSDs of the respective single tracking experiments. The determined mean diffusion coefficients are $<D> = 8.5\pm2.5\times10^{6}$ [nm^2/s] for the fast and $<D> = 1.6\pm0.9\times10^{6}$ [nm^2/s] for the slow protein species.

The second type of fluo-IFNα molecules which were finely dispersed in areas of type 2 of the tsc-extrudate matrix also started to move directly upon incubation at 37° C and pH 4.0. These molecules, however, moved more slowly (Movie 2-S) than the ones found in the large pores of type 3 areas. The motion of this second species was also controlled by normal diffusion as the MSD was linearly correlated to time (Figure 7 blue curves). The distribution of the single molecule MSD plots of these slow fluo-IFNα molecules is broader than that of the fast proteins indicating a more heterogeneous environment. The mean diffusion coefficient of the slow proteins was determined to be $<D> = 1.6\pm0.9\times10^{6}$ [nm^2/s], which is about 5-fold lower than for the fast proteins in the large pores.

In summary normal diffusion was found to be the main driving force for protein release from tsc-extrudates in both type 2 and type 3 areas showing two different diffusion coefficients. Now the question arises to which phases of the tsc-extrudates these areas belong.

3.6 Diffusion pathways of fluo-IFNα molecules in tsc-extrudates

We already saw that the fast protein species of type 3 areas was diffusing in large pores formed by dissolution of PEG 6000 in PBS buffer and IFNα lyophilisate with HP-β-CD. Furthermore, since the tsc-extrudate matrix seems to be not totally inert and empty, the second protein population found in areas of type 2 might have been diffusing in phases of molten PEG or lipid (H12 or D118) at the incubation temperature of 37°C. DSC thermograms of tsc-extruded implants indicated that only the low-melting lipid H12 was molten at the incubation temperature of 37°C within the implant while the other compounds were still solid (D118, PEG 6000, see Figure 8).

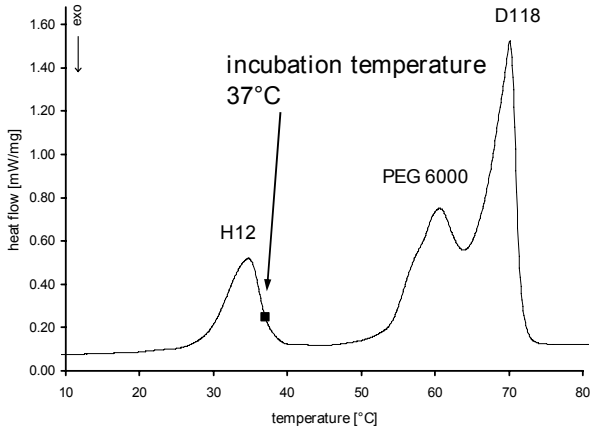

Figure 8: DSC thermogram of a tsc-extrudate comprising the triglycerides H12, D118 and the water-soluble excipient PEG 6000.

In order to indentify the phases more precisely we investigated the diffusion of IFNα molecules in solutions of PEG 6000 in isotonic PBS (pH 4.0, 37°C) and also the diffusion of IFNα in molten H12 for comparison with the two populations found in the implant during incubation.

As stated before, the diffusivity of molecules in pure solution is usually too high to be resolved with our setup. Therefore, a minimum concentration of 53% (w/v) PEG was necessary in the experiments to increase the viscosity of the PBS buffer solution and thus to slow down the diffusion of the protein particles in order to allow the visualization of these diffusing IFNα molecules (Movie 3-S). Within such a 53% (w/v) PEG solution we tracked individual fluo-IFNα molecules and calculated the mean diffusion coefficient from the MSD

plot (Figure 9 black) to be <D> = 14.1 ± 6.5 x 10^6 [nm^2/s] in an analogue way as before. This value is in good agreement to the fast fluo-IFNα population in the large pores (type 3 areas) of the tsc-extrudate (see both values in Table 1; average MSD plot of the fast fluo-IFNα molecules see Figure 9 red).

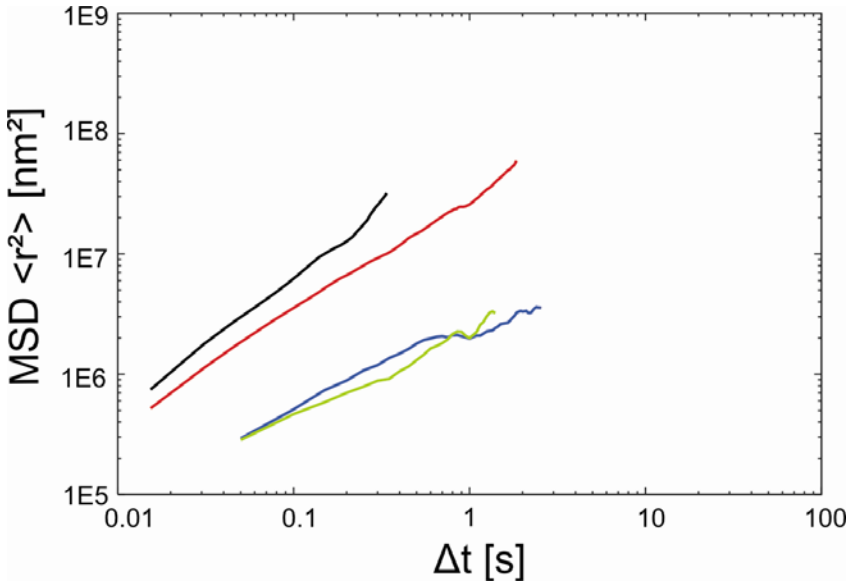

Figure 9: MSDs of fast (red) and slow (blue) IFNα molecules diffusing in tsc-extrudates and respective molecules in PEG solution (black) or dispersions with H12 (green). The linear correlation indicates normal diffusion of the molecules. All MSDs are displayed as average MSD plots from the respective individual tracking experiments.

Table 1: Mean diffusion coefficients of IFNα molecules as calculated from wide-field microscopy measurements in different environments: tsc-extrudates (fast and slow species), 53% PEG solution and molten H12. For a detailed analysis of the distribution of the single molecule diffusion coefficients see Figure S-1 in the Supporting Information.

	<D> [nm^2/s]
tsc-extrudate – fast species	8.5 ± 2.5 x 10^6
53% PEG solution	14.1 ± 6.5 x 10^6
tsc-extrudate – slow species	1.6 ± 0.9 x 10^6
H12 melt at 37°C	0.9 ± 0.4 x 10^6

For comparison, Herrmann *et al.* measured the diffusion coefficient of IFNα molecules in solutions of PBS by a modified open-end capillary technique proposed by Anderson and Saddington.[26, 28] They calculated a diffusion coefficient of IFNα in pure PBS of 1.8 x 10^8 [nm^2/s]. This is about 12-times faster than the molecules in the 53% (w/v) PEG solution and about 21-times faster than the fast fluo-IFNα population in the large pores (type 3 areas) of the tsc-extrudate, which were both detected by wide-field fluorescence spectroscopy. This result is in good agreement with the fact that we are usually not able to resolve molecular diffusion in a pure low viscous solution with our measurement technique as stated earlier and therefore are only able to detect the slower molecules diffusing in more viscous PEG solutions.

At this point we wanted to identify the second population of diffusing IFNα molecules detected in type 2 areas. For this single molecule studies of the diffusion of finely dispersed protein molecules in pure H12 were performed at 37°C (Movie 4-S). Tracking of the single molecules allowed to calculate a mean diffusion coefficient of <D> = 0.9 ± 0.4 x 10^6 [nm^2/s] from the MSD plot (Figure 9 green). This MSD plot is very similar to the MSD plot of the slow population diffusing in type 2 areas in the tsc-extrudate (Figure 9 blue). Therefore, we concluded that the slow protein species found in type 2 areas of the implant is in fact diffusing within molten H12 phases. Moreover, the diffusion of proteins in molten H12 and the slow motion of the molecules within this phase might be the reason why the release from tsc-extrudates is more sustained and slows down after the initial diffusion controlled linear release as shown in the release profile (Figure 4) before. This statement is supported by release measurements in tsc-extrudates with lysozyme,[29] which is a protein with similar properties compared to IFNα. In these measurements the release profiles of the protein at temperatures where H12 was molten showed a similar slow down of the release rate after the linear regime, whereas incubation at temperatures where H12 was still solid lead to a linear correlation over the complete time range and showed no slow down of the release rate. Thus, this more sustained release behavior seems to be caused by the slow release from molten H12 phases.

In summary, we were able to identify both species of diffusing protein molecules within tsc-extrudates and could thereby elucidate the major mechanisms for the more sustained release from such matrices.

3.7 Diffusional behavior of IFNα molecules in micropores

In the special case of incubation at 23°C (below the melting point of H12), protein molecules diffusing within small micropores with sizes ranging in the nanometer and low micrometer regime were detected within the implants (Figure 10). The protein molecules found in these micropores diffused most likely in cracks of the lipid matrix filled with PEG-buffer-solution. These cracks were probably created upon cooling of the lipid matrix after the manufacturing process. Upon incubation at 37°C no such structures could be detected anymore. The reason for this is sealing of the microcavities by partial implant melting.

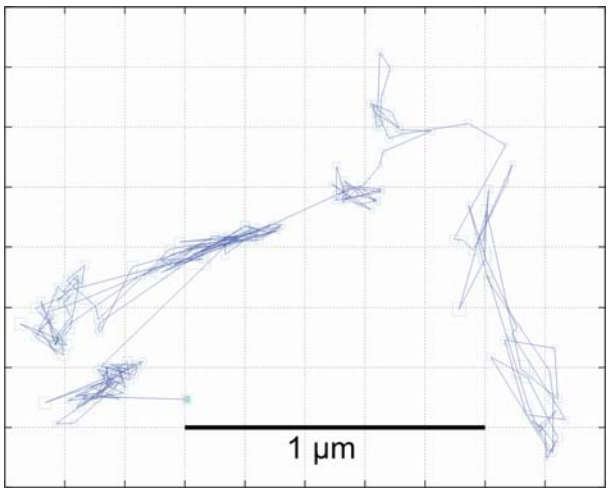

Figure 10: Trajectory of a single IFNα molecule diffusing in micropores within lipid tsc-extrudates plotted with box-error bars indicating the positioning accuracy of the single molecule tracking.

The diffusing protein molecules in this case were trapped within microcavities until they randomly found an accessible connection to the next one. This diffusional behavior is similar to the "random walk" between neighboring cavities described by Siegel and Langer,[19] however, takes place at a length scale which is about two orders of magnitude smaller. Analogue to the finding of Langer *et al.*, the retention within the micropores found in this

study may be considered as an additional mechanism for the sustained release from tsc-extrudates in the special case of incubation temperatures below H12 melting.

At this point it should be mentioned that the "random walk" mechanism described by Langer *et al.* may have also been present in the large pores of our sample, however, it can not be detected with our wide-field microscopy technique because the field of view is limited to smaller dimensions.

4. Conclusion

Various authors investigated protein release from inert matrices and found the rates to be controlled by a plethora of factors like wettability of the implant,[30] water entry velocity,[30] particle sizes of the compounds,[4, 15, 21] drug solubility,[25, 26] and drug loading.[4, 16, 20] In order to achieve more sustained release profiles the use of smaller drug particles and a more homogeneous drug distribution within the implant matrix have been successfully applied by various authors.[4, 15, 20, 30, 31] Tsc-extrudates show a sustained protein release profile *per se* which is mainly explained by the dense implant matrix which prevents rapid water access to the implant core and a very fine and homogeneous distribution of the protein particles in the implant matrix. Additionally, partial implant melting during production and release has been identified to strongly influence release kinetics. Besides all mentioned factors, the protein diffusion coefficient within the implant system is the most important factor controlling the release rate[30] and therefore an 'apparent' protein diffusion coefficient is often calculated[22, 25] to allow mathematical modeling of drug release kinetics. This apparent diffusion coefficient takes into account drug solubility, the tortuosity of implant matrix, the constricted pore-geometry between neighboring pores and of course the absolute diffusion coefficient which again can be influenced by temperature and viscosity.[20]

In this work tracking of single IFNα molecules within the lipidic matrix by single-molecule wide-field fluorescence microscopy allowed for the first time to directly observe protein molecule diffusion and to directly measure the absolute diffusion coefficient of IFNα in different phases of the implants. This allowed a more accurate description of the processes involved in protein release from triglyceride based matrices. Two populations of diffusing

protein molecules were detected within the implants. The first population was found to diffuse within PEG and buffer filled pores which were created upon incubation (type 3 areas). This finding is in good agreement with previous theoretical considerations which explain protein release from lipid implants through an interconnected pore-network which is created upon dissolution of hydrophilic excipients and the drug itself.

Surprisingly, a second population was found to diffuse in a phase of molten lipid (type 2 areas). We explained this by the partial melting of the implant matrix during release and concluded that implant melting during preparation led to a fine distribution of IFNα in the implant matrix. In this way the implant matrix was not completely inert but acted as protein reservoir, which was slowly depleted upon incubation at 37°C. Thus, this non-aqueous diffusion pathway is the reason for the more sustained protein release and the very slow release kinetics from tsc-extrudates at incubation temperatures above the melting point of the low-melting lipid.

Although the "random walk" between neighboring large pores formed by PEG dissolution according to Siegel and Langer[19] could not be visualized directly, a similar diffusional behavior for incubation temperatures below H12 melting was detected within micropores on an about two orders of magnitude smaller scale. The retention within these micropores may be an additional mechanism contributing to the sustained release from tsc-extrudates.

The authors conclude that IFNα release from triglyceride based tsc-extrudates is driven by diffusion of protein in PEG-buffer solutions within implant pores and by diffusion of IFNα within molten triglyceride matrix material. The slow diffusion within the molten lipid leads to an enhanced retention of protein release compared to release from inert implants which do not melt.

Supporting information

Movie 1-S: Fast species of fluo-IFNα particles diffusing in a large pore of a type 3 area at 37° and pH 4.0.

Movie 2-S: Slow species of fluo-IFNα particles diffusing in a type 2 area at 37° and pH 4.0.

Movie 3-S: Diffusion of fluo-IFNα particles in a 53% (w/v) PEG solution in PBS at 37° and pH 4.0.

Movie 4-S: Diffusion of fluo-IFNα particles in pure H12 triglyceride at 37°.

References

1. E. H. Moeller, L. Jorgensen, Alternative routes of administration for systemic delivery of protein pharmaceuticals. *Drug Discovery Today: Technologies* **5**, e89 (2008).
2. M. van de Weert, L. Jorgensen, E. Horn Moeller, S. Frokjaer, Factors of importance for a successful delivery system for proteins. *Expert Opinion on Drug Delivery* **2**, 1029 (2005).
3. R. Langer, J. Folkman, Polymers for the sustained release of proteins and other macromolecules. *Nature* **263**, 797 (1976).
4. R. A. Siegel, J. Kost, R. Langer, Mechanistic studies of macromolecular drug release from macroporous polymers. I. Experiments and preliminary theory concerning completeness of drug release. *Journal of Controlled Release* **8**, 223 (1989).
5. R. Bodmeier, H. Chen, Evaluation of biodegradable poly(lactide) pellets prepared by direct compression. *Journal of Pharmaceutical Sciences* **78**, 819 (1989).
6. D. Bodmer, T. Kissel, E. Traechslin, Factors influencing the release of peptides and proteins from biodegradable parenteral depot systems. *Journal of Controlled Release* **21**, 129 (1992).
7. F. Kreye, F. Siepmann, J. Siepmann, Lipid implants as drug delivery systems. *Expert Opinion on Drug Delivery* **5**, 291 (2008).
8. P. Y. Wang, Lipids as excipient in sustained release insulin implants. *International Journal of Pharmaceutics* **54**, 223 (1989).
9. S. Koennings *et al.*, In vitro investigation of lipid implants as a controlled release system for interleukin-18. *International Journal of Pharmaceutics* **314**, 145 (2006).
10. S. Koennings, A. Goepferich, Lipospheres as delivery systems for peptides and proteins. *Lipospheres in Drug Targets and Delivery*, 67 (2005).
11. S. Koennings, Lipid implants for controlled release of proteins. PhD Thesis, Hoffmann-La Roche (2006).
12. C. Guse *et al.*, Biocompatibility and erosion behavior of implants made of triglycerides and blends with cholesterol and phospholipids. *International Journal of Pharmaceutics* **314**, 153 (2006).
13. M. Schwab *et al.*, Correlation of in vivo and in vitro release data for rh-INF[alpha] lipid implants. *European Journal of Pharmaceutics and Biopharmaceutics* **70**, 690 (2008).

14. M. Schwab, G. Sax, S. Schulze, G. Winter, Studies on the lipase induced degradation of lipid based drug delivery systems. *Journal of Controlled Release* **140**, 27 (2009).
15. S. Koennings, A. Sapin, T. Blunk, P. Menei, A. Goepferich, Towards controlled release of BDNF -- Manufacturing strategies for protein-loaded lipid implants and biocompatibility evaluation in the brain. *Journal of Controlled Release* **119**, 163 (2007).
16. S. Mohl, G. Winter, Continuous release of rh-interferon [alpha]-2a from triglyceride matrices. *Journal of Controlled Release* **97**, 67 (2004).
17. H. Reithmeier, J. Herrmann, A. Gopferich, Lipid microparticles as a parenteral controlled release device for peptides. *Journal of Controlled Release* **73**, 339 (2001).
18. S. Schulze, G. Winter, Lipid extrudates as novel sustained release systems for pharmaceutical proteins. *Journal of Controlled Release* **134**, 177 (2009).
19. R. A. Siegel, R. Langer, Controlled Release of Polypeptides and Other Macromolecules. *Pharmaceutical Research* **1**, 2 (1984).
20. R. A. Siegel, R. Langer, Mechanistic studies of macromolecular drug release from macroporous polymers. II. Models for the slow kinetics of drug release. *Journal of Controlled Release* **14**, 153 (1990).
21. S. Kaewvichit, I. G. Tucker, The release of macromolecules from fatty acid matrixes: complete factorial study of factors affecting release. *J. Pharm. Pharmacol.* **46**, 708 (1994).
22. F. Siepmann, S. Herrmann, G. Winter, J. Siepmann, A novel mathematical model quantifying drug release from lipid implants. *Journal of Controlled Release* **128**, 233 (2008).
23. J. Kirstein *et al.*, Exploration of nanostructured channel systems with single-molecule probes. *Nature Materials* **6**, 303 (2007).
24. A. Zürner, J. Kirstein, M. Doblinger, C. Bräuchle, T. Bein, Visualizing single-molecule diffusion in mesoporous materials. *Nature* **450**, 705 (2007).
25. S. Herrmann, S. Mohl, F. Siepmann, J. Siepmann, G. Winter, New Insight into the Role of Polyethylene Glycol Acting as Protein Release Modifier in Lipidic Implants. *Pharmaceutical Research* **24**, 1527 (2007).
26. S. Herrmann, G. Winter, S. Mohl, F. Siepmann, J. Siepmann, Mechanisms controlling protein release from lipidic implants: Effects of PEG addition. *Journal of Controlled Release* **118**, 161 (2007).
27. W. I. Higuchi, Diffusional models useful in biopharmaceutics. Drug release rate processes. *Journal of Pharmaceutical Sciences* **56**, 315 (1967).
28. J. S. Anderson, K. Saddington, S 80. The use of radioactive isotopes in the study of the diffusion of ions in solution. *Journal of the Chemical Society (Resumed)*, S381 (1949).
29. G. Sax, G. Winter, Mechanistic studies on the release of lysozyme from twin-screw extruded lipid implants. *in preparation*.
30. S. Koennings, A. Berie, J. Tessmar, T. Blunk, A. Goepferich, Influence of wettability and surface activity on release behavior of hydrophilic substances from lipid matrices. *Journal of Controlled Release* **119**, 173 (2007).
31. C. Guse *et al.*, Drug release from lipid-based implants: Elucidation of the underlying mass transport mechanisms. *International Journal of Pharmaceutics* **314**, 137 (2006).

7 Summary

In the recent two decades single molecule techniques have emerged as a widely used method in various fields of science due to their ability to provide substantial novel insights into the true behavior of single molecules within their environment. This is brought about by circumventing the ensemble averaging of conventional methods and thus obtaining the distribution of investigated variables. Throughout this work single molecule experiments and single particle tracking have been demonstrated to be well suited to study diffusion in nanoporous systems. For these materials developments towards possible applications are highly awaited in fields ranging from material science to nanomedicine. However, a thorough knowledge of the diffusion of guest molecules in such porous host matrices is vital as a basis for further progress.

In the investigation presented in chapter 3 of this work, a fundamental concept central to the dynamics of diffusion, the ergodic theorem, has been validated experimentally for the first time. Ergodicity means that for systems under equilibrium the time average taken over a single particle is the same as the ensemble average over many particles. The experimental proof of the ergodic theorem was achieved by measuring the diffusivities of guest molecules inside a nano-structured porous glass using single molecule tracking experiments to determine the time-averaged diffusion coefficient. This value is within the limits of accuracy in good agreement with the ensemble value provided under identical conditions by pulsed field gradient NMR. For this validation a situation was considered where the rules of normal diffusion are obeyed. However, it has also been shown by other studies that e.g. in biological systems ergodicity breaking might occur. In these cases the mean square displacement is not increasing linearly with the observation time and is thus found to deviate from normal diffusion. Using the combined potentials of single particle and ensemble techniques, the possible conditions and underlying reasons for ergodicity breaking might be revealed in future studies.

Nanoporous structures constitute very versatile host systems for the incorporation of various guest molecules. Mesoporous silica materials are in this regard of exceptional interest in material science due to their wide range of tunable pore sizes, topologies and

functionalizations as well as their straightforward assembly and low expenses for possible technological applications. Two different mesoporous silica systems were investigated in this work.

The first of them presented in chapter 4.1 deals with the synthesis of highly structured, collinear mesoporous silica filaments. These filaments contain pores that are several microns long. Moreover, the diffusion dynamics of terrylene diimide (TDI) dye molecules and dye-labeled double-strand DNA were studied in such mesoporous filaments using single molecule fluorescence microscopy. The deposition of a thin layer of gold on the samples quenches the fluorescence of the dye molecules residing on the external surface of the filaments, while molecules incorporated in the mesoporous channels remain fluorescent, thus clearly demonstrating successful loading of the guest molecules. TDI was used as a stable and hydrophobic probe molecule for single molecule structural analysis. Additionally, ds-DNA could be incorporated into such a host system without damaging its integrity as shown by FRET measurements. The intact DNA exhibits remarkably long linear trajectories in the mesoporous channels. The diffusion of both types of guest molecules could be controlled by a reversible on-off mechanism induced by exposure of the sample to water and chloroform vapors for TDI or only water vapor for DNA. Insights into the translational as well as the orientational dynamics of the guest molecules could be obtained by analyzing the single molecule data. Furthermore, the direct visualization of the diffusional behavior of both guest molecules in real space allowed to access structural information, such as domain sizes, accessible pore space, the presence of defects, interconnections and dead ends in the mesoporous host material from the viewpoint of the single molecules. Highly structured collinear host systems, such as the mesoporous silica filaments presented in this work, might serve as a platform for the further development of customized nanosystems for applications e.g. in bioanalytics.

In the second study of diffusion of single guest molecules within a mesoporous host system in chapter 4.2, the dynamics and various host-guest interactions of three different terrylene diimide (TDI) dyes within hexagonal and lamellar mesoporous silica thin films were investigated. The three structurally different TDI derivatives allowed studying the influence of the molecular structure of the guest on the translational diffusion behaviour in the hexagonal phase and the lamellar phase. The diffusional behaviour in the hexagonal phase differs dramatically from unrestricted diffusion, e.g. in a liquid medium, as the motion of the

single molecules is confined in the host channels. The highly structured trajectories reveal details about the underlying host structure, such as domain sizes, connectivity between the different channels, the presence of defects sites, e.g. holes in the silica wall or dead ends where the pores are closed. In the lamellar phase, the differences between the three guests are quite dramatic. First, two populations of diffusing molecules - one with parallel orientation of the molecules to the lamellae and the other with perpendicular orientation - could be observed for two of the TDI derivatives. These populations differ drastically in their translational diffusion behaviour. Depending on the TDI derivative, also the ratio between the two populations is different. Additionally, switching between the two populations was observed. These data provide novel insights into host-guest interactions, such as the influence of the molecular structure of the guest molecules on their diffusional as well as on their orientational behaviour in structurally confined guest systems. This might be a first step towards designing guests with adapted diffusion properties and thus gaining better control over host-guest interactions.

In the approach presented in chapter 5.1 mesoporous thin films were used as spatial separator and their structured channels served as guiding pathways for single dye molecules and quantum dots diffusing along silver island films (SIF). Due to the island structure of these thin silver films the diffusing fluorophores in the mesoporous film on top of the SIF encounter varying distances in the range of several nanometers up to 20 nm to the metal nanoparticles. Depending on this distance the absorption and emission properties of the single fluorophores may be altered. Thereby, the fluorescence of these fluorophores can be quenched or enhanced by coupling to the plasmon of the metal nanoparticle. Using single molecule fluorescence microscopy and SPT, diffusion of the used organic dye molcules and quantum dots was demonstrated in these ultra-thin mesoporous films. In samples on top of a SIF the diffusing fluorophores exhibited significant variations in their emitted fluorescence intensities depending on the position along their trajectories.

While the influence of metal nanoparticles on the absorption and emission of single fluorophores is a very interesting field of research yet to be fully explored, also the luminescence after photo-activation of metal nanostructures itself is a worthwhile subject to investigate. In the study discussed in chapter 5.2, the photophysical properties of silver nano-wires with regard to their real structure were investigated using a combination of

wide-field fluorescence- and transmission electron microscopy. In consecutive fluorescence images synchronous emission from different distinct positions along the silver nano-wires was observed over time. The sites of emission were separated spatially by up to several micrometers. Various transmission electron microscopy based techniques were used to investigate nano-wires exhibiting such a cooperative effect. From the results provided by determining the chemical composition in emissive regions, it was concluded that the emissive sites are tiny silver clusters, which were generated photochemically. The cooperative emission behavior might thus be created by coupling of the emitters via surface plasmons of the silver nano-wire.

Nanoporous materials are also well suited for drug delivery purposes in nanomedicine. Thereby, a specific dose of a therapeutic agent can be delivered in a controlled way over an extended amount of time. In particular, the sustained release of protein drugs from lipid drug reservoirs is a very promising approach for long term delivery due to the excellent stability, biocompatibility and biodegradability of the lipid devices. Using single molecule microscopy and tracking of individual fluorescently labeled recombinant human IFNα protein molecules within lipid tsc-extrudates as described in chapter 6, the diffusion coefficients of these molecules could be determined directly for the first time. This allowed the elucidation of the major mechanisms which contribute to the sustained release from such tsc-extrudates. The formation of large pores by PEG dissolution within the lipidic host matrix (consisting of the high-melting lipid D118 and the low melting lipid H12) upon incubation in a buffer solution constitutes the first mechanism. Additionally, it was found that the lipidic implant matrix is in fact not as "inert" as it has been presumed in previous studies. In particular, the low melting lipid H12 partially melts during the production process at elevated temperatures and some amount of the protein molecules gets embedded into this H12 melt. Therefore, these molecules are trapped at incubation temperatures below H12 melting and only get released from molten H12. The second mechanism contributing to the more sustained release from tsc-extrudates is the release from this lipid phase, because the diffusion coefficient of protein molecules in the triglyceride melt is much smaller than within the large pores formed by PEG. At incubation temperatures below the melting point of H12, protein molecules diffusing within small micropores with sizes of up to a few micrometers were detected within the implants. These protein molecules were trapped within cavities

until they randomly found an accessible connection to the next one. The retention within these micropores can be considered as a third mechanism for the sustained release from tsc-extrudates at temperatures below H12 melting.

The individual studies presented in this thesis provide detailed insights into the diffusional behavior of single molecules in nanoporous systems. These results strengthen the knowledge of essential processes occurring in these nano-scaled materials towards possible future applications in nanotechnology. Single molecule studies, which are an exceptionally useful tool for the investigation of diffusion in nanoporous matter, allow to establish deeper understanding of such systems compared to ensemble methods, which might not be conclusive due to averaging.

8 List of abbreviations

AAM	anodic alumina membrane
AFM	atomic force microscopy
Ag-NW	silver nano-wire
APD	avalanche photodiode
BET	Brunauer-Emmett-Teller
CCD	charge coupled device
CTAB	cetyltrimethylammonium bromide
DNA	deoxyribonucleic acid
DSC	differential scanning calorimetry
EDX	energy dispersive X-ray spectroscopy
e.g.	exempli gratia
EISA	evaporation-induced self-assembly
EM-CCD	electron multiplying charge coupled device
et al.	et alii
FFT	fast Fourier transformation
FRET	Förster resonance energy transfer
fps	frames per second
HRTEM	high resolution transmission electron microscopy
HP-β-CD	hydroxypropyl-β-cyclodextrin
IC	internal conversion
i.e.	id est
IFNα	recombinant human interferon α2a
IR	infrared
ISC	intersystem crossing
IUPAC	International Union of Pure and Applied Chemistry
laser	light amplification by stimulated emission of radiation
MSD	mean square displacement
NA	numerical aperture
NMR	nuclear magnetic resonance
OD	optical density

PBS	phosphate buffered saline
PEG	polyethylene glycol
PFG NMR	pulsed field gradient nuclear magnetic resonance
QD	quantum dot
rcf	relative centrifugal force
rpm	rounds per minute
SAXS	small-angle X-ray scattering
SEM	scanning electron microscopy
SIF	silver-island film
SMS	single molecule spectroscopy
SNR	signal-to-noise ratio
SPT	single particle tracking
STEM	scanning transmission electron microscopy
TDI	terrylene diimide
TEM	transmission electron microscopy
TEOS	tetraethyl orthosilicate
tsc-extrusion	twin screw extrusion
UV-Vis	ultraviolet-visible
XRD	X-ray diffraction

9 List of publications and contributions to conferences

9.1 Publications

First-author publications in peer reviewed journals

1. F. Feil, C. Jung, J. Kirstein, J. Michaelis, C. Li, F. Nolde, K. Müllen, C. Bräuchle, Diffusional and orientational dynamics of various single terrylene diimide conjugates in mesoporous materials. *Microporous and Mesoporous Materials* (Special Issue: Diffusion in micropores) **125**, 70 (2009).

2. F. Feil*, S. Naumov*, J. Michaelis, R. Valiullin, D. Enke, J. Kärger, C. Bräuchle, Single-Particle and Ensemble Diffusivities - Test of Ergodicity. *Angewandte Chemie* **124**, 1178 (2012) / *Angewandte Chemie International Edition* **51**, 1152 (2012).

3. F. Feil*, V. Cauda*, T. Bein, C. Bräuchle, Direct Visualization of Dye and Oligonucleotide Diffusion in Silica Filaments with Collinear Mesopores. *Nano Letters* **12**, 1354 (2012).

4. G. Sax*, F. Feil*, S. Schulze, C. Jung, C. Bräuchle, G. Winter, Release pathways of interferon α2a molecules from lipid twin screw extrudates revealed by single molecule fluorescence microscopy. *Journal of Controlled Release*, submitted.

5. M. Davies*, A. Wochnik*, F. Feil*, C. Jung, C. Bräuchle, C. Scheu, J. Michaelis, Synchronous emission from nanometric silver particles through plasmonic coupling on silver nano-wires. *ACS Nano*, submitted.

[*] These authors contributed equally to this work.

Co-author publications in peer reviewed journals

1. S. Wirth, A. U. Wallek, A. Zernickel, F. Feil, M. Sztiller-Sikorska, K. Lesiak-Mieczkowska, C. Bräuchle, I.-P.Lorenz, M. Czyz, Tautomerization of 2-nitroso-N-arylanilines by coordination as N,N'-chelate ligands to rhenium(I) complexes and the anticancer activity of newly synthesized oximine rhenium(I) complexes against human melanoma and leukemia cells in vitro. *Journal of Inorganic Biochemistry* **104** 774 (2010).

9.2 Contributions to conferences

Talks

1. *Diffusional and orientational dynamics of various single terrylene diimide conjugates in mesoporous materials*
   73rd Annual conference of the German Physical Society 2009, Technische Universität Dresden, Dresden, Germany.

2. *Single molecule diffusion*
   Internal workshop of the International Doctorate Program NanoBioTechnology 2009, Ludwig-Maximilians-Universität München, München, Germany.

3. *Diffusion in nanoporous systems*
   Summer school of the International Doctorate Program NanoBioTechnology 2010, Aiterbach am Chiemsee, Germany.

4. *Single molecule diffusion in columnar functionalized mesoporous rods*
   75rd Annual conference of the German Physical Society 2011, Technische Universität Dresden, Dresden, Germany.

Poster presentations

1. *Single molecule studies of mesoporous materials*
   21st German Zeolite Conference 2009, Christian-Albrechts-Universität zu Kiel, Kiel, Germany.

2. *Single Molecule Studies of Mesoporous Materials: From Material Science to Drug-Delivery Applications*
   SFB 486 Meeting 2009, Venice International University, Venice, Italy.

3. *Optical investigations of plasmons generated in silver nanowires and their influence on the emission of dye molecules*
   74rd Annual conference of the German Physical Society 2010, Universität Regensburg, Regensburg, Germany.

4. *Single molecule diffusion studies of mesoporous materials: From material science to drug-delivery applications*
   Diffusion Fundamentals IV 2011, Rensselaer Polytechnic Institute, Troy, NY, USA.

Participation

1. *Complex Nanosystems - Assembly, Control and Functionality*
   Workshop of the Center for NanoScience (CeNS) 2008, Venice International University, Venice, Italy.

2. 22st German Zeolite Conference 2010, Ludwig-Maximilians-Universität München, München, Germany.

3. Winter school of the Nanosystems Initiative Munich (NIM) 2011, St. Christoph, Austria.

10 Acknowledgements

First of all, I wish to express my sincere gratitude to Prof. Dr. Christoph Bräuchle for the opportunity to do research on such a fascinating field of science as well as for his support and advice during all the time.

In addition, I am especially grateful to my co-supervisor Prof. Dr. Jens Michaelis for his expert knowledge and all the fruitful discussions.

Furthermore, I would like to thank the board of examiners for reviewing this thesis and their participation in my defense examination.

Many thanks go to all collaborators and their group leaders: Valentina Cauda and Prof. Dr.Thomas Bein, Gerhard Sax and Prof. Dr. Gerhard Winter, Sergej Naumov and Prof. Dr. Jörg Kärger, Angela Wochnik and Prof. Dr. Christina Scheu.

I also would like to thank my former students Meli, Chrissy, Matthias and Christine for their contributions to this work in course of their internships.

Special thanks go to my colleagues Meli, Stefan, Leonhardt, Vroni, Ellen, Frauke and Adriano from the AK Bräuchle group as well as to all other past and present members of the AK Bräuchle / Lamb / Michaelis.

Special words of gratitude go to my parents, Ludwig and Ingrid, my brother Norbert and my sister Sylvia for their belief and continuous support.

Finally, I want to thank Julia. Thank you for your belief, motivation and love!